UNIVERSITY OF CALIFORNIA,
IRVINE

Environmental Controls on Marine Particulate C:N:P Ratios

DISSERTATION

submitted in partial satisfaction of the requirements
for the degree of

DOCTOR OF PHILOSOPHY

in Earth System Science

by

Catherine Amanda Garcia

Dissertation Committee:
Professor Adam C. Martiny, Chair
Professor J. Keith Moore
Assistant Professor Katherine R.M. Mackey

2020

DEDICATION

To my family - Nancy, Mike and Joe Roney

Thank you for your love and support.

And to my partner, Gerson Garcia

No matter how far out to sea I go, you are the final port.

Sea fever*, by John Masefield*

"I must go down to the seas again, to the lonely sea and the sky,

And all I ask is a tall ship and a star to steer her by;

And the wheel's kick and the wind's song and the white sail's shaking,

And a grey mist on the sea's face, and a grey dawn breaking.

I must go down to the seas again, for the call of the running tide

Is a wild call and a clear call that may not be denied;

And all I ask is a windy day with the white clouds flying,

And the flung spray and the blown spume, and the sea-gulls crying.

I must go down to the seas again, to the vagrant gypsy life,

To the gull's way and the whale's way where the wind's like a whetted knife;

And all I ask is a merry yarn from a laughing fellow-rover,

And quiet sleep and a sweet dream when the long trick's over."

TABLE OF CONTENTS

LIST OF FIGURES

LIST OF TABLES

ACKNOWLEDGMENTS

I am so happy to thank of all my family and mentors for their support. To my parents: thank you for encouraging me to be independent and for supporting me in all my decisions in life with more love than I could ever have asked for. Thank you to my advisor, Adam Martiny, who has pushed me to expand my knowledge base and allowed me the space to find my path. You have talk me how to ask the right questions and not be weighed down by the tough parts of science. Thank you to my committee member Keith Moore, who has supported five years of great ocean biogeochemistry discussions. To my other committee member Kate Mackey, thank you for your thoughtful comments and for being a wonderful example.

To all of the members of the Martiny lab, past and present, thank you for making this a family experience. You have all strived to do your best work for the lab, as much as for yourselves. Alyssa, Alli, and Alyse, thank you for being amazing colleagues and women of science. We have grown through each other through understanding and tears. To Jenna and Angie, you have been incredible undergrads to mentor, are full of curiosity, and have bright futures ahead – whether in science or needle-felting or baking or art. To Stacy, Lucas, and Melissa, thank you for jumping into our crazy family and making the past few years incredible. To Celine and Claudia, thank you for being the support structures you were in the respective Martiny labs and for training new generations of scientists. To Nathan and Mo – thank you your support as far back as USC and through all the past five years navigating grad school. To Teghveer – you have a large heart and brought so much laughter to the lab. Thank you all for the holiday parties and lunches, and please learn how to bowl!

Thank you to my wonderful husband Gerson Garcia. You were with me when this journey started back in Los Angeles. You have always wanted to be a supporting figure to reach this goal. I hope I can do the same on your own journey through life to fulfill your aspirations.

Financial support was provided by the NASA Earth and Space Science Fellowship. Thank you to the Johnson lab for generously allowing us to use their elemental analyzer.

Chapter 1 was published with the permission of Springer Nature. The text of this chapter is a reprint of the material as it appears in the journal Nature Communications. Chapter 3 was published with the permission of Philosophical Transactions for Royal Society B. The text of this chapter is a reprint of the material as it appears in the journal Philosophical Transactions for Royal Society B.

VITA

EDUCATION

PhD 2020	University of California – Irvine, Earth System Science, Advisor: Dr. Adam Martiny
B.S. 2011	Northeastern University, Biological Sciences Concentrations: Marine Science, Three Seas Program, Nahant, MA Concentration in Maritime Studies, Sea Education Association, Woods Hole, MA

AWARDS AND ACHIEVEMENTS

2015-2019	NASA Earth & Space Fellowship *Global Distribution Patterns of Phytoplankton Communities and Their Elemental Stoichiometry Using MODIS Satellite Data*
2017	*OCB supported* early career participation in *Cornell Satellite Remote Sensing class*.
2017	Earth System Science Travel Grant, UC Irvine
2016	Associated Graduate Student Union Travel Grant, UC Irvine

PUBLICATIONS – PEER-REVIEWED

Garcia, CA, Hagstrom, GI, Larken, AA, Ustick, LJ, Levin, SA, Lomas, MW, and Marticy, AC. (2020) Linking regional shifts in microbial genome adaptation with surface ocean biogeochemistry. *Phil. Trans. R. Soc. B,* Article number: 20190254.

Martiny AC, Ustick L, Garcia CA, and Lomas MW. (2019) Genomic adaptation of marine phytoplankton populations regulates phosphate uptake. *Limnology and Oceanography.*

Larkin AA, Garcia CA, Ingoglia KA, Garcia NS, Baer SE, Twining BS, Lomas MW, and Martiny AC. (2019) Subtle biogeochemical regimes in the Indian Ocean revealed by spatial and diel frequency of *Prochlorococcus* haplotypes. *Limnology and Oceanography.*

Garcia CA, Baer SE, Garcia NS, Rauschenberg S, Twining BS, Lomas MW, and Martiny AC. (2018) Nutrient supply controls particulate elemental concentrations and ratios in the low latitude eastern Indian Ocean*. Nature Comm.* 9, Article number: 4868. 2018.

Baer SE, Rauschenberg S, Garcia CA, Garcia NS, Martiny AC, Twining AC, and Lomas MW. (2018) Carbon and nitrogen productivity during spring in the oligotrophic Indian Ocean along the GO-SHIP IO9N transect. *Deep-Sea Res. II.*

Kent AG, Garcia CA, and Martiny AC. (2018) Increased biofilm formation due to high temperature adaptation in marine *Roseobacter. Nature Microbiol.*

PRESENTATIONS

* *Presented by CA Garcia*

2020* Garcia CA, Hagstrom, GI, Larken, AA, Ustick, LJ, Levin, SA, Lomas, MW, and Marticy, AC. (2020) Incorporating phytoplankton genomic traits into cellular resource allocation models. Ocean Sciences Meeting, San Diego, CA.

2019* Garcia CA and Martiny AC. (2019) Remote sensing of global ocean surface phosphate. Ocean Carbon Biogeochemistry Summer Workshop. Poster Session, Woods Hole, MA. [Poster]

2018* Garcia CA and Martiny AC. (2018) Global prediction of surface phosphate using remote sensing. Environmental Research Poster Session, Irvine, CA. [Poster]

2018 Moreno AR, Garcia CA, Lee JA, Larkin, AA, Primeau FW, Moore JK, and Martiny AC. (2018) Pacific Ocean biome variation in the respiration quotient of particulate organic matter. Environmental Research Poster Session, Irvine, CA. [Poster]

2018* Kent AG, Garcia CA, and Martiny AC. (2018) Increased biofilm formation due to high temperature adaptation in marine *Roseobacter*. Marine Microbes Gordon Research Conference, Lucca, Italy. [Poster]

2018 Larkin AG, Garcia CA, Ingoglia KA, Garcia NS, Baer SE, Twining BS, Lomas MW, and Martiny AC. (2018) Differential distribution and estimated growth patterns of microdiverse *Prochlorococcus* haplotypes in the Indian Ocean. Marine Microbes Gordon Research Conference, Lucca, Italy. [Poster]

2018* Garcia CA, Baer SE, Garcia NS, Rauschenberg S, Twining BS, Lomas MW, and Martiny AC. (2018) Nutrient supply controls particulate elemental concentrations and ratios in eastern Indian Ocean, US-India Colloquium. Goa, India. [Oral].

2018* Garcia CA, Baer SE, Garcia NS, Rauschenberg S, Twining BS, Lomas MW, and Martiny AC. (2018) Nutrient supply controls particulate elemental concentrations and ratios in eastern Indian Ocean. NASA Biodiversity and Ecological Forecasting Meeting, Washington, DC. [Poster].

2017* Garcia CA, Baer SE, Garcia NS, Rauschenberg S, Twining BS, Lomas MW, and Martiny AC. (2018) Nutrient supply controls particulate elemental concentrations and ratios in eastern Indian Ocean. Poster presented at: 2nd International Indian Ocean Expedition Symposium (IIOE-2); San Diego, CA.

2017 Larkin AA, Ingoglia KA, Garcia CA, Lomas MW, and AC Martiny. The distribution of Prochlorococcus ecotypes reveals patterns of nutrient-limitation in the Indian Ocean. Poster presented at: 2nd International Indian Ocean Expedition Symposium (IIOE-2); San Diego, CA.

2017* Garcia CA, Baer SE, Garcia NS, Rauschenberg S, Twining BS, Lomas MW, and Martiny AC. (2018) Regional differences and diel rhythm of particulate

elemental concentrations and ratios in the eastern Indian Ocean. Ocean Sciences Meeting, Honolulu, HI. [Oral].

RESEARCH & TEACHING APPOINTMENTS

2012-2014	Lab Manger – Fuhrman Lab, University of Southern California *Topic:* Marine microbial diversity at the San Pedro Ocean Time-Series
2011	Marine Educator/Deckhand, Schooner Inc., New Haven, CT
2010	Undergraduate Researcher – Cheney Lab, Northeastern University *Topic:* Analyzed accumulation of PCB pollutants within food chain in New Bedford harbor
2010	Research Assistant, Adnexus, a Bristol-Myers Squibb R&D Company *Topic:* Screen targets using enzyme-linked immunosorbent assays (ELISAs) and homogeneous assays.
2009	Research Assistant – Anderson Lab, Woods Hole Oceanographic Institution *Topic:* Microbial diversity of toxin-producing Dinoflagellates in the North Atlantic and cultured freshwater isolates
2007-2009	Assistant Outreach Coordinator, Northeastern Marine Science Center, Nahant, MA
2008	Oceanography Research Project in Atlantic Ocean, Sea Education Association *Topic:* Zooplankton Geography and Diel Vertical Migration in Coastal Waters, the North and South Sargasso Sea, and the Tropics
2007	Undergraduate Research Assistant – Vollmer Lab, Northeastern University *Topic:* Analyzed genetic resistance to white band disease in coral *Acropora* sp.

FIELD EXPERIENCE

2018	R/V Ronald H. Brown, CLIVAR I07N - *Particulate organic carbon, nitrogen and phosphorus and ratio trends in western Indian Ocean.* Durban/Goa. 39 days.
2016 – 2017	R/V Ronald H. Brown, CLIVAR P18 leg 2 - *Particulate organic carbon, nitrogen and phosphorus and ratio trends in South Pacific.* Easter Island/Punta Arenas. 37 days.
2016	R/V Roger Revelle, CLIVAR I09N – *Particulate organic carbon, nitrogen and phosphorus and ratio trends in eastern Indian Ocean.* Perth/Phuket. 38 days.
2012 – 2014	R/V Yellowfin, SPOT Time Series – *Monthly sampling of the San Pedro Basin for bacterioplankton and viral cell counts and DNA samples, NH_4 & NO_2, and heterotrophic production rates.* San Pedro, CA
2010	New Bedford Harbor - *Seine net collections of grass shrimp, mummichog fish, and macroalga Ulva sp. for PCB pollutant study*. New Bedford, MA

2009 Nauset Marsh - *red tide study, involved collections of marine toxin-producing dinoflagellates Alexandrium* sp. Nauset, MA.

2008 SSV Corwith Cramer, C-219 - *Zooplankton Geography and Diel Vertical Migration in Coastal Waters, the North and South Sargasso Sea, and the Tropics.* Woods Hole/St. Croix. 35 days.

SERVICE/OUTREACH

2019 Student mentor, Senior Career Program Irvine High School, Irvine, CA
2018 Women's Shelter Outreach, Goa, India
2016 Aquarium of the Pacific Meet a Scientist! Long Beach, CA
2013, 2014 World Ocean Sampling Day, University of Southern California, Los Angeles, CA
2007 - 2010 Marine Science Center Outreach, Northeastern University Nahant, MA

TRAINING AND WORKSHOPS

2018 Bayesian Statistics using Stan, UC-Irvine, CA
2017 Ocean Carbon Biogeochemistry Indian Ocean Workshop, La Jolla, CA
2017 Cornell Satellite Remote Sensing, Ithaca, NY
2016 Data Science Initiative workshops (Spatial-Temporal Models, Introduction to R, Predictive Modeling with Python), UC-Irvine, CA

PROFESSIONAL ORGANIZATIONS

2016 AWIS, American Women in Science, Los Angeles/Ventura County Chapter
2016 ASLO, Association for the Sciences of Limnology and Oceanography

ABSTRACT OF THE DISSERTATION

Environmental Controls on Marine Particulate C:N:P Ratios

By

Catherine Amanda Garcia

Doctor of Philosophy in Earth System Science

University of California, Irvine, 2019

Professor Adam C. Martiny, Chair

Elemental ratios of particulate organic matter (POM) are key to linking biogeochemical cycles. Microbial uptake and allocation of essential biogenic elements (carbon (C), nitrogen (N), and phosphorus (P)) influence the distribution of nutrients throughout the ocean. This dissertation evaluates the role of environmental stress and underlying phytoplankton diversity in driving regional variation in the ratio of particulate C:N:P. Competing hypotheses predict C:N:P equally well due to regional co-variance in environmental conditions and biodiversity. The Indian Ocean offers a unique positive temperature and nutrient supply relationship to test these hypotheses. We collected 248 POC:N:P observations in the eastern Indian Ocean along this environmental gradient. As phytoplankton community composition was constant, biodiversity changes could not explain the elemental variation. Instead, our data supports the nutrient supply hypothesis over the influence of temperature.

Nutrients concentrations are often below detection limits in subtropical ocean regions. We develop two methods to predict nutrient stress to further evaluate its role in particulate C:P regulation. In the first method, we develop a global remote sensing

estimate of surface phosphate. Using a mechanistic framework, we develop an artificial neural network to provide a robust basis for developing a remote sensing estimation of surface phosphate. However, C:P predictions using only phosphate did not match observations in either the South Indian or Pacific subtropical gyres. To address this challenge, we develop a second method by applying genomic shifts among microbial communities as 'biosensors' for the *in situ* nutritional environment. We find that our genome-based trait-model significantly improves our prediction of particulate C:P across ocean regions. Furthermore, we detect previously unrecognized ocean areas of iron, nitrogen, and phosphorus stress. Ultimately, we find a combination of nutrient stress accounts for global variation in particulate C:P.

INTRODUCTION

The elemental composition of ocean phytoplankton ultimately determines the distribution of major biogenic elements. This core role was first described by Alfred Redfield when he linked the ratio of nutrient concentrations (NO3:PO4) to the average composition of particulate organic carbon (C), nitrogen (N), and phosphorus (P) (Redfield, 1934). Since the Redfield Ratio (106C: 16N: 1P) was first described, it has been widely used to model biological processes (e.g. remineralization rates of exported organic matter, nutrient uptake rates, etc.). However, recently systematic latitudinal and taxonomic variation in the ratio of C:N:P has emerged (Martiny et al., 2013a; Martiny et al., 2013b). While this discovery has improved model predictions of nutrient distributions (Teng et al., 2014), we as yet only hypothesize which factors control global trends in C:N:P (Moreno & Martiny, 2018). Here, the following chapters evaluate the environmental drivers underlying variation in surface ocean particulate C:N:P.

It is challenging to tease apart phytoplankton stoichiometry hypotheses, as temperature, nutrient availability, and community composition covary *in situ*. Cold, nutrient-rich water corresponds to larger phytoplankton taxa and depressed C:N:P ratios, and vice versa yields elevated ratios. The Indian Ocean is a unique basin, where the relationship between temperature and nutrient supply is opposite the global relationship. As such, we can tease apart these hypotheses based on expected predictions. In Chapter 1, we sampled particulate organic matter (POM) along with environmental conditions to address the following questions; How do POM concentrations and elemental ratios vary between regions and on short-term scales within regions? How do the phytoplankton community composition and environmental conditions relate to variation in POM

concentrations and elemental ratios? Is the South Indian Ocean gyre unique in terms of its POM concentrations, ratios, and controls compared to other oligotrophic gyres?

By identifying the regional importance of temperature and nutrient availability, we can better predict how POM composition will respond to changing climate patterns. Fluctuating temperature influences phytoplankton physiology directly, but also indirectly as phytoplankton may adjust to increased stratification between surface and deep ocean layers. The primary environmental controls of phytoplankton processes are light, temperature, and nutrients. Whereas light and temperature are easy to observe, nutrient availability is poorly defined and difficult to measure. Chapters 2 and 3 develop novel methods to predict nutrient availability and limitation in the surface ocean. With these nutrient proxies, we can use an existing phytoplankton trait model (Moreno et al., 2018) to predict C:P ratios under differing environmental conditions.

There is no remote sensing product for global ocean phosphate, whereas sea surface temperature (SST) and photosynthetically active radiation (PAR) are commonly observed via satellite. Based on the results from Chapter 1, a dynamic prediction of nutrients is needed to accurately predict C:P in the low latitudes (Garcia et al., 2018). Previous attempts to model nitrate concentrations are based on temperature and/or chlorophyll due not capture concentrations below detection limits (Switzer et al., 2003). Furthermore, the underlying patterns of ultralow phosphate concentrations differ (Martiny et al, 2019). In Chapter 2, we develop an artificial neural network model of surface phosphate. Firstly, we test which combination satellite inputs leads to the best prediction of surface phosphate along four defined gradients. Secondly, we describe the regional uncertainty for the best

model fits. However, we find that a trait model using a single nutrient input is not enough to predict C:P ratios in the Indian Ocean.

The Indian Ocean has complex nutrient limitation patterns (Twining et al., 2019). As such, models must account for multiple nutrients to accurately predict cellular allocation of C:P. Particulate. This is difficult in oligotrophic biomes, where nitrate and sometimes phosphate concentrations are below detection. In Chapter 3, we use metagenomes collected across three low latitude ocean basins (Indian, Pacific, and Atlantic) to develop a second nutrient stress proxy. We address the following questions; 1) Can we quantify the genetic variation of nutrient assimilation genes and relate this metric to gradients in nutrient stress? 2) Does this underlying variation in nutrient uptake genes lead to a better prediction of C:P?

CHAPTER 1

Nutrient supply controls particulate elemental concentrations and ratios in the Eastern Indian Ocean

Co-authors: Steven Baer, Nathan Garcia, Sara Rauschenberg, Ben Twining, Michael Lomas, and Adam Martiny.

Abstract

Variation in ocean C:N:P of particulate organic matter (POM) has led to competing hypotheses for the underlying drivers. Each hypothesis predicts C:N:P equally well due to regional co-variance in environmental conditions and biodiversity. The Indian Ocean offers a unique positive temperature and nutrient supply relationship to test these hypotheses. Here we show how elemental concentrations and ratios vary over daily and regional scales. POM concentrations were lowest in the southern gyre, elevated across the equator, and peaked in the Bay of Bengal. Elemental ratios were highest in the gyre, but approached Redfield proportions northwards. As *Prochlorococcus* dominated the phytoplankton community, biodiversity changes could not explain the elemental variation. Instead, our data supports the nutrient supply hypothesis. Finally, gyre dissolved iron concentrations suggest extensive iron stress, leading to depressed ratios compared to other gyres. We propose a model whereby differences in iron supply and N_2-fixation influence C:N:P levels across ocean gyres.

Keywords: Indian Ocean, marine biogeochemistry, particulate organic matter, phytoplankton stoichiometry

Introduction

Elemental ratios of particulate organic matter (POM) are key to linking biogeochemical cycles. The carbon:nitrogen:phosphorus (C:N:P) ratio is often assumed globally constant at Redfield proportions (106C:16N:1P). However, recent observations show high ratios in nutrient-poor subtropical gyres and low ratios in nutrient-rich environments (Martiny et al., 2013; Weber & Deutsch, 2010). There are also ocean basin differences with higher C:P and N:P values in the North Atlantic subtropical gyre and lower ratios in other subtropical gyres (Martiny et al., 2013; Teng et al., 2014). However, many regions remain woefully under-sampled, especially in regards to particulate organic phosphorus.

Individual studies have presented competing hypotheses explaining global variation in the elemental ratios of POM (Moreno & Martiny, 2018). First, the translation-compensation hypothesis predicts a negative relationship between temperature and the cellular concentration of P-rich ribosomes as higher temperatures increase ribosomal translation efficiency (Toseland et al., 2013). This would lead to a positive relationship between temperature and C(N):P ratios. Second, the nutrient supply hypothesis predicts that nutrient stressed cells are frugal and have low cell quotas of the limiting nutrient. For example, this hypothesis predicts a negative correlation between C:P and ambient P availability (Galbraith & Martiny, 2015; Klausmeier et al., 2004). Thirdly, the allometric diversity hypothesis predicts that smaller, nutrient uptake specialists like *Prochlorococcus* have elevated C:P and N:P in comparison to larger lineages like diatoms (Arrigo, 2005; Klausmeier et al., 2004; Martiny et al., 2013). However, it is a challenge to separate these

hypotheses as temperature, nutrient supply, and community composition strongly co-vary in the ocean.

The Indian Ocean (IO) accounts for 15-20% of global ocean net primary production (Behrenfeld & Falkowski, 1997), but there are few published data that describe the ocean biogeochemistry of particulate organic matter in this region. In the Indian Ocean spring inter-monsoon season, sea surface temperatures and macronutrient concentrations increase northwards. Strong gradients in temperature and nutrient concentrations in the surface ocean suggest three distinct regions: an oligotrophic, cooler (20.5-29.7^{o}C) Southern Indian Ocean gyre (SIO gyre); a warm (30.3-31.5^{o}C) upwelling region north of 10°S (EqIO); and a warm (29.1-32.6^{o}C), higher biomass region in the Bay of Bengal (BoB) (Grand et al., 2015). Although surface nutrient concentrations are consumed to near depletion throughout the basin, two overturning thermohaline cells deliver nutrient-replete water close to the surface around 10°S and slightly north of the equator (Lee, 2004). However, the northern branch of the cross-equatorial cell is not well defined (Schott et al., 2002). The Bay of Bengal also has elevated nutrient supply driven seasonally by coastal upwelling and river inputs, thereby leading to periods of increased productivity (Gomes et al., 2000). Thus, it appears that the warmest regions are also the most nutrient replete in the eastern Indian Ocean leading to temperature and macronutrient supply being uniquely positively correlated. As such, this region enables a test of our hypotheses for how phytoplankton stoichiometry ratios are controlled.

Here, we ask the following three questions about environmental and biological controls of biogeochemistry in the eastern Indian Ocean: How do particulate organic matter concentrations and elemental ratios vary between regions and on short-term scales

within regions? How do the phytoplankton community composition and environmental conditions relate to variation in POM concentrations and elemental ratios? Is the SIO gyre unique in terms of its POM concentrations, ratios and controls compared to other oligotrophic gyres?

Our results suggest that nutrient supply is the leading driver of regional variation in elemental composition in the eastern Indian Ocean as well as other low latitude regions. However, the C:P ratio in the SIO gyre is low in comparison to other subtropical gyres leading us to propose that iron stress controls the POM C:P ratio in oligotrophic regions via regulation of N_2-fixation. Thus, the unique biogeochemistry of the Indian Ocean provides key information for understanding the controls of ocean C:N:P.

Results

I09N transect environmental gradients

To quantify the link between environmental gradients, phytoplankton community composition, particulate organic matter (POM) concentrations, and ratios, we collected samples across 238 stations in the eastern Indian Ocean (Figure 1.1, S1.1). Both the western and eastern Indian Ocean experienced anomalously warm sea surface temperature (SST) during the sampling period. However, there was an overall positive Indian Ocean Dipole (IOP +0.34, April 2016) since the eastern basin was cooler. These conditions favor wind patterns that promote upwelling off Indonesia (Wiggert et al., 2009). Based on near surface temperature and nutrient concentration gradients, we classified the transect into the Southern Indian Ocean gyre (SIO gyre, 31°S - 12°S), an equatorial upwelling region (EqIO, 10°S - 5°N), and the Bay of Bengal (BoB, 5°N - 19°N)(Figures 1.2A and B, Figure S1.1). Due to uncertainty in the SIO gyre-Indonesian through flow transition,

12°S was used instead of 10°S as the gyre northern cutoff. We used the depth of the 1μM NO_3 isocline to define the nutricline and applied this as a proxy for nutrient supply into the surface layer (Figure 1.2B, Figure S1.2) (Cermeño et al., 2008). SIO gyre had the lowest surface temperature and the deepest nutricline depth along the transect (218 m)(Table S1.1 and Figures 1.2A and B). EqIO was characterized by temperatures above 29°C and the nutricline shoaled to 71 m. Increased nitrate concentrations below the nutricline near 10°S, the equator, and 5°N corresponded to bands of elevated chlorophyll (Figure 1.1)("NASA Goddard Space Flight Center, Ocean Ecology Laboratory, Ocean Biology Processing Group. Moderate-resolution Imaging Spectroradiometer (MODIS) Aqua Chlorophyll a 4km Data; NASA OB.DAAC, Greenbelt, MD, USA.," n.d.). This suggests high nutrient supply at these bands. In BoB, temperature was on average 30.8°C, and the nutricline remained constant (70 m). Overall, there was a coupled negative relationship between SST and nutricline depth (R = -0.88). Thus, there were significant regional environmental differences, but in support of our prediction, a uniquely positive relationship between temperature and the nutrient supply.

Short term and regional variation in POM

We identified significant diel variability of POM concentrations and elemental ratios (Figure 1.3). Particulate organic carbon (POC) had the strongest cycle with a maximum at dusk, and minimum at dawn. POP had a similar cycle, whereas PON cycled with a peak between midnight and 07:00 local time (Table S1.1). The stronger oscillation in POC led to C:N and C:P maxima near dusk. The temporal shift in the peak of PON relative to POP led to a weak N:P ratio maximum at 17:00 local time. Over the course of a day, on average the

ratio of C:P changed by 13.4, N:P by 0.64, and C:N by 0.58 in the eastern Indian Ocean. These daily ranges were comparable to differences observed between regions (Table S1.1).

We next found distinct diel amplitudes across regions (Figure 1.3). The smallest amplitudes for all POM concentrations and elemental ratios were observed in SIO gyre, but no significant differences between the BoB or EqIO regions (Table S1.1). Using the daily POC range as a proxy for daily biomass accumulation, the highest normalized accumulation rates were observed on the coastal margin of Western Australia at 30.7°S, EqIO at 2.4°S, and intermittently northwards at 5°N, 8.5°N, and 17.2°N (Figure S1.3). In contrast, the POC normalized accumulation rates were dampened in SIO gyre. The nutrient and hydrography profiles suggested upwelling at ~4-8°N, where two of the POC normalized accumulation peaks were observed (Figure S1.1). Thus, there appeared to be increased daily carbon accumulation in regions with elevated nutrient availability.

We found significant regional variation in the concentration and ratios of POC, PON, and POP (Figure 1.4 and Table S1.2). Particulate organic matter concentrations were lowest in SIO gyre and higher northwards (Table S1.1). In BoB, the POM concentrations decreased from 9°N to 15°N followed by a sharp increase in waters overlying the continental shelf (Figure 1.2D-F). Although the nutricline shoals, nutrients may be entrained below the thermocline due to strong salinity gradients in BoB leading to low POM concentrations (Prasanna Kumar et al., 2002). The elemental ratios followed similar declining northward trends, with high ratios in the SIO gyre and low ratios in the north. C:P and C:N decreased sharply during the transition from SIO Gyre (C:P 150, C:N 7.6) to EqIO (C:P 131, C:N 7.0), but stayed slightly above Redfield proportions in the EqIO and the BoB (C:P 127, C:N 7.1)(Figure 1.2G-I). N:P decreased gradually northward throughout the

transect (N:P: SIO gyre = 20.1 EqIO = 19.0, BoB = 17.9). Thus, there were clear regional differences in elemental ratios across the eastern Indian Ocean.

Testing ecological stoichiometry hypotheses

We next tested the three proposed stoichiometry models for POM stoichiometry trends in the Indian Ocean. First, we addressed the allometric diversity hypothesis. Consistent with past studies (Makino et al., 2003; Rusch et al., 2010), *Prochlorococcus* dominated the phytoplankton portion with only small contributions from picoeukaryotic phytoplankton and *Synechococcus*. The picoeukaryotic phytoplankton increased in biomass north and south of the equator, while the *Synechococcus* biomass increase centered on the equator. Residual effects of coastal upwelling could explain the increases in *Synechococcus* in the EqIO (Wiggert et al., 2009), but the overall *Synechococcus* contribution to phytoplankton composition was small. Larger phytoplankton were rare and the ratio of photo-to-heterotrophic plankton biomass was nearly 1:1 throughout the transect. A linear regression model showed no significant explanatory power of relative biomass composition for POM concentrations and elemental ratios (Table S1.3, Figure S1. 4). Instead, POM variation was explained equally well by a combination of a sinusoidal diel plus an either temperature or nutricline depth model (Figure S1. 5, Figure S1.6, Table S1.4, Table S1.5). The models lent support for both the translation-compensation and nutrient supply hypotheses. As such, we were statistically unable to distinguish between these two ecological stoichiometry hypotheses based solely on our Indian Ocean data.

To further understand how POM stoichiometry was regulated, we next compared the observed relationships for environmental variation and POM composition within the

Indian Ocean with previously seen global trends (Martiny et al., 2013)(Figure 1.5, Figure S1. 7). While the nutricline depth was positively related to POM elemental ratios for both the Indian Ocean and globally, the relationship for temperature flipped from negative in the Indian Ocean to globally positive. This suggests that the relationship between temperature and POM stoichiometry is not uniform. We further searched the global C:N:P database for all surface transects with strong temperature and nutricline depth correlations (Figure S1.8). This analysis confirmed the observations in the Indian Ocean, whereby the correlation between nutricline depth and POM stoichiometry was consistently positive. In contrast, the correlation between temperature and POM stoichiometry could be both positive and negative, leading us to reject the translation-compensation hypothesis. It is worth noting that all these cruises were from tropical and subtropical ocean leaving it currently unknown how temperature vs. nutrient supply control higher latitude POM ratios. Nevertheless, the analysis suggests that for at least low latitude regions, nutrient availability is the primary control on POM stoichiometry.

Proposed model relating N:P supply ratio to gyre POM C:N:P

While the POM C:P and N:P ratios in SIO were above Redfield proportions, they were still substantially lower than observed in several other low nutrient ocean regions. To further understand the biogeochemical controls on POM cycling, we compared the POM concentrations and ratios in SIO gyre to the North Atlantic, South Atlantic, North Pacific, and South Pacific subtropical gyres (Figure 1.6, Figure S1.9). The mean gyre concentration for POC, PON, and POP were 3.1 μM, 0.37 μM and 16 nM respectively and our observed concentrations in the SIO gyre were generally consistent with these levels (Table S1.6). However, there were also clear difference in the levels and ratios across gyres (Table S1.7,

ANOVA p-values < 1E-16). The South Indian and North Pacific observations had anomalously low median POM concentrations, the North Atlantic was near the mean, and the South Pacific and South Atlantic gyres had median POM concentrations at or above the means. Median C:P and N:P ratios were near or slightly above Redfield proportions in the SIO gyre (C:P = 147:1, N:P = 19:1), near the average in the North and South Pacific, and elevated in the North Atlantic subtropical gyre (C:P = 205:1, N:P = 33:1)(no POP data for the South Atlantic). Median C:N ratios ranged from 6.9 (North Atlantic gyre) to 9.0 (South Atlantic gyre). The highest C:N ratios were found in the gyres with the highest median POM concentrations. Thus, there were significant differences in POM ratios across gyres (Table S1.7).

We hypothesized that low iron (Fe) supply could influence the elemental ratios via Fe-controls on regional N_2-fixation rates and the relative degree of N vs. P stress (Figure 1.7) (Mather et al., 2008; Rembauville et al., 2016). In regions with low N_2-fixation rates, a relatively higher P vs. N availability would lead to lower POM C:P and vice-versa for regions with high rates leading to high POM C:P. Thus, Fe controls on N_2-fixation may influence the nutrient supply *ratio* of nitrogen versus phosphorus which in turn would affect POM C:P (Moreno & Martiny, 2018). Previously measured dissolved Fe concentrations (Grand et al., 2015; Tagliabue et al., 2012) in subtropical gyres have an inverse relationship with surface phosphate (Garcia et al., 2013) (Figure 1.7A). Here, the South Indian and South Pacific gyres have the highest phosphate concentrations, but lowest dissolved iron concentrations. The lowest PO4:Dfe concentration ratio was found in the North Atlantic gyre. To begin to evaluate this hypothesis, we measured ratios of POM iron to carbon and phosphorus. We detected lower labile particulate iron to POC (LPFe:C) ratios in the SIO gyre (17.8 nM/μM)

and typical of a low iron ecosystem (Table S1.1) This was seen for both labile and refractory pFe. In contrast, pFe:C was elevated in the EqIO (22.3 nM/μM) region and further increased into the Bay of Bengal (44.5 nM/μM) (Table S1.). Thus, there appeared to be lower iron stress north of EqIO and the highest degree of iron stress in the gyre. As such, the C:P ratio in the SIO compared to the North Atlantic gyre may be depressed due to lower Fe, lower P, and higher N availability (Figure 1.7B and C). The regional LPFe:C and LPFe:P mean ratios increased toward the north, further indicating reduced iron stress in the phytoplankton community in EqIO and BoB (Table S1.1). Thus, the elevated iron stress in the South Indian Ocean may suppress C:P in the gyre.

Discussion

The quantification of POM concentrations in the eastern Indian Ocean allowed us to test current hypotheses for how elemental ratios are regulated as well as identify regional differences in biogeochemical functioning. Our findings directly evaluate three proposed mechanisms (allometric diversity, temperature, and nutrient supply) that may explain deviations in POM stoichiometry. Consistent with past studies (Schlüter et al., 2011; Zwirglmaier et al., 2008), *Prochlorococcus* dominated the phytoplankton community and the ratio of photo-to-heterotrophic plankton biomass was nearly 1:1 throughout the transect. Thus, we only observed minor changes in the community structure leading us to reject the allometric diversity hypothesis. However, there are caveats to this conclusion. First, genetic diversity within groups (e.g., ecotypes) may determine growth physiology leading to unique elemental composition (Martiny et al., 2016). However, no systematic patterns have yet been determined at this level of phylogenetic resolution. Secondly, heterotrophic bacteria did constitute a slightly larger portion of the relative biomass when

C:P and C:N ratios were higher. We find this an unlikely driver as heterotrophic bacteria tend to have lower C:nutrient ratios in comparison to phytoplankton due to C limitation (Moreno & Martiny, 2018). Thus, there is little support that changes in plankton community composition is the primary control on POM stoichiometry in this region.

The unique environmental conditions in the Indian Ocean lead us to support the nutrient supply hypothesis for low latitude marine ecosystems. For this analysis, we assumed nutricline depth was a proxy for nutrient supply rates to the surface and that a deeper nutricline would be indicative of increased surface nutrient stress. We found that the C:P, N:P, and C:N ratios were highest in the SIO gyre and decreased when the nutricline shoaled around 10-12^{o}S. Northwards of this latitude, the Indian Ocean is subject to monsoonal circulation patterns and fine-scale variation in the elemental ratios corresponded to observed changes in the nutrient supply. All of the ratios remained above Redfield proportions, reflecting oligotrophic surface conditions during the intermonsoon season. Between 5^{o}S and 5^{o}N C:P and C:N ratios increased when nutrient concentrations declined below the mixed layer, but the ratios were elevated at the equator where a band of high chlorophyll was present off Sumatra. While the onset of upwelling in the tropical Indian Ocean is consistent, the magnitude is seasonally variable and underlying mechanisms are complex (Deshpande et al., 2017; Hood et al., 2017; Punyu et al., 2014; Strutton et al., 2015; Wyrtki, 1973). Furthermore, the positive phase of the Indian Ocean Dipole can influence surface circulation as well (Deshpande et al., 2017; Wiggert et al., 2009). Historically, upwelling is also observed off the Sri Lanka Dome near 5^{o}N, where POM concentrations were the highest and elemental ratios decreased (Hood et al., 2017; Schott et al., 2002). Within the Bay of Bengal, the elemental ratios flattened out in the stratified

Inter-Monsoon gyre until a final increase putatively driven by increased nutrient supply over the continental shelf in northern BoB. Thus, regional differences in the nutrient supply rates indicated by nutricline depth across the eastern Indian Ocean appeared to regulate POM concentrations and ratios.

Two cruise transects in the North Atlantic shared a positive relationship between temperature and nutrient supply and these provide further support of our hypothesis for how POM ratios are regulated. POM elemental ratios were reported as part of a FS Poseidon (Kahler) (Dietze et al., 2004) cruise (30^{o}W, 18^{o}N-31^{o}N) and a North Atlantic Bloom Experiment (NABE) (Passow & Peinert, 1993) cruise (33^{o}N, 21^{o}W to 18^{o}N, 30^{o}W). In both of these cruises, nutrient supply rates were the best predictor for POM ratios and the temperature relationship flipped in comparison to global trends (Figure S1.8). Since macronutrient supply rates are non-limiting in high latitude regions, other factors (e.g., light, temperature, and plankton growth physiology) likely control C:N:P in such biomes (Moreno & Martiny, 2018). In support, a recent study demonstrated that the elemental composition of a phytoplankton was highly regulated by the nutrient supply but the optimal composition (i.e., N:P at maximum growth) was temperature dependent (Thrane et al., 2017). Thus, there could be an interaction leading to a more pronounced temperature effect in high nutrient conditions, but we reject the translation-compensation hypothesis as the primary driver in low-latitude regions.

Stoichiometric variation on diel time scales was observed throughout the region. In support, studies of phytoplankton cultures (Clark et al., 2014; Lopez et al., 2016; Ng & Liu, 2016) and communities (Copin-Montegut & Copin-Montegut, 1978; Fraga, 1966; Fuhrman et al., 1985; Ng & Liu, 2016) show a peak in the carbon-nutrient ratio towards the end of

the photoperiod. A diel range in C:P of 60 and C:N of 2 were found in *Synechococcus* cultures, but barely any variation in the N:P ratio (Lopez et al., 2016). The peaks are primarily attributed to daytime fixed carbon storage and troughs from exudation and respiration at night (Granum et al., 2002; Lopez et al., 2016). The amplitude of C:P and C:N were larger in a culture than observed in the IO9N transect, which may be due to the presence of heterotrophic lineages or detrital material in field samples. The diel cycling of POC accumulation and degradation could also influence nutrient cycling within the whole microbial community. Diel changes in the surface area to volume ratio of phytoplankton can limit their nutrient uptake and the timing of their release of photosynthetically-derived nutrients can directly impact the ambient nutrient concentrations for heterotrophic bacteria. In addition, heterotrophic grazers could compensate for low-quality prey (high C:N, C:P) by increased feeding at night (Ng & Liu, 2016). It was unclear if the N:P ratio residuals displayed a diel cycle leading us to conclude that daily N and P uptake was fairly synchronized in this region. If N fixation played a large role during the IO9N transect, we would expect the N:P ratio to increase during the daytime (Capone et al., 1990) but the absence of this trend suggested depressed N-fixation rates. Our results illustrate that the amplitude of daily C:P and C:N peaks is of a comparable magnitude to changes in the ratios across ocean regions, but the lack of N:P cycling indicates a constraint on additional N inputs.

We hypothesized that low Fe supply depresses the elemental ratios via controls on N_2-fixation rates and the relative degree of N vs. P stress (Mather et al., 2008; Rembauville et al., 2016). In contrast, high Fe inputs and increased nitrogen fixation may lead to elevated N and intense P drawdown. We propose that this mechanism leads to divergent

C:P and N:P ratios in the North Atlantic Ocean vs. the South Indian Ocean gyre. In the eastern Indian Ocean, the regional LPFe:C and LPFe:P mean ratios increased toward the north, indicating northward positive gradient iron availability for the phytoplankton community (Table S1.1). Higher N-fixation rates in the Arabian Sea than at the equator and Southern Indian Ocean Gyre along 69^{o}E were attributed to higher dissolved iron in the Arabian Sea (Shiozaki et al., 2014). Our depressed C:P ratios in the SIO gyre are consistent with inverse model results and observations of the western SIO gyre (Copin-Montegut & Copin-Montegut, 1978; Teng et al., 2014). Thus, the SIO gyre may represent a low C:P extreme for ocean gyres. As such, the variations in particulate elemental ratios observed in the Indian Ocean are distinctive and impose new constraints on how ocean C:N:P is regulated.

Methods

Sample collection and analysis procedures

Seawater samples were collected during the RR1604 GO-SHIP IO9N cruise aboard *R/V Roger Revelle* from March 22-April 24, 2016. Transect coordinates began at 31° 02'01" S /110° 27'28"E off Western Australia and ended at 16° 44'15"N/90° 08'77"E in the Bay of Bengal (Figure 1.1). In total, samples for particulate organic carbon, nitrogen, and phosphorus were taken at 238 stations. Samples for particulate iron were collected from 24 separate trace-metal clean casts off the stern at 20 m depth. Flow cytometry samples for phytoplankton and Bacteria cell counts were collected from the mixed layer (~20m) at 31 GO-SHIP stations. All cruise POM data is available on BCO-DMO (https://www.bco-dmo.org/dataset/734915). Nutrients data for this cruise were provided by Jim Swift/SIO and Susan Becker/SIO and is available at https://cchdo.ucsd.edu (Swift & Becker, 2010).

Water was collected from a circulating seawater system distributed via plastic tubing for POC/PON/POP around 3m deep. An underway system was chosen to vastly increase sampling coverage, replicate number, and sample volume. The water intake is located near the ship sea chest, which may have missed particle production in the subsurface. The circulating seawater was never turned off during the entirety of the transect and kept at a constant flow. Water was passed through a 30µm nylon mesh (Small Parts #7050-1220-000-12) to remove larger plankton and particles from the sample. Each replicate was collected into a separate 8.5L plastic carboys (Thermo Scientific, Waltham, Massachusetts). In between stations, carboys were rinsed with 30 µm filtered sample water just prior to collection. Six 8 L seawater samples were divided into POC/PON and POP triplicates. Carboys were placed at ~45° angle to avoid particle settling below the nozzle. Each replicate was passed through a 25 mm pre-combusted (500°C for 5 h) GF/F filter (Whatman, Florham Park, New Jersey) with a nominal pore size of 0.7 µm. The vacuum filtration was an in-line setup with 25 mm filter holders connected to an aspirator pump at -0.08 MPa. POP filters were rinsed with 5 ml of 0.17 M Na_2SO_4 to remove traces of dissolved phosphorus from the filter. All filters were stored in pre-combusted aluminum packets and immediately frozen at -80°C during the cruise and -20°C for shipment.

Particulate Organic Carbon/Nitrogen

Prior to analysis, the filters for POC and PON were dried according to the JGOFS protocol(Ducklow & Dickson, 1994). The protocol has a detection range of 0.43-43.13 µM for POC and 0.037-7.39µM for PON in sea water(Ducklow & Dickson, 1994). First, the filters were dried in an incubator at 55°C for 24-48 h and then stored in a desiccator with concentrated HCl fumes for 24 h to remove inorganic carbonates. Secondly, the filters were

dried again at 55°C for 48 h before being folded and packed into pre-combusted tin capsules (CE Elantech, Lakewood, New Jersey). The packaged filters are analyzed on a CN FlashEA 1112 Elemental Analyzer (Thermo Scientific, Waltham, Massachusetts) against an atropine standard curve (chemical formula $C_{17}H_{23}NO_3$).

Particulate Organic Phosphorus

Particulate organic phosphorus (POP) were analyzed according to a modified ash-hydrolysis protocol(Lomas et al., 2010). Thawed filters were placed in along with a corresponding standard curve of KH_2PO_4. 2 mL of 0.017M $MgSO_4$ was added to the acid-washed glass vials containing filters and covered with pre-combusted aluminum foil. The vials were placed in an incubator at 90°C for 24 h and then combusted (500°C, 2 h). Once cooled, 5 mL 0.2 M HCl was added and incubated at 90°C for at least 30 min. Next, the supernatant plus 5 mL milli-Q water was mixed with 2:5:1:2 parts ammonium molybdate tetrahydrate, 5N sulfuric acid, potassium antimonyl tartrate, and ascorbic acid for 30 min. Finally, the standards and samples were analyzed on a spectrophotometer at a wavelength of 885 nm to determine POP concentration with an assay detection limit 0.1 nmol l^{-1}.

C:N, C:P, and N:P ratios

Each filter analyzed for both POC and PON was treated as a replicate with a corresponding POC/PON ratio. The ratios of POC/POP and PON/POP were taken from the mean concentrations. The standard deviation for C:P and N:P was calculated as a pooled sample:

$$\sigma_{CN} = \sqrt{((\Sigma(CN_i - CN_{ave})^2))/n}, \quad (1)$$

$$\sigma_{NP} = N_{ave}/P_{ave} \times (\sqrt{((\sigma_N/N_{ave})^2 + (\sigma_P/P_{ave})^2)}), \quad (2)$$

$$\sigma_{CP} = C_{ave}/P_{ave} \times (\sqrt{((\sigma_C/C_{ave})^2 + (\sigma_P/P_{ave})^2)}), \quad (3)$$

Relative Biomass Estimates

Samples for biomass were collected directly into 2 ml cryovials from Niskin bottles at sea, and fixed with freshly made and 0.2 µm filtered paraformaldehyde. After fixation for 1 hour at 4˚C in the dark, samples were frozen at -80˚C until analysis. Cell counts were run on a BD FACSJazz flow cytometer equipped a 200 mW 488 nm laser. *Prochlorococcus* was determined by forward scatter and red fluorescence, and *Synechococcus* distinguished by emission in the green and yellow wavelengths. Small eukaryotes were the autofluorescing cells outside of the cyanobacterial gates. Biomass estimates were based on literature values of carbon per cell based on geometric means of forward scatter for each group (Casey et al., 2013). Relative biomass estimates were used in this study.

Particulate and dissolved Fe

Trace metal samples were collected from 5L Teflon-coated Niskin-X bottles hung on Kevlar line. Niskin bottles were transferred to a clean bubble immediately after sample collection. Samples for dissolved metal analysis were filtered through acid-washed 0.4 µm polycarbonate filters using a vacuum filtration apparatus and acidified using Optima grade HCl. Particulate samples were collected by filtering directly from pressurized Niskin bottles onto 0.45 µm Supor membranes. All samples were handled and stored using trace metal clean protocols. Dissolved samples were analyzed using an ESI seaFAST SP2 coupled to a Perkin Elmer Nexion 350D ICP-MS. Samples were passed through an ESI preconcentration column and buffered in-line with ammonium acetate buffer. Metals were eluted off the column and analyzed in DRC mode using ammonia gas. Samples were quantified using

standard additions; each sample was spiked with 2 additions averaging roughly 100% and 200% of the sample concentration. Labile particulate metals were leached (Berger et al., 2008) and were analyzed using a Thermo Element 2 HR-ICP-MS (Twining et al., 2011).

Statistical Model Analysis

All analyses were completed in MATLAB. Nutricline depth was chosen as a proxy for nutrient supply, and was determined by a threshold nitrate concentration of 1 μM. Depth profiles of nitrate concentrations were analyzed using an AutoAnalyzer shipboard, run by the SIO HydroLab according to standard methods(Hydes et al., 2010). Mixed layer depths (MLD), isothermal layer depths, and barrier layer thickness were calculated according to Rao and Sivakumar(Rao & Sivakumar, 2003) (Figure S1.4). MLD is the depth where the change in potential density anomaly (σ_t) equals the surface $\sigma_{t(z=0)}$ plus a change in 0.5°C ($\mathbf{\Delta}$T) times the thermal expansion coefficient (dσ/dt).

Mixed layer depth (MLD), where $\sigma_{t(z=h)} = \sigma_{t(z=0)} + \mathbf{\Delta}T\ d\sigma/dt$, (4)

Isothermal layer depth (ITL), where $\theta = \theta_{(z=0)} + \mathbf{\Delta}T$, (5)

Barrier layer thickness (BLT) = ITL – MLD, (6)

SST values were from the underway temperatures by the Hydro Lab (HLT) using the following correction(Wanninkhof et al., 2016):

SST(estimated) = 0.001424*HLT^2 + 0.950053*HLT + 0.048227, (7)

Statistical models were fitted using one or two predictor variables (SST (° C), Nutricline Depth (m) or Mixed Layer Depth, as well as time)(Table S1.5). The models were also fitted against all stations south of 5N to examine the influence from the Bay of Bengal on the fits (Table S1.6). RMSE and R^2 were used to compare across models. If a daily diel rhythm was identified (Table S1.1, Figure S1.3), a sine function was added to the model with a fixed period of 24 h.

$$y = p(1)_y * \sin\left(\frac{\text{Tot Hrs}*2\pi}{24} + p(2)_y\right) + (p(3)_y + p(4)_y \times (\text{SST}, \text{Znut}, or\ \text{MLD}), \quad (8)$$

$$\text{where } y = \text{POC, PON, POP, C: P, C: N, or N: P}$$

Residuals between the points and 8-point moving average were used for comparing the diel cycles of POM concentrations and ratio at each station. Again, most of the variation could be equally explained by temperature or nutricline depth. Residuals between the points and 8-point moving average were used for comparing the diel cycles of POM concentrations and ratio at each station.

Global and Gyre Comparisons

The global observations of concentrations and ratios of particulate organic matter was an from updated POM database (Martiny et al., 2014). Nitrate concentrations and temperature values were taken at the nearest depth from monthly WOA13 values at 1km resolution (Garcia et al., 2013; Locarnini et al., 2013). For the gyre comparison, gyre coordinates were determined where the nutricline depth was greater than 150m for the North Atlantic, South Atlantic, North Pacific, South Pacific, and South Indian Oceans. The latitude blocks for each gyre are as follows: North Atlantic (90˚W to 5˚W); North Pacific

(120˚E to 100˚W); South Atlantic (60˚W to 10˚E); South Pacific (60˚W to 150˚E); South Indian (30˚E to 150˚E). A map and boxplot of observations from each gyre and the new Indian Ocean values are shown (Figure S1.7). Average gyre surface phosphate concentrations were taken from 0m WOA13 values over each gyre area (Figure 1.7) (Garcia et al., 2013). Average gyre surface dissolved iron concentrations were taken from all data point in the top 50m over each gyre surface area using the more recent Tagliabue et al. database (Tagliabue et al., 2012). For the global comparison, POM observations were filtered to only include the top 30m. Temperature and nutricline values were paired with the observations and normalized to the maximum values. Correlation coefficients and slopes were determined separately for the global database stations and the new Indian Ocean observations (Figure 1.5). The slopes were determined from a linear regression using a Monte Carlo Metropolis-Hastings algorithm developed for MatlabStan (Carpenter et al., 2017; Stan Development Team, 2017). The scatter plots, linear fits and correlations are shown in Figure S1. 6.

Data Availability

Particulate organic matter data that support the findings of this study has been deposited in BCO-DMO as cited: Martiny, Adam and Lomas, Michael (2018) Particulate organic matter (PON, POC, POP) concentrations collected on R/V Roger Revelle cruise RR1604 along the hydrographic line IO9 in the Eastern Indian Ocean from March to April 2016. Biological and Chemical Oceanography Data Management Office (BCO-DMO) https://www.bco-dmo.org/dataset/734915. Data for the GO_SHIP line I09N can be found at https://cchdo.ucsd.edu/.

Acknowledgements

We thank KH Andersen, F Primeau, and G Britten for their helpful comments. We thank the captain and crew of the SCRIPPS R/V *Roger Revelle*, the chief scientists L Barbero and C Rodriguez, and the science party on board the IO9N cruise. We also thank GO-SHIP coordinators Lynne Talley and Greg Johnson for their support in participating in the U.S. Global Ocean Carbon and Repeat Hydrography Program. The work was supported by the National Aeronautics and Space Administration Earth and Space Science Fellowship (NESSF16R to CAG) and NSF (OCE-1559002 to ACM and OCE-1559021 to MWL and BT).

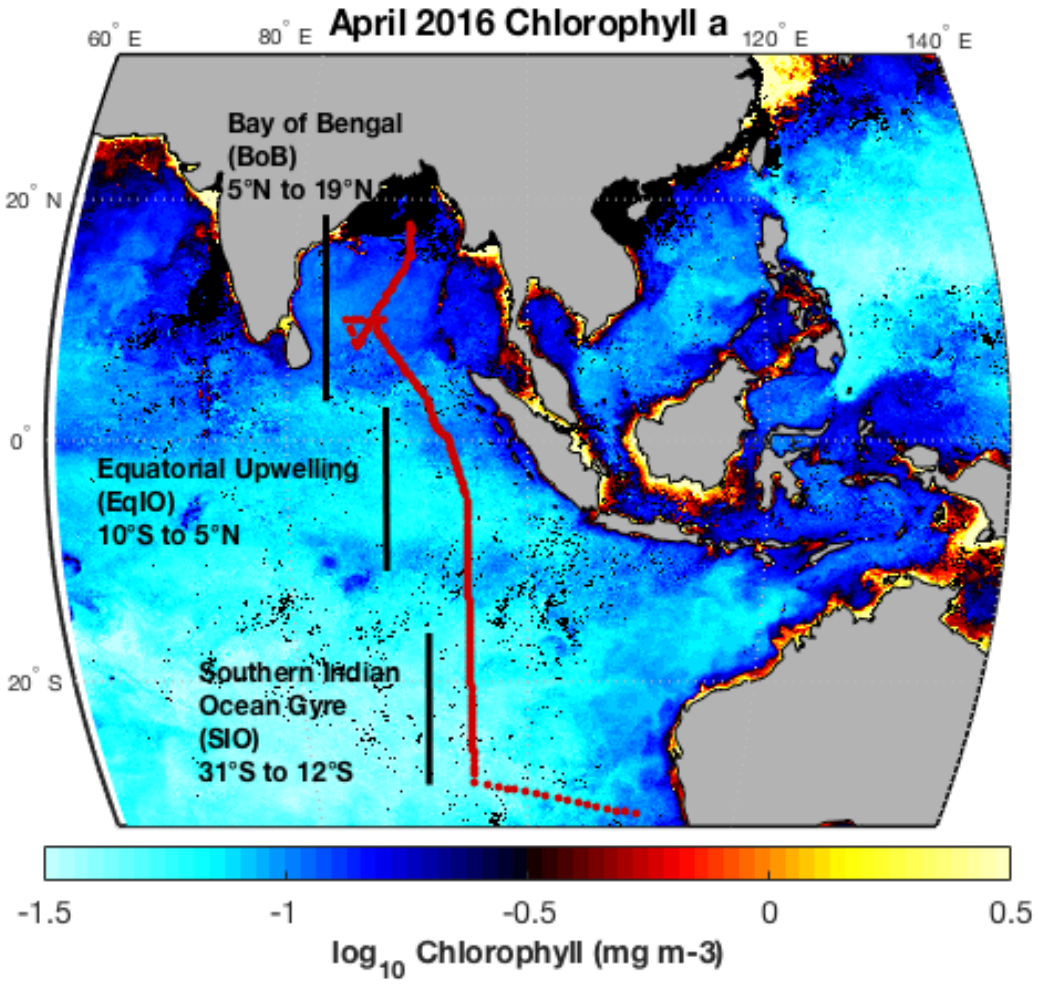

Figure 1.1. Study region. The transect sampling locations for GO-SHIP cruise IO9N are marked by the red dots. The approximate latitudinal range of proposed regions is marked by yellow bars. Chlorophyll concentrations are from MODIS-Aqua 4km April 2016 monthly average("NASA Goddard Space Flight Center, Ocean Ecology Laboratory, Ocean Biology Processing Group. Moderate-resolution Imaging Spectroradiometer (MODIS) Aqua Chlorophyll a 4km Data; NASA OB.DAAC, Greenbelt, MD, USA.," n.d.). Figure was created in MATLAB using fireice.m colormap package.

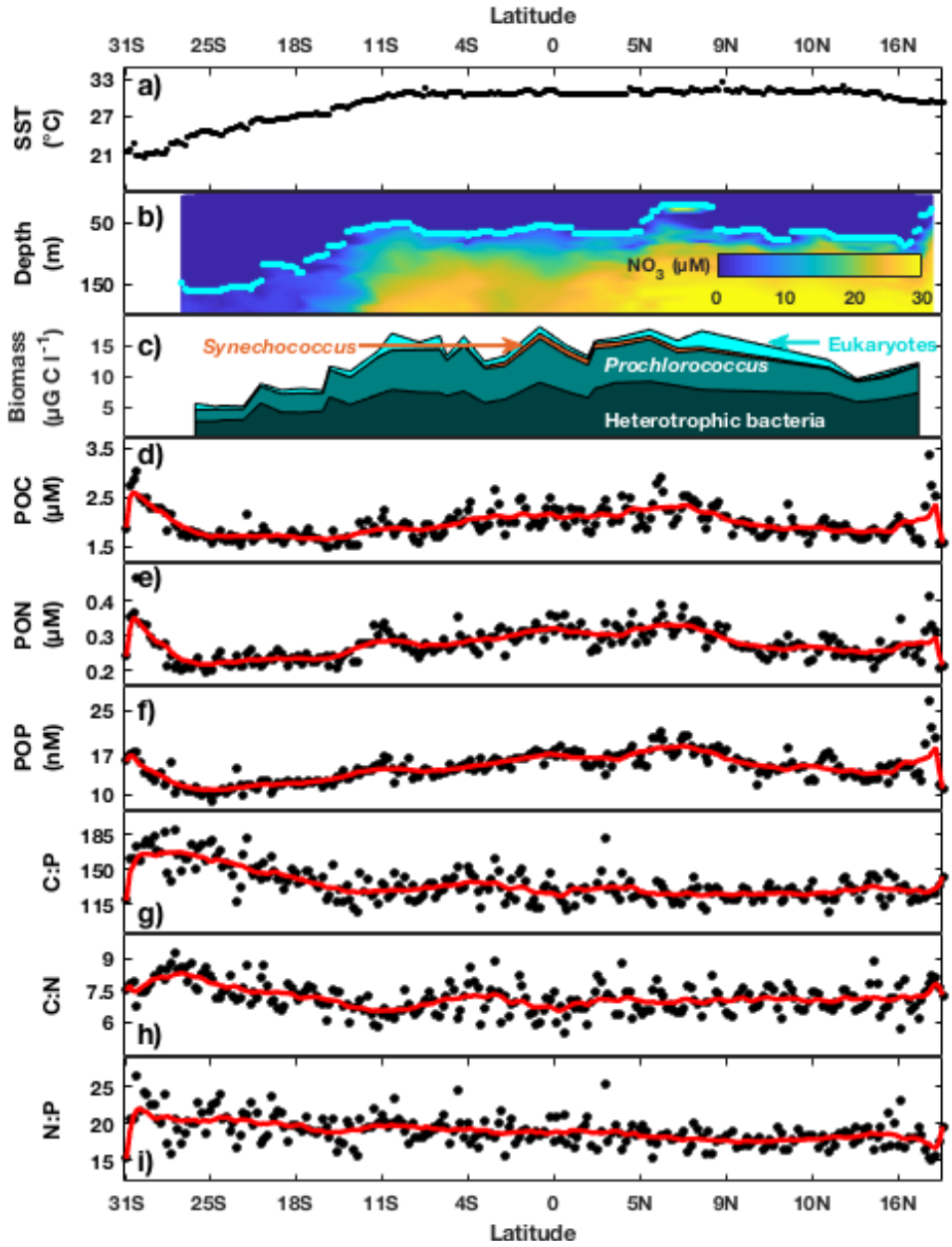

Figure 1.2. Observations of environmental conditions, relative phytoplankton biomass, and POM concentrations and ratios across the eastern tropical Indian Ocean; A) Sea surface temperatures; B) Nitrate concentrations as shaded background and nutricline depth (depth with 1 µM [NO_3]) marked by light blue dots; C) Phytoplankton relative biomass; D) particulate organic carbon (POC); E) particulate organic nitrogen (PON); F) particulate organic phosphorus (POP); G) POC:POP (C:P); H) POC:PON (C:N); and I) PON:POP (N:P). In panels D-I, averages of analytical triplicates are marked by black dots, the red line represents an 8-sample moving average, and elemental ratios are molar. First and last 4 end points are averaged over fewer than 8 points. For bacteria & phytoplankton: Bact(dark green) = Heterotrophic bacteria, Pro(greenblue) = *Prochlorococcus*, Syn(orange) = *Synechococcus*, and Euks(cyan) = Eukaryotes.

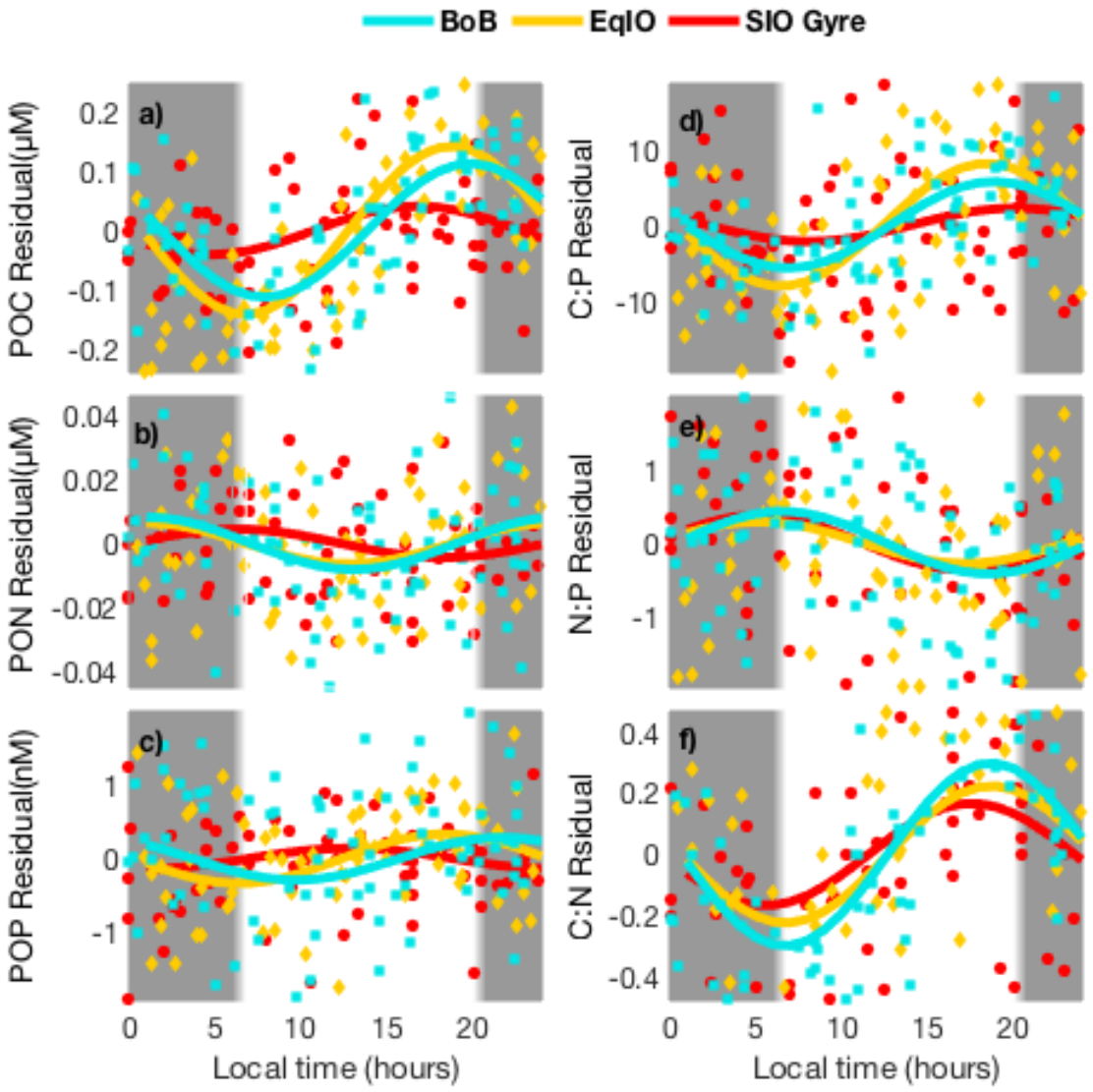

Figure 1.3. Diel variation in POM concentrations and ratios. Residuals are calculated as follows: data points subtracted from the 8-point smoothed line for A) particulate organic carbon (POC), B) particulate organic nitrogen (PON), C) particulate organic phosphorus POP, D) POC:POP (C:P), E) PON:POP (N:P), and F) POC:PON (C:N). Points were plotted and a sine curve was fitted for each region. Bay of Bengal (BoB) is in cyan. Equatorial Upwelling (EqIO) is in gold. Southern Indian Ocean gyre (SIO gyre) is in red. The grey bar represents local nighttime and white bar daytime.

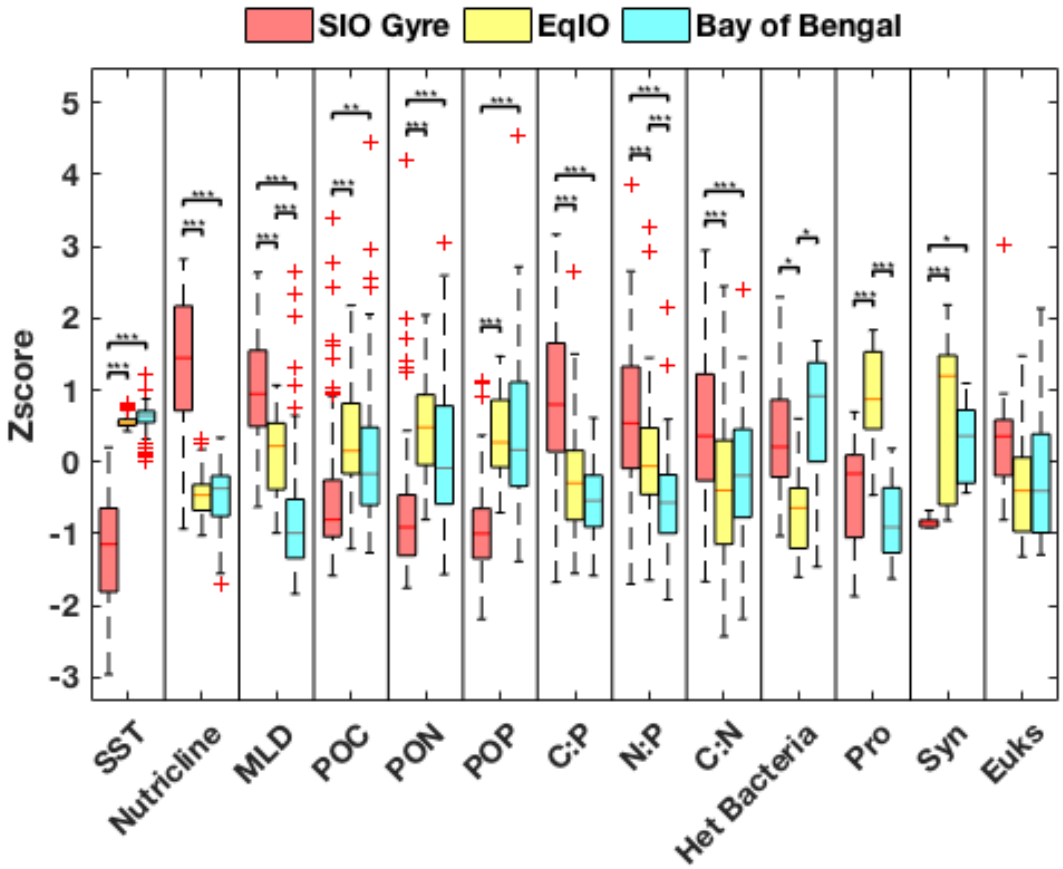

Figure 1.4. Regional variation in environmental parameters, relative biomass, and POM concentrations and ratios. Significant regional variation between specific regions is indicated by the number of stars (ANOVA, * = p <0.5, ** = p<0.01, *** = p<0.001). For relative biomass; Het bacteria = heterotrophic bacteria, Pro = *Prochlorococcus*, Syn= *Synechococcus*, and Euks = Eukaryotes.

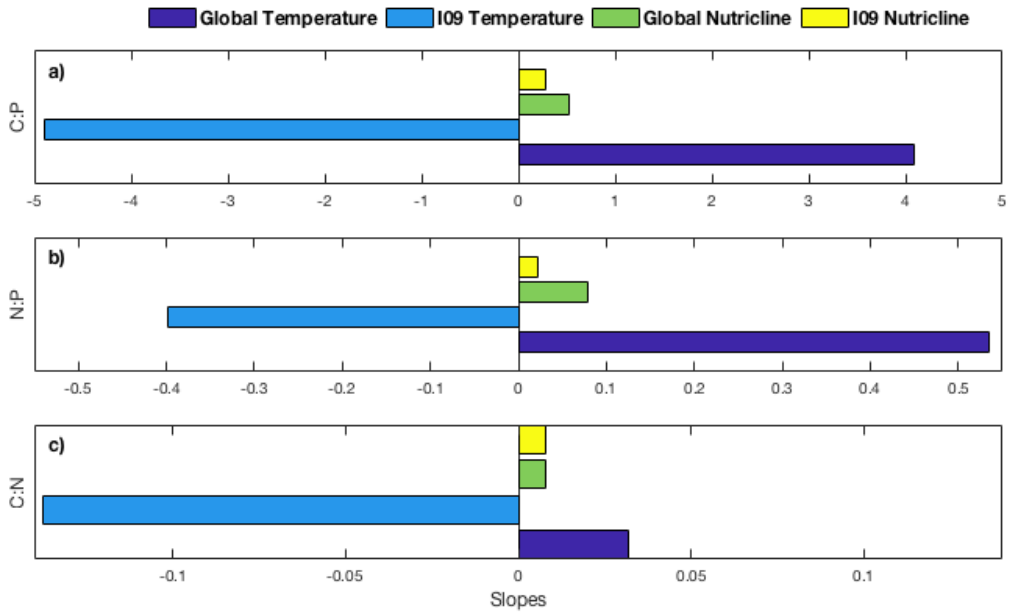

Figure 1.5. Global and Indian Ocean environmental correlations. Mean of slope estimates for global and Indian Ocean (IO9N) transect particulate organic matter (POM) concentrations and ratios. The sign of the slope indicates the average relationship between the POM concentration(ratio) and the enivironmental parameter (temperature or nutricline depth). Slopes are fitted to a linear regression model (see methods).

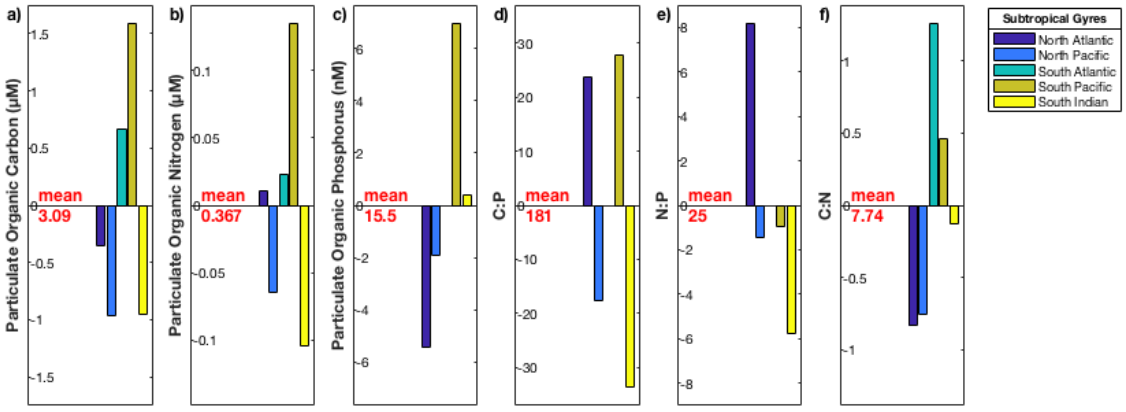

Figure 1.6. Gyre anomalies for particulate organic matter concentration and ratios. Anomalies are relative to gyre mean (red text) for A) particulate organic carbon (POC), B) particulate organic nitrogen (PON), C) particulate organic phosphorus (POP), D) POC:POP (C:P), E) PON:POP (N:P), and F) POC:PON (C:N). There are no POP, C:P, or N:P data for the South Atlantic gyre.

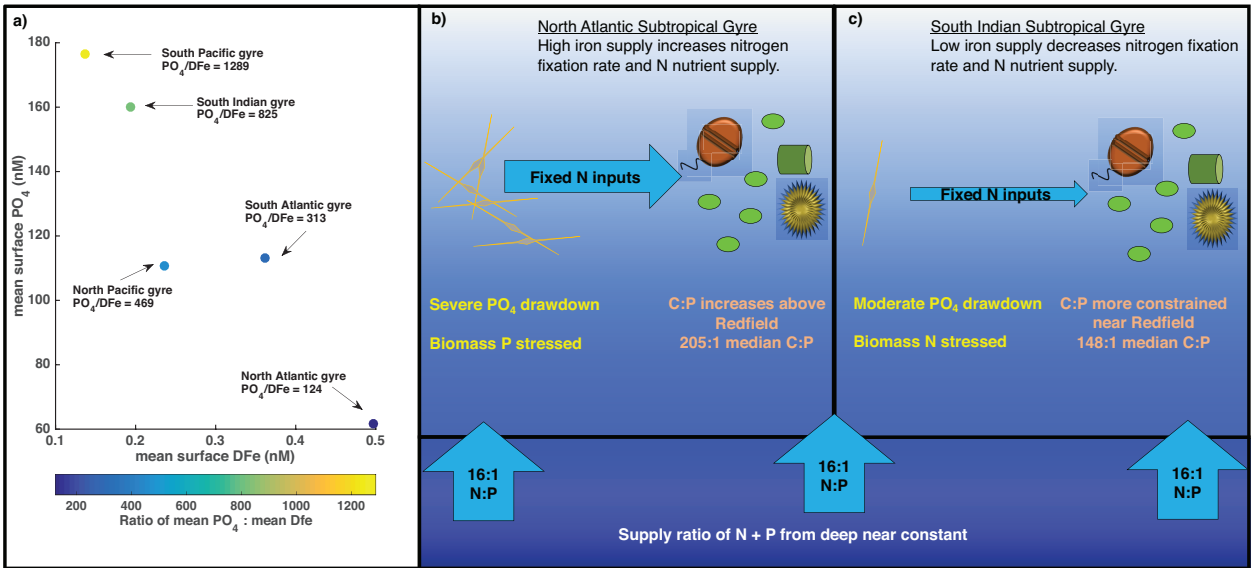

Figure 1.7. Conceptual model for regulation of ocean gyre biogeochemistry A) Nutrient levels across gyres: median surface phosphate to dissolved iron in top 50m. B) Iron Supply Model for C:P in North Atlantic and C) South Indian Ocean subtropical gyres. Median C:P values are from gyre comparison (North Atlantic, Table S1.6) and this cruise.

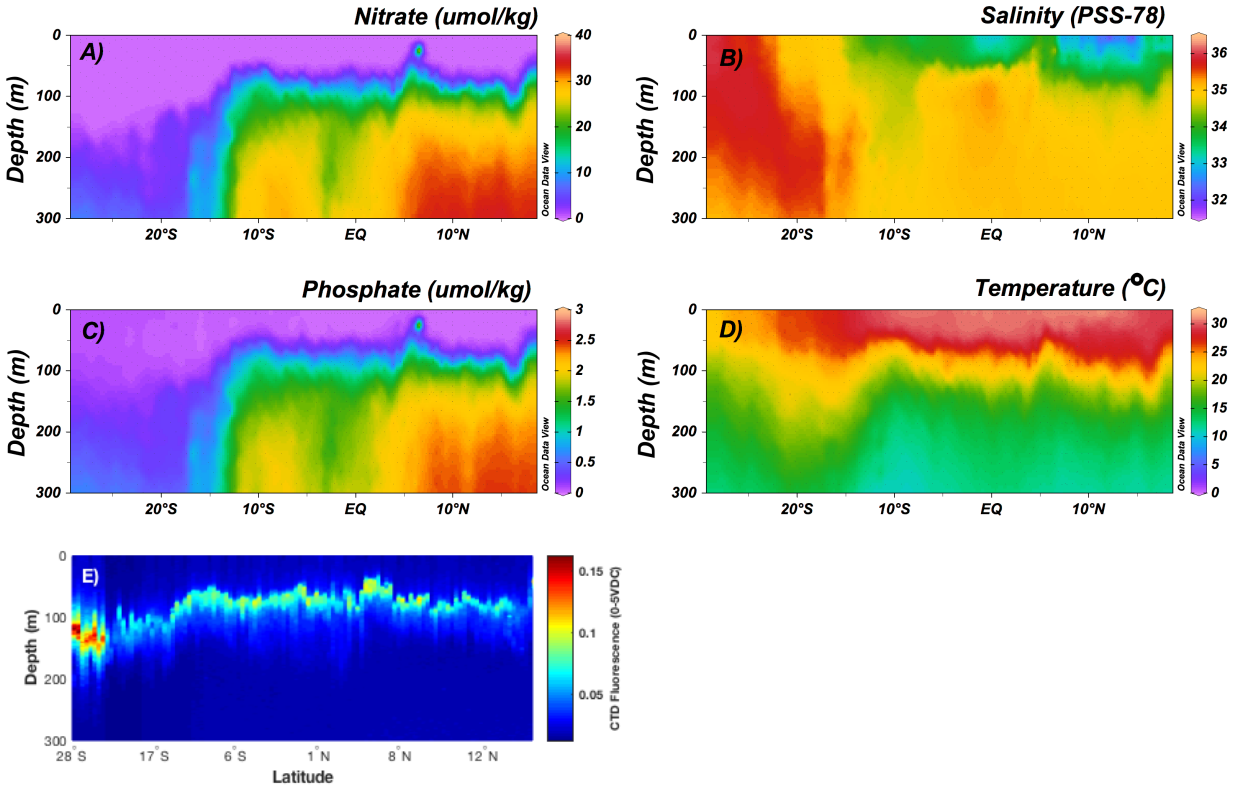

Figure S1.1. I09 GO-SHIP section profiles. From top to bottom: A) Nitrate (µmol/Kg), B) Salinity (PSS-78), C) Phosphate (µmol/Kg), and D) CTD temperature (°C). Images made in Ocean Data View. E) CTD fluorescence profiles mapped in MATLAB.

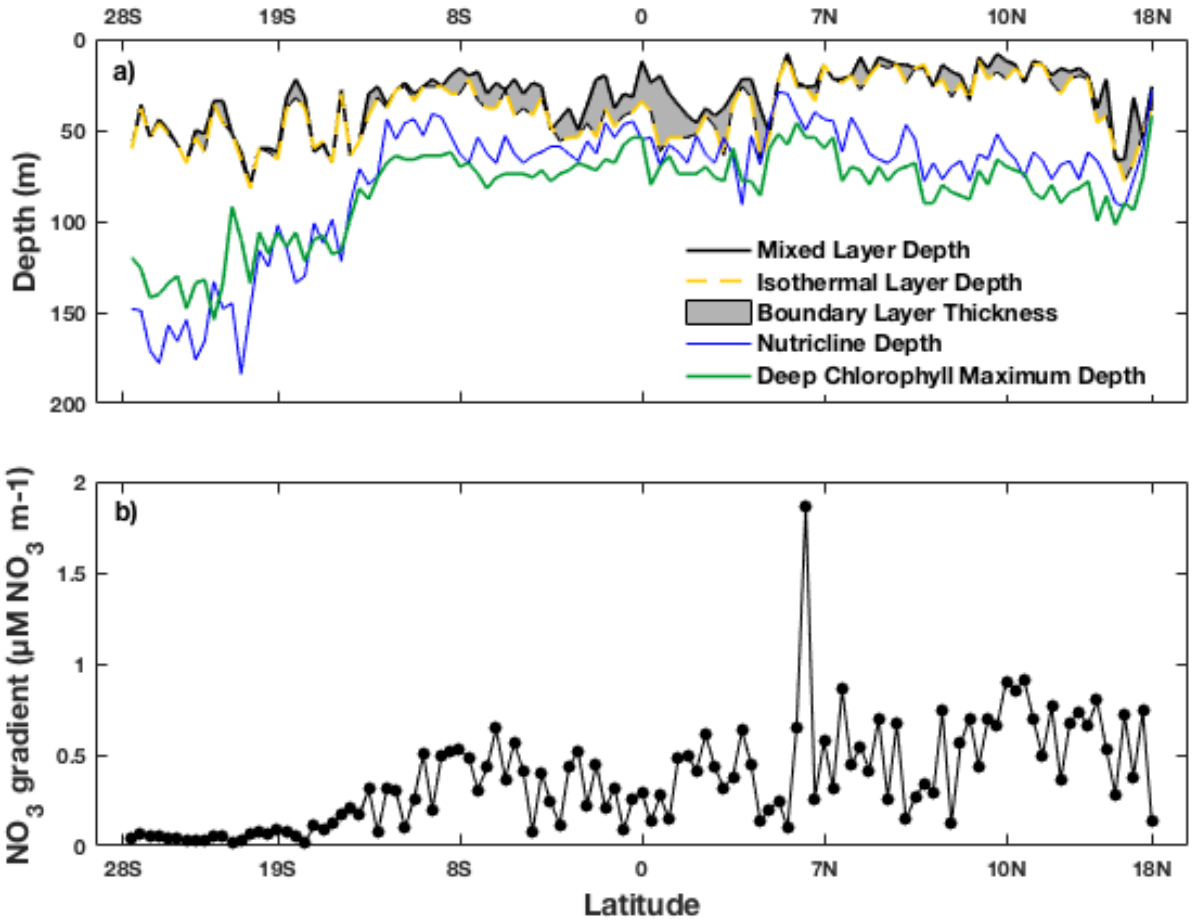

Figure S1.2. Surface layer depths and gradients. A) Mixed layer depth (black line), nutricline depth (blue line), isothermal layer (ITL) dashed red line, and the deep chlorophyll maximum (DCM) is the green line. The barrier layer thickness is shaded in grey between the MLD and ITL and thickest near the equator. Because nutricline and DCM depths were deeper than mixed layer depths, it is likely that biological uptake influenced nutricline depths in the SIO gyre and Bay of Bengal. B) NO_3 gradient calculated as change in concentration 10m below nutricline depth.

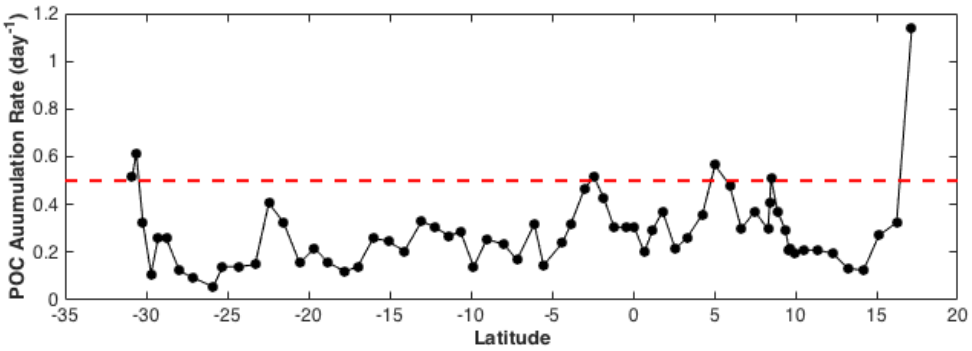

Figure S1.3. Daily accumulation rate of particulate organic carbon (POC). This is the peak to trough difference in daily POC divided by the minimum POC. Red dashed reference line is added at 0.5 day^{-1}.

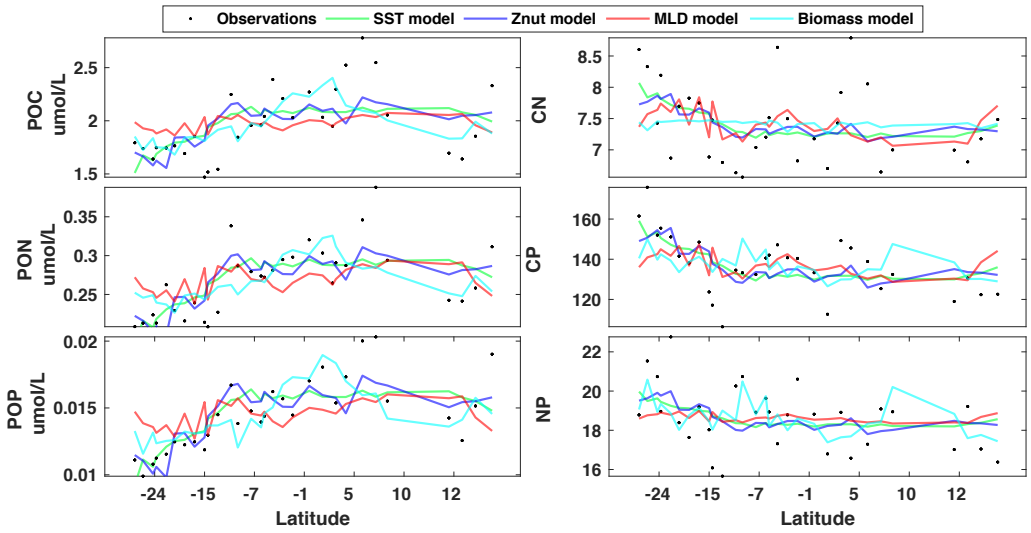

Figure S1.4. Linear Model β0 + β1*x1 + β2*x2 + β3*x3 + β4*x4. Lines are plotted predictions of POM concentrations and ratios at Biomass Stations for f(SST) -green, f(Znut) -blue, f(MLD)-red, f(bact,por,syn,euks)-cyan. The observations are ins black. SST = sea surface temperature. Znut = nutricline depth. MLD = mixed layer depth.

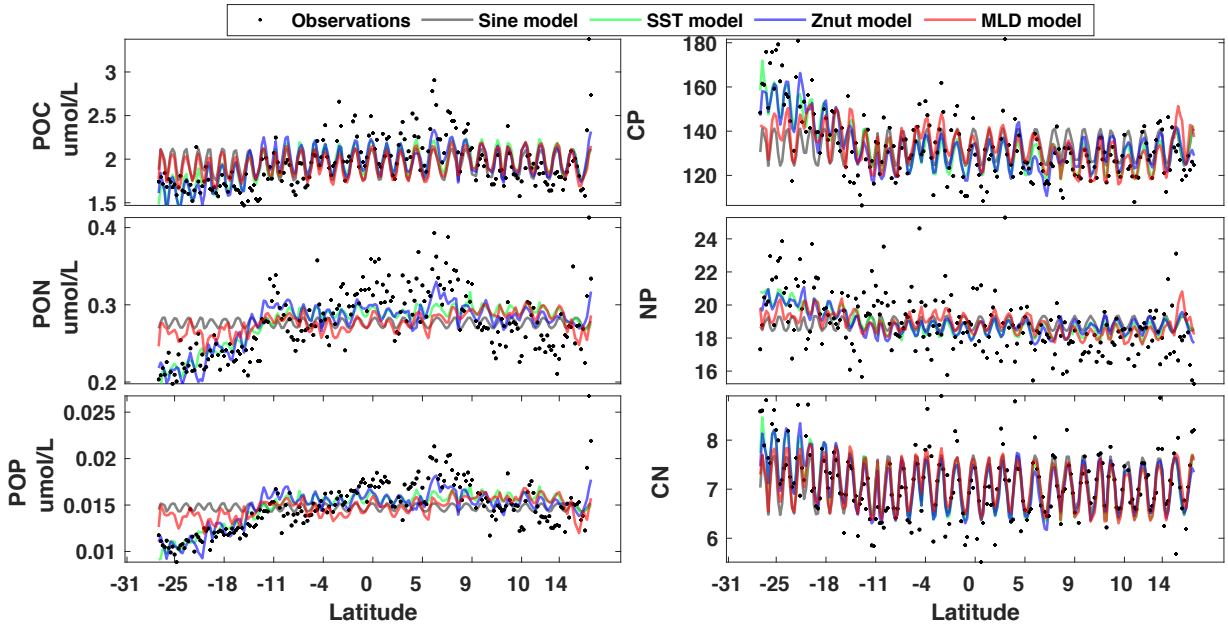

Figure S1.5. Nonlinear sine models with Bay of Bengal. A) Models for POM concentrations and ratios are described in methods. Observations (black circles) and model prediction (Sine-grey, SST-green, Znut-blue, MLD-red) for POC, POP, PON, C:P, N:P and C:N. B) The same except the Bay of Bengal stations above 5N are removed. SST = sea surface temperature. Znut = nutricline depth. MLD = mixed layer depth.

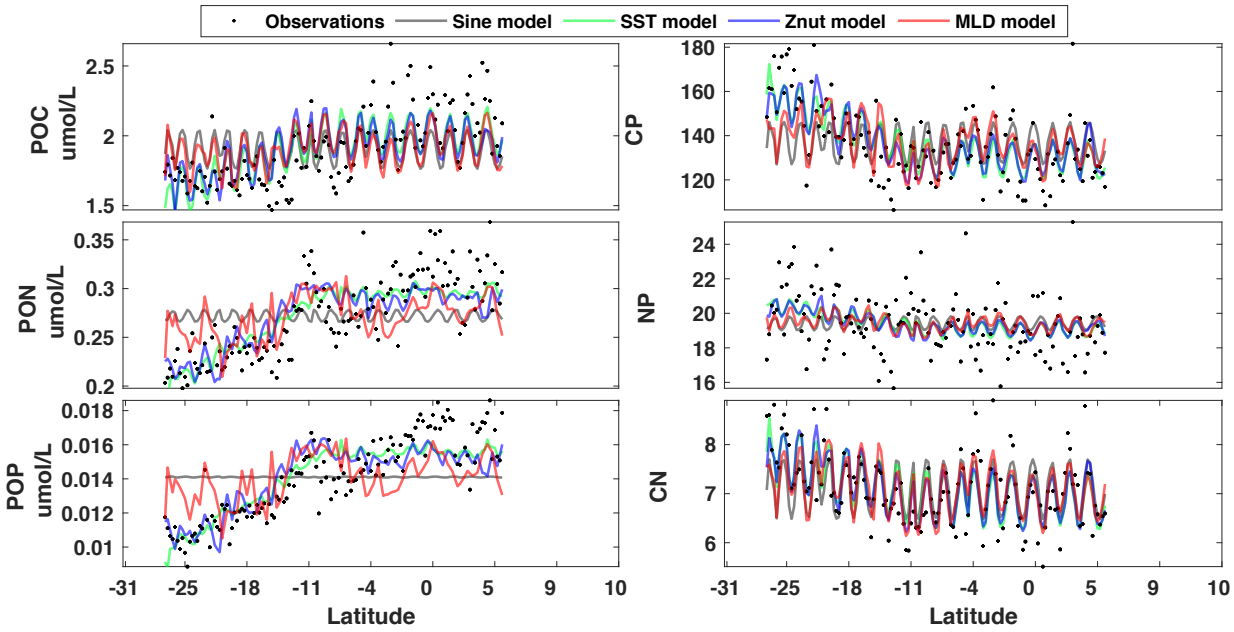

Figure S1.6. Nonlinear sine models without Bay of Bengal (<5N). A) Models for POM concentrations and ratios are described in methods. Observations (black circles) and model prediction (Sine-grey, SST-green, Znut-blue, MLD-red) for POC, POP, PON, C:P, N:P and C:N. B) The same except the Bay of Bengal stations above 5N are removed. SST = sea surface temperature. Znut = nutricline depth. MLD = mixed layer depth.

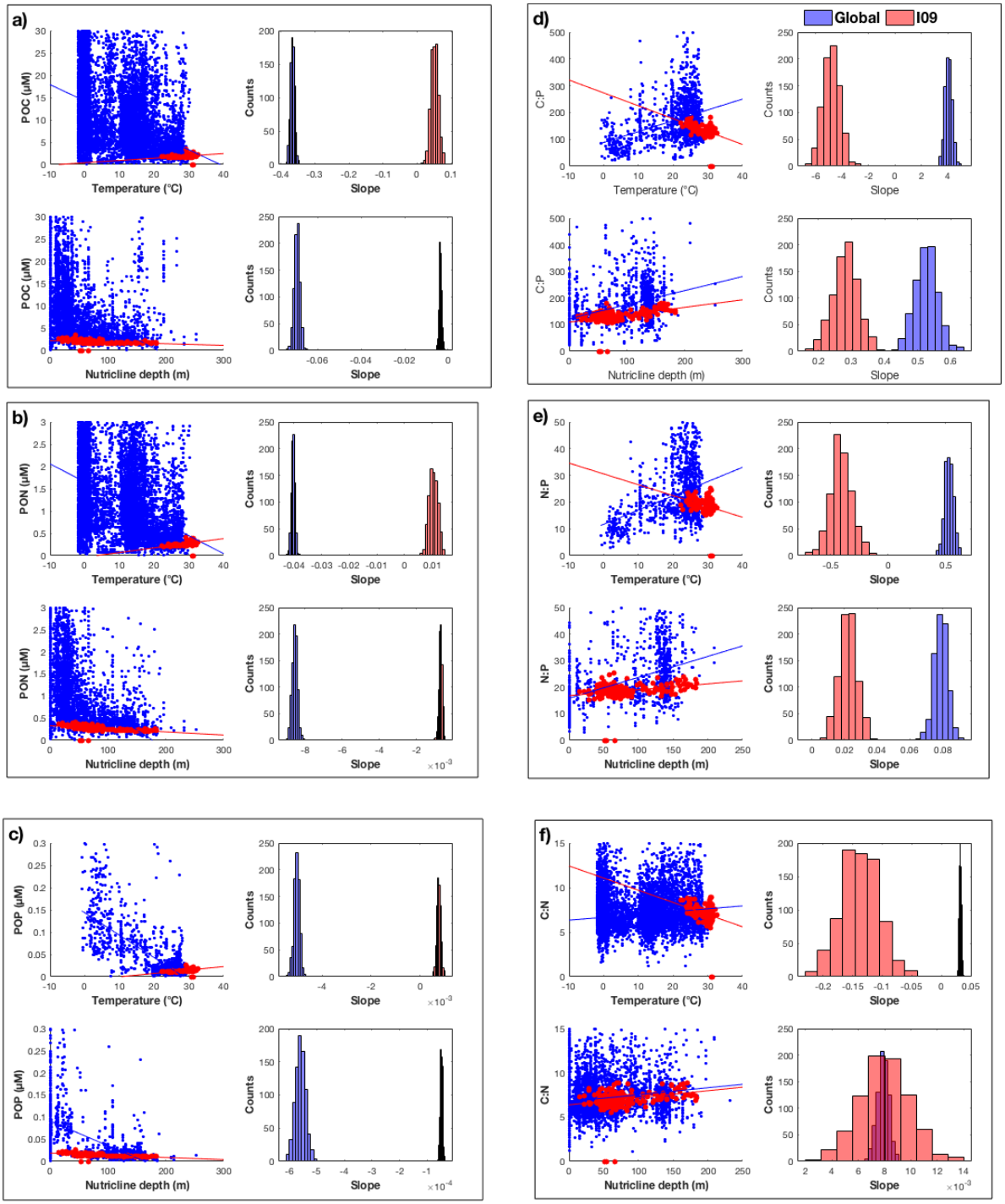

Figure S1.7. Comparison of global and IO9 POM concentrations and ratios to nutricline depth @ 1μM NO_3 and ocean temperature. The slopes are estimates at each station across 1000 iterations, and then averaged across each iteration for the histogram plots (total counts = 1000). The global observations and histogram slopes are in blue. The Indian Ocean observations are in red.

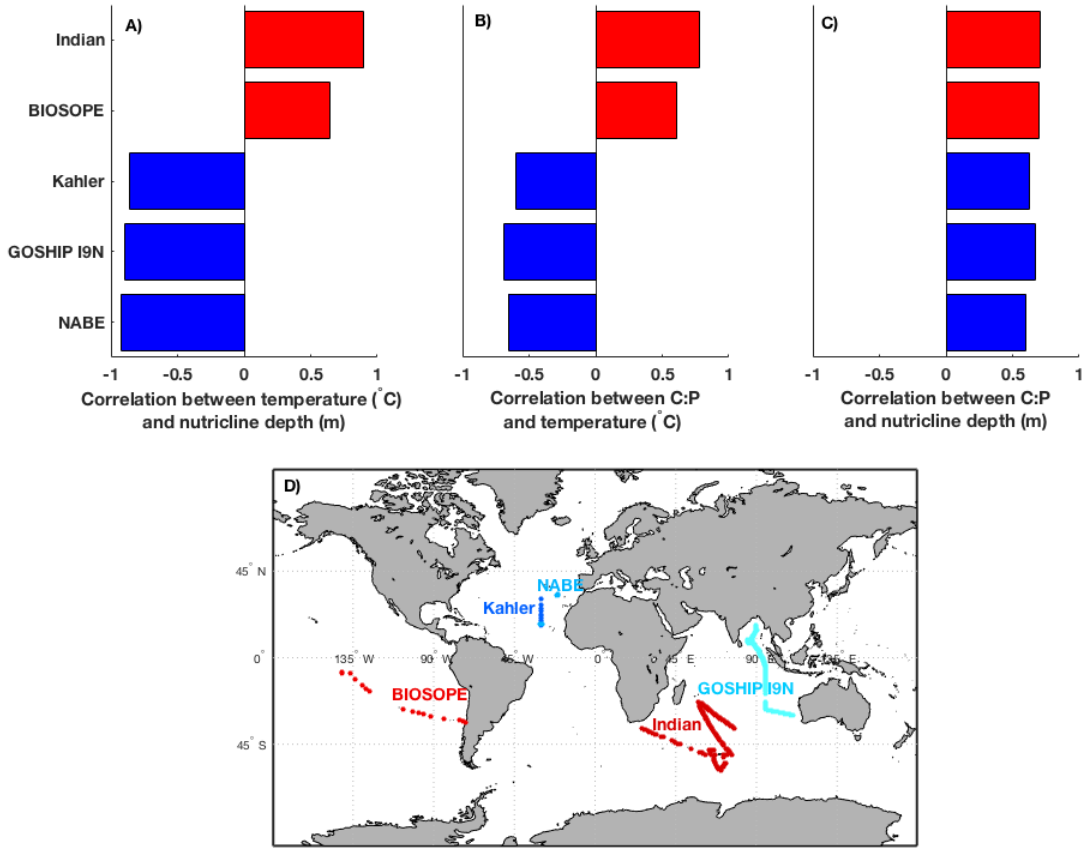

Figure S1.8. Correlation between temperature and nutricline depth among cruise transects with POC:POP (C:P) data, are shown for A) the correlation between temperature and nutricline depth, B) the correlation between particulate C:P ratio and temperature and C) the correlation between particulate C:P ratio and nutricline depth. This study eastern Indian Ocean transect is shown in cyan. Blue bars indicate negative correlations between temperature and nutricline depth of R < -0.5. Red bars indicate positive correlations between temperature and nutricline depth of R > 0.5. Y-axis shows cruise transects for global C:N:P database (Adam C Martiny et al., 2014). D) Map of station locations.

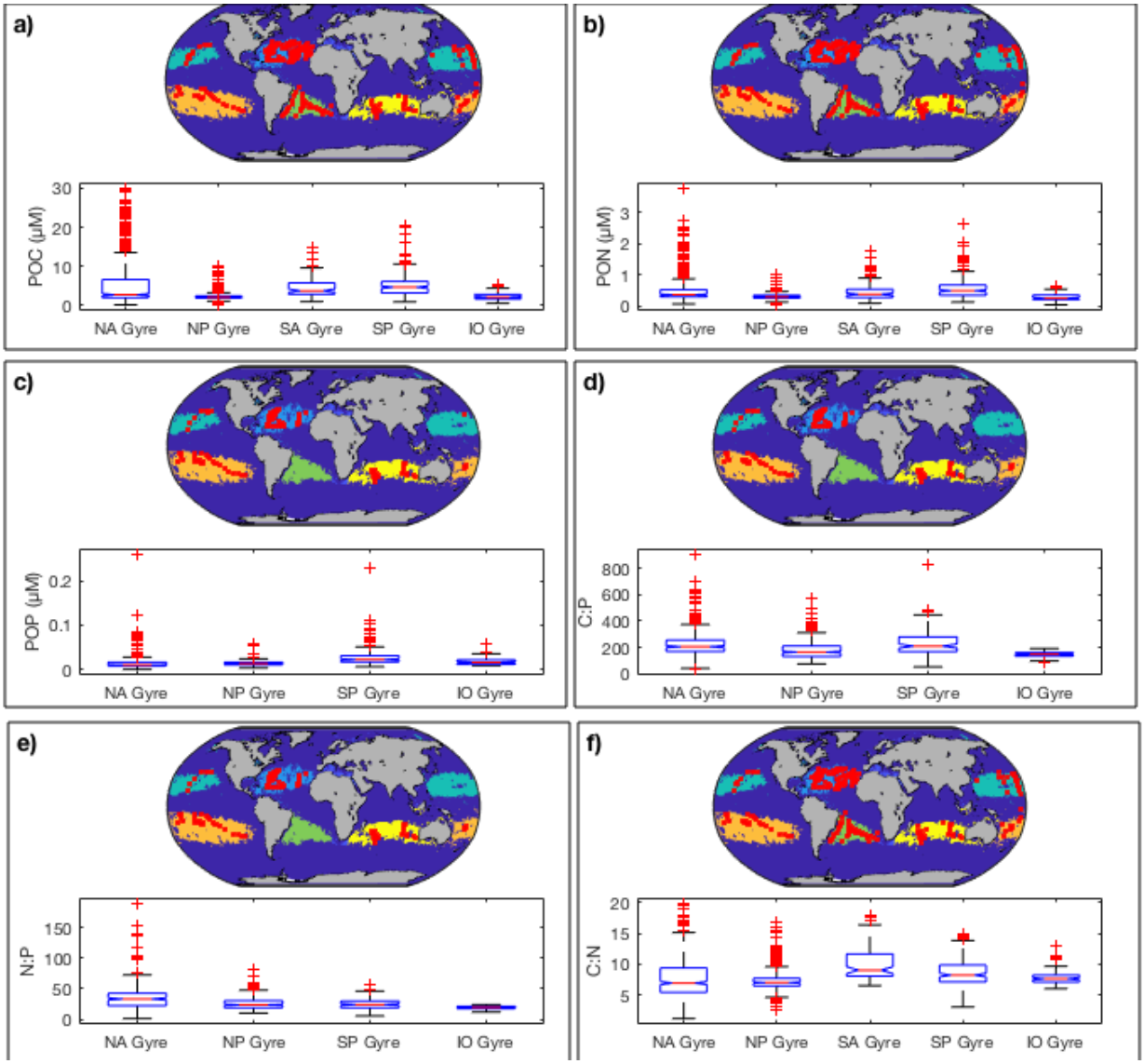

Figure S1.9. Gyre comparison of POM concentrations and ratios. Observations are included in gyres where nutricline depths at 5μM NO_3 are above 150m.

Table S1.1 Regional and transect averages for environmental parameters				
Region	**Indian Ocean Average**	**SIO Gyre**	**EqIO**	**Bay of Bengal**
Latitude	31°S to 19°N	31°S to 12°S	10°S to 5°N	5°N to 19°N
SST (C)	29.10 ± 2.91	25.33 ± 2.56	30.74 ± 0.26	30.79 ± 0.69
Nutricline (m)	78.1 ± 36.9	128.6 ± 36.7	61.6 ± 10.4	61.4 ± 17.0
Mixed Layer (m)	38.0 ± 16.3	53.7 ± 12.5	40.2± 9.4	26.5 ± 14.7
% *Prochlorococcus* biomass	51.8 ± 5.0%	53.9 ± 4.5%	48.6 ± 3.1%	54.9 ± 5.5%
% *Synechococcus* biomass	38.3±3.8%	36.6±2.9%	41.6±2.6%	35.1±2.4%
% Eukaryotes biomass	2.1± 2.0%	0.5± 0.2%	3.6± 2.3%	2.8± 1.2%
% Heterotrophic Bacteria biomass	7.7± 3.9%	9.0± 3.8%	6.2± 2.9%	7.1± 4.3%
Particulate organic carbon (µM)	1.97 ± 0.10	1.84 ± 0.12	2.05 ± 0.10	2.01 ± 0.08
Particulate organic nitrogen (µM)	0.28 ± 0.02	0.25 ± 0.03	0.30 ± 0.02	0.28 ± 0.02
Particulate organic phosphorus (nM)	14.70 ± 0.85	12.27 ± 0.90	15.71 ± 0.81	15.80 ± 0.78
C:P	135.30 ± 11.99	150.51 ± 15.87	131.14 ± 10.38	126.93 ± 8.79
N:P	19.00 ± 2.12	20.14 ± 2.82	19.00 ± 1.97	17.92 ± 1.44
C:N	7.17 ± 0.56	7.55 ± 0.85	6.96 ± 0.52	7.11 ± 0.34
Dissolved iron (nM)	0.15 ± 0.11	0.15 ± 0.05	0.08 ± 0.04	0.26 ± 0.14
Labile particulate iron (pM)	53.6 ± 30.9	32 ± 4	47 ± 17	89 ± 26
LPFe(nM): C(µM) (ratio of means)	26.5	17.8	22.3	44.5
LPFe (pM): P(nM) (ratio of means)	3.6	2.6	3	5.6
POC 24-hr residual amplitude (µM)	0.116	0.037	0.174	0.132
Local time of POC peak min (max)	7:00 (19:00)	5:00 (17:00)	7:00 (19:00)	8:00 (20:00)
PON 24-hr residual amplitude (µM)	5.9 x 10-3	5.5 x 10-3	7.9 x 10-3	9.1 x 10-3
Local time of peak min (max)	13:00 (01:00)	19:00 (07:00)	12:00 (24:00)	13:00 (01:00)
POP 24-hr residual amplitude (µM)	3.8 x 10-4	4.8 x 10-4	3.6 x 10-4	5.9 x 10-4
Local time of peak min (max)	8:00 (20:00)	4:00 (16:00)	7:00 (19:00)	8:00 (20:00)
C:P 24-hr residual amplitude	6.7	2.58	8.80	7.11
Local time of peak min (max)	7:00 (19:00)	8:00 (20:00)	6:00 (18:00)	7:00 (19:00)
N:P 24-hr residual amplitude	0.32	0.47	0.28	0.36
Local time of peak min (max)	17:00 (05:00)	18:00 (06:00)	17:00 (05:00)	18:00 (06:00)
C:N 24-hr residual amplitude	0.29	0.17	0.26	0.37
Local time of peak min (max)	6:00 (18:00)	4:00 (16:00)	6:00 (18:00)	7:00 (19:00)

Temperature, nutricline depth, mixed layer depth, percent relative biomass, particulate organic matter (POM) concentrations and ratios, dissolved iron, and labile particulate iron. Estimated amplitudes, peak minimum (min) local time and maximum (max) local time from fitted sine functions (see Figure 1.3) are shown for particulate organic carbon (POC), particulate organic nitrogen (PON), particulate organic phosphorus (POP), POC:POP, PON:POP, and POC:PON. SIO = Southern Indian Ocean, EqIO = Equatorial Indian Ocean.

Table S1.2. One-way ANOVA results Regional Differences					
SST ANOVA	SS	df	MS	F	Prob>F
Regions	1436.2	2	718.1	326.3	**<1E-16**
Error	497.3	226	2.2		
Total	1933.5	228			
Nutricline ANOVA	SS	df	MS	F	Prob>F
Regions	185406.9	2	92703.5	183.6	**<1E-16**
Error	105503.6	209	504.8		
Total	290910.5	211			
Mixed Layer ANOVA	SS	df	MS	F	Prob>F
Regions	25187.3	2	12593.7	81.0	**<1E-16**
Error	32481.7	209	155.4		
Total	57669.0	211			
POC ANOVA	SS	df	MS	F	Prob>F
Regions	1.9	2	0.9	10.0	**6.8E-05**
Error	20.7	223	0.1		
Total	22.5	225			
PON ANOVA	SS	df	MS	F	Prob>F
Regions	0.1	2	0.0	30.7	**1.7E-12**
Error	0.4	223	0.0		
Total	0.5	225			
POP ANOVA	SS	df	MS	F	Prob>F
Regions	0.0	2	0.0	65.1	**<1E-16**
Error	0.0	224	0.0		
Total	0.0	226			
POC:POP ANOVA	SS	df	MS	F	Prob>F
Regions	23223.3	2	11611.6	57.3	**<1E-16**
Error	45025.0	222	202.8		
Total	68248.2	224			
PON:POP ANOVA	SS	df	MS	F	Prob>F
Regions	186.1	2	93.1	31.4	**9.9E-13**
Error	658.2	222	3.0		
Total	844.4	224			
POC:PON ANOVA	SS	df	MS	F	Prob>F
Regions	13.2	2	6.6	15.3	**5.8E-07**
Error	95.7	223	0.4		
Total	108.9	225			

One-way ANOVA results for POM concentrations, ratios and environmental parameters. Regions defined as SIO Gyre (31°S to 12°S), EqIO (10°S to 5°N), and BoB (5°S to 20°N). SST = sea surface temperature, POC = particulate organic carbon, PON = particulate organic nitrogen, POP = particulate organic phosphorus, and POM = particulate organic matter. Sum of squares (SS), degree of freedom (df), mean squares (MS=SS/df), ratio of mean squared errors, F=MS(Regions)/MS(Error)

Table S1.3. Linear Model Coefficients and Statistics												
Ratio	LinModel	β0	β1	β2	β3	β4	N	DF	Fstat	pVal	R2	RMSE
C:P	f(SST)	232.0	-3.3	0.0	0.0	0.0	30	28	12.8	**0.001**	0.31	12.64
C:P	f(Znut)	120.3	0.2	0.0	0.0	0.0	30	28	13.4	**0.001**	0.32	12.54
C:P	f(MLD)	119.8	0.4	0.0	0.0	0.0	30	28	4.4	**0.045**	0.14	14.18
C:P	f(b,pro,syn,euks)	123.1	154.3	109.5	284.1	-142.4	30	25	1.2	0.337	0.16	14.79
N:P	f(SST)	24.4	-0.2	0.0	0.0	0.0	30	28	2.9	0.101	0.09	1.62
N:P	f(Znut)	17.4	0.0	0.0	0.0	0.0	30	28	4.6	**0.041**	0.14	1.58
N:P	f(MLD)	18.0	0.0	0.0	0.0	0.0	30	28	0.4	0.551	0.01	1.69
N:P	f(bact,pro,syn,euks)	16.5	17.0	14.1	36.4	-15.4	30	25	2.1	0.109	0.25	1.56
C:N	f(SST)	10.2	-0.1	0.0	0.0	0.0	31	29	5.1	**0.032**	0.15	0.59
C:N	f(Znut)	7.0	0.0	0.0	0.0	0.0	31	29	3.8	0.061	0.12	0.61
C:N	f(MLD)	6.7	0.0	0.0	0.0	0.0	31	29	4.2	**0.048**	0.13	0.60
C:N	f(bact,pro,syn,euks)	7.5	4.4	3.4	4.0	-4.4	31	26	0.0	0.996	0.01	0.68

Linear Model β0 + β1*x1 + β2*x2 + β3*x3 + β4*x4. Observations (n = 30/31) limited to stations with biomass estimates. SST = sea surface temperature (°C), Znut = nutricline depth (m), MLD = mixed layer depth(m), bact = Heterotrophic bacteria (ugC/L), pro = *Prochlorococcus* (ugC/L), syn = *Synechococcus* (ugC/L), euks = Eukaryotes (ugC/L). All biomass cells pre-filtered through 20µm mesh. All POM concentrations used for C:N:P ratios pre-filtered through 30µm mesh. ANOVA results are for linear model against constant model.

Table S1.4. Models fits for POM concentrations and ratios								
Ratio/POM	NonlinModel	p(1)	p(2)	p(3)	p(4)	N obs	R^2	RMSE
POC (µM)	f(hour)	-0.18	6.07	1.94	0.00	216	0.19	0.263
POC (µM)	f(hours,SST)	-0.18	6.12	0.17	0.06	216	0.39	0.230
POC (µM)	f(hours,Znut)	-0.18	6.10	2.25	0.00	216	**0.44**	**0.219**
POC (µM)	f(hours,MLD)	0.18	2.94	2.07	0.00	216	0.23	0.258
PON (µM)	f(hour)	0.01	1.75	0.28	0.00	216	0.01	0.042
PON (µM)	f(hours,SST)	0.01	1.78	-0.07	0.01	216	0.37	0.034
PON (µM)	f(hours,Znut)	0.01	1.83	0.34	0.00	216	**0.46**	**0.031**
PON (µM)	f(hours,MLD)	0.01	1.69	0.31	0.00	216	0.10	0.040
POP (µM)	f(hour)	0.00	5.89	0.01	0.00	217	0.01	2.6E-03
POP (µM)	f(hours,SST)	0.00	6.17	-0.01	0.00	217	0.46	1.9E-03
POP (µM)	f(hours,Znut)	0.00	2.91	0.02	0.00	217	**0.54**	**1.8E-03**
POP (µM)	f(hours,MLD)	0.00	2.74	0.02	0.00	217	0.15	2.4E-03
C:P	f(hour)	8.42	3.01	132.78	0.00	215	0.16	13.859
C:P	f(hours,SST)	-8.60	6.07	256.91	-4.19	215	**0.52**	10.475
C:P	f(hours,Znut)	-8.38	6.11	113.64	0.24	215	**0.52**	10.474
C:P	f(hours,MLD)	8.68	2.99	117.77	0.39	215	0.33	12.337
N:P	f(hour)	0.46	0.53	18.89	0.00	215	0.03	1.756
N:P	f(hours,SST)	0.48	0.63	28.08	-0.31	215	**0.18**	**1.625**
N:P	f(hours,Znut)	0.48	0.57	17.55	0.02	215	**0.16**	**1.641**
N:P	f(hours,MLD)	0.45	0.58	17.57	0.03	215	0.13	1.669
C:N	f(hour)	-0.61	0.05	7.08	0.00	216	0.40	0.522
C:N	f(hours,SST)	-0.61	0.02	10.21	-0.11	216	**0.52**	**0.470**
C:N	f(hours,Znut)	-0.60	0.04	6.58	0.01	216	**0.53**	**0.465**
C:N	f(hours,MLD)	-0.61	0.04	6.75	0.01	216	0.45	0.504

Models fits for POM concentrations and ratios are described in methods. SST = sea surface temperature (°C), Znut = nutricline depth (m), MLD = mixed layer depth(m).

Table S1.5. Models fits without Bay of Bengal								
Ratio/POM	NonlinModel	p(1)	p(2)	p(3)	p(4)	N obs	R^2	RMSE
POC (µM)	f(hour)	-0.14	6.18	1.90	0.00	137	0.15	0.239
POC (µM)	f(hours,SST)	-0.15	6.23	0.04	0.06	137	**0.51**	**0.182**
POC (µM)	f(hours,Znut)	-0.15	6.21	2.19	0.00	137	0.42	0.198
POC (µM)	f(hours,MLD)	-0.14	6.21	2.20	-0.01	137	0.26	0.223
PON (µM)	f(hour)	0.01	0.88	0.27	0.00	137	0.01	0.042
PON (µM)	f(hours,SST)	0.00	0.99	-0.11	0.01	137	**0.60**	**0.027**
PON (µM)	f(hours,Znut)	0.00	1.45	0.34	0.00	137	0.53	0.029
PON (µM)	f(hours,MLD)	0.00	0.88	0.35	0.00	137	0.26	0.036
POP (µM)	f(hour)	0.00	1.76	0.01	0.00	136	0.00	2.4E-03
POP (µM)	f(hours,SST)	0.00	0.65	-0.01	0.00	136	**0.71**	**1.3E-03**
POP (µM)	f(hours,Znut)	0.00	0.19	0.02	0.00	136	0.63	1.4E-03
POP (µM)	f(hours,MLD)	0.00	0.51	0.02	0.00	136	0.30	2.0E-03
C:P	f(hour)	9.58	3.04	136.59	0.00	136	0.17	15.377
C:P	f(hours,SST)	9.15	2.97	253.19	-4.03	136	**0.50**	**11.924**
C:P	f(hours,Znut)	8.51	2.98	115.53	0.24	136	**0.52**	**11.719**
C:P	f(hours,MLD)	9.36	3.00	112.44	0.53	136	0.34	13.660
N:P	f(hour)	0.41	0.78	19.42	0.00	136	0.03	1.779
N:P	f(hours,SST)	0.45	0.78	25.67	-0.22	136	**0.11**	**1.708**
N:P	f(hours,Znut)	0.47	0.72	18.34	0.01	136	**0.11**	**1.713**
N:P	f(hours,MLD)	0.43	0.79	18.31	0.02	136	0.06	1.754
C:N	f(hour)	-0.61	0.10	7.09	0.00	137	0.35	0.593
C:N	f(hours,SST)	-0.59	0.08	10.82	-0.13	137	**0.53**	**0.505**
C:N	f(hours,Znut)	0.57	3.24	6.40	0.01	137	**0.55**	**0.495**
C:N	f(hours,MLD)	-0.60	0.08	6.21	0.02	137	0.47	0.535

Bay of Bengal stations not included. Models fits for POM concentrations and ratios are described in methods. SST = sea surface temperature (°C), Znut = nutricline depth (m), MLD = mixed layer depth(m).

Table S1.6. Median gyre POM concentrations and ratios						
	North Atlantic Gyre	North Pacific Gyre	South Atlantic Gyre	South Pacific Gyre	South Indian Gyre	Gyre Mean
POC (μM)	2.7	2.1	3.8	4.6	2.1	3.07
PON (μM)	0.377	0.302	0.390	0.448	0.261	0.356
POP (μM)	0.010	0.014	-	0.031	0.016	0.018
POC:POP	205.0	163.7	-	177.5	147.7	173.5
PON:POP	33.2	23.6	-	18.9	19.3	23.7
POC:PON	6.9	7.0	9.0	8.1	7.6	7.7

Median POM concentrations and ratios from surface observations. No POP, C:P, and N:P data points are available for the South Atlantic gyre.

Table S1.7 One-way ANOVA for gyre regions					
POC ANOVA	SS	df	MS	F	Prob>F
Regions	4432.1	4	1108.0	52.5	**<1E-16**
Error	35449.5	1680	22.1		
Total	39881.6	1684			
PON ANOVA	SS	df	MS	F	Prob>F
Regions	19.7	4	4.9	46.5	**<1E-16**
Error	166.7	1576	0.1		
Total	186.4	1580			
POP ANOVA	SS	df	MS	F	Prob>F
Regions	3.1E-2	3	1.0E-2	47.7	**<1E-16**
Error	2.5E-1	1149	2.2E-4		
Total	2.8E-1	1152			
POC:POP ANOVA	SS	df	MS	F	Prob>F
Regions	764126.7	3	254708.9	30.9	**<1E-16**
Error	7495867.9	910	8237.2		
Total	8259994.5	913			
PON:POP ANOVA	SS	df	MS	F	Prob>F
Regions	27331.6	3	9110.5	43.8	**<1E-16**
Error	183332.3	881	208.1		
Total	210663.9	884			
POC:PON ANOVA	SS	df	MS	F	Prob>F
Regions	787.5	4	196.8	33.4	**<1E-16**
Error	8985.3	1525	5.9		
Total	9772.7	1529			

One-way ANOVA results for POM concentrations and ratios. Regions analyzed are the North Atlantic, South Atlantic, North Pacific, South Pacific, and South Indian gyres. POC = particulate organic carbon, PON = particulate organic nitrogen, POP = particulate organic phosphorus, and POM = particulate organic matter. For POC:POP, POP, and PON:POP there are no observations from the South Atlantic. Sum of squares (SS), degree of freedom (df), mean squares (MS=SS/df), ratio of mean squared errors, F=MS(Regions)/MS(Error).

CHAPTER 2

Remote sensing of global ocean surface phosphate concentrations

Co-authors: Toby Westberry, Michael Behrenfeld, and Adam Martiny.

Abstract

Regional variations in dissolved inorganic phosphate (DIP) influence cellular physiology, ocean productivity, and cycling between bio-limiting nutrients. However, we have not developed a robust global remote sensing (RS) estimate of surface DIP. Here, we aim to assess the variation in DIP using a mechanistic framework; capturing multiple axes of variation including latitudinal, between tropical upwelling vs downwelling regions, among subtropical gyres and between polar oceans. We then matched 34 RS inputs to each axis of variation and used artificial neural network analysis to predict the observed distribution of DIP. The RS inputs of sea surface temperature, net primary productivity, total dust deposition, and sea surface salinity captured 77% of total variation in surface DIP. Uncertainty in predicting ultralow DIP among oligotrophic regions is improved with high sensitivity measurements but remains a large source of variation. The contribution of RS inputs associated with iron deposition indicates the importance of micronutrient co-limitation in estimating regional DIP drawdown. By examining the interactions among the inputs and DIP in major ocean biomes, we find an unsupervised neural network model matches our mechanistic understanding. Thus, the combination of a mechanistic model for nutrient supply and demand combined with artificial neural networks provided a robust basis for developing a remote sensing estimation of surface DIP.

Keywords: phosphate, remote sensing, neural network models, marine nutrients

Introduction

Dissolved inorganic phosphate (DIP) is one of the major bio-limiting nutrients. DIP is suggested to be the ultimate limiting nutrient over geologic timescales (Tyrrell, 1999) and can locally limit primary production and other ocean biological processes (Mills et al., 2008; Mills et al., 2004; Moore et al., 2013; Moutin et al., 2005, 2008). Thus, it is important to identify the spatial and temporal variation in DIP. Currently, DIP is predominantly measured from CTD bottles using laborious techniques leading to large spatial or temporal gaps in coverage. Thus, we lack either autonomous or remote sensing approaches to consistently estimate variation in DIP.

There is systematic heterogeneity in DIP concentrations ([DIP]). First, [DIP] is low in tropical and subtropical waters and increases poleward due to a latitudinal gradient in stratification and phytoplankton nutrient drawdown (Falkowski et al., 1992). Secondly, [DIP] is elevated in regions with upwelling. Thirdly, there are subtle gradients within oligotrophic regions (Martiny et al., 2019; Wu et al., 2000). Using high-sensitivity techniques to measure DIP (Karl & Tien, 1992), there appears to be a shift in [DIP] between oligotrophic gyres in the Northern VS. Southern Hemispheres as well as a longitudinal gradient within the gyres (Martiny et al., 2019). Drivers for differences in concentrations among the subtropical gyres are poorly understood but hypothesized to include iron stress among microbial communities (Mather et al., 2008; Moutin et al., 2008). Fourthly, [DIP] is substantially higher in the Southern Ocean compared to Arctic regions (Codispoti et al., 1991) – likely due to upwelling and iron stress (Boyd et al., 2000). Furthermore, land masses break circumglobal wind and current circulation patterns in the Arctic Ocean

leading to isolated regional DIP sources and sinks. Thus, it appears that [DIP] display clear global variation related to specific ocean physical and biological processes.

Remote sensing observations potentially related to DIP have been collected for over two decades and overlap with many field DIP measurements. While there is no known direct optical signature of DIP within the remote sensing wavelengths, multiple satellite-retrieved geophysical properties are mechanistically related to [DIP] and thus provide a potential avenue for estimating global surface DIP distributions. For example, the first axis of variation in [DIP] could possibly be captured by satellite observations of sea surface temperature (SST) and/or photosynthetically active radiation (PAR). However, we predict that the SST-nutrient relationships changes in time and space and would not capture the additional axes of variation in [DIP] leading to high global uncertainty. There are several possible satellite measurements that possibly could capture variation in [DIP] due to upwelling in low latitude regions. This could include inherent optical properties (absorption, reflectance, or backscatter) or a metric of phytoplankton biomass or productivity (Behrenfeld et al., 2008; Behrenfeld & Falkowski, 1997; Westberry et al., 2008). Alternatively, sea level anomalies and surface wind properties of wind strength, wind stress and wind-derived upwelling intensity could capture the impact of upwelling on DIP. Metrics of Fe stress or supply may enable a distinction of [DIP] between the subtropical gyres. One study has proposed using fluorescence quantum yields to describe physiological iron stress in phytoplankton (Behrenfeld et al., 2008) whereas the iron supply may be partially tied to aerosol optical thickness (Randles et al., 2017). Finally, we predict that polar differences are due to a combination of iron stress and physical strength

of upwelling and circulation. Thus, remote sensing observations along these four axes may accurately describe the global variation of surface [DIP].

Here, we aim to develop a remote sensing approach to estimate the global distribution of surface [DIP] by applying our mechanistic knowledge of DIP sources and sinks. Furthermore, we propose to use artificial neural network models to describe the complex nonlinear response and interactions between remote sensing observations and [DIP]. First, we test which combination of satellite inputs leads to the best prediction of surface [DIP]. Secondly, we describe the regional uncertainty for the best model fits. Having a new remote sensing estimate of DIP provides high spatial and temporal resolution observations of nutrient stress, which impact biological processes.

Methods

DIP Data Collection

The majority of DIP observations used in this study were from the GLODAPv2.2019 database (Olsen et al., 2016, 2019) (Figure S2.1). DIP observations in GLODAPv2.2019 were sourced from the WOCE, CLIVAR, and GO-SHIP repeat transects between 1972 and 2017. In total, there were 28,553 DIP observations from the top 10m. Following difficulties in accurately estimating DIP concentration below 1 μM, we added DIP observations from a recent high sensitivity DIP compilation (Martiny et al., 2019) (Figure S2.1). Since several cruises conducted underway sampling over several hours, samples were binned into 0.15˚ grids and by date for a total of 32,040 DIP observations. As described below, we matched each DIP observation to weekly, monthly, or monthly climatology RS inputs where possible (Figure S2.2). A total of 18025 DIP observations contained all 34 inputs and were used for the initial neural network model selection process.

Selection of Remote Sensing Inputs

Based on our knowledge of DIP sources and sinks, we narrowed down possible remote sensing inputs to four major categories (Table 2.1). In total, thirty-four RS inputs were selected and matched to DIP observations. A more detailed description of satellite data retrieval and resolution is available in supplementary information (Table S2.1). Briefly, the following inputs were downloaded from https://oceancolor.gsfc.nasa.gov/ using the SeaWiFS and MODIS L3 mapped files (a_412_giop, a_443_giop, bb_412_giop, bb_443_giop, bbp_443_giop, Rrs_412, Rrs_443, aot_869, aot_865, chl_gsm, chlor_a, par, pic, poc, Zeu_lee, sst). Three inputs were downloaded from http://www.science.oregonstate.edu/ocean.productivity/ using the CbPM model for SeaWiFS and MODIS (carbon_cbpm, growth_cbpm, and npp_cbpm). Plankton fractions were downloaded from https://doi.pangaea.de/10.1594/PANGAEA.892211 for Sfm (Mouw et al., 2019), and from https://doi.pangaea.de/10.1594/PANGAEA.859005 for pico-, nano-, and micro- fractions (Kostadinov et al., 2015). Salinity (Lee et al., 2012; Meissner et al., 2018; Wentz et al., 2014) was downloaded from the Aquarius (ftp://podaac-ftp.jpl.nasa.gov/allData/aquarius/L3/mapped/V5/7day/SCI/2015/) and SMAP satellites (ftp://ftp.remss.com/smap/SSS/V03.0/FINAL/L3/8day_running/40km/). Wind inputs (taux, tauy, upwelling, curl, and modStress) were downloaded for the QuikSCAT and METOP-ASCAT satellites (https://coastwatch.pfeg.noaa.gov/erddap/griddap/index.html?page=1&itemsPerPage=1000). Estimates of dry, wet and total dust deposition was taken from the MERRA-2 NASA model (https://disc.gsfc.nasa.gov/datasets?keywords=%22MERRA-2%22&page=1&source=Models%2FAnalyses%20MERRA-2). Lastly physiological iron

stress (phi) was provided through Toby Westberry at Oregon State University (Behrenfeld et al., 2008).

Physical/chemical properties along the first latitudinal axis:

The first axis of variation was partially linked to differences in water column stratification. We chose RS inputs to differentiate low latitude (increased salinity, temperature, and light availability) from high latitude (reduced salinity, temperature, and light availability) environmental conditions. The corresponding RS inputs were sea surface salinity (SSS), sea surface temperature (SST), and photosynthetically active radiation (PAR).

Water optical properties between the second subtropical and tropical axis

The second axis of variation was tied to differences in upwelling intensity between the subtropical gyres and equatorial regions. We expected water optical properties would reflect differences in phytoplankton productivity and nutrient drawdown between upwelling and downwelling regions at low latitudes. Only variables available as L3 data for both SeaWiFS and MODIS-Aqua were selected to improve matches to DIP observations. The content of dissolved and particulate matter within the water will change the absorption, backscattering, and reflectance of light. By choosing only shared variables as stated above, we selected the total absorption coefficients (a412, a443), total backscatter coefficients (b412, b443), and remote sensing reflectance (Rrs412, Rrs443) at 412 and 443nm wavelengths, as well as the backscatter coefficient for particles at 443nm (bbp443). Additional RS inputs derived from water optical properties from https://oceancolor.gsfc.nasa.gov included chlorophyll a (chlGSM, chlOCI), particulate inorganic carbon (PIC), particulate organic carbon (POC), and euphotic zone depth

(ZEULee). Productivity RS inputs were included from the Carbon-based Productivity Model (CbPM, https://www.science.oregonstate.edu/ocean.productivity/) for net primary production (NPPCbPM), growth rate (growthCbPm), and phytoplankton carbon biomass (carbonCbPM). Lastly, estimated of plankton size class fractions were included for micro-plankton (SfmMouw, microKosta), nano-plankton (nanoKosta), and pico-plankton (picoKosta).

Iron supply indicators between the third subtropical gyre axis

Among subtropical gyres, dissolved iron was proposed as the driver of [DIP] variation. Iron is likely sourced from aeolian dust and continental margin sediment inputs. We only associated RS inputs with dusy supply using aerosol optical thickness (aot869,865) and estimates of total dust deposition (tot_dd), total dry dust deposition (tot_ddd), and total wet dust deposition (tot_dwd) across five particle classes. Dust deposition estimates are taken from the NASA MERRA2 model, which assimilates remote sensing inputs into an atmospheric process and transport model. Beyond supply, a remote sensing metric for physiological iron stress (phi), has been derived from variation in phytoplankton fluorescence. Because this phi metric is derived from water optical properties, it is included in two categories.

Wind and upwelling indicators between the fourth polar ocean axis

The wind derived upwelling indicators are expected to be more accurate at high latitudes. These include zonal wind speed (taux), meridional wind speed (tauy), wind-driven upwelling (upwelling), the modulas of wind stress (Modstress), and wind stress curl (curl). Sea level anomaly (SLA) is also included as an upwelling indicator.

Neural network analysis

Nonlinear interactions between inputs and DIP were modelled using artificial neural networks. A network was trained with 1 to 5 combinations of RS inputs. The DIP database was randomly split 50/50 into training and validation datasets. Three nodes were used in the network with the Bayesian regularization backpropagation settings (trainbr in MATLAB). This process was repeated 100 times for each input combination. All model analyses were done using MATLAB's neural network toolbox.

Model Selection

The models were ranked according to the Akaine's Information Criterion to determine the best fitting model: AIC = n x log(SSE/n) + 2p. The goodness of fit is determined by multiplying the number of training observations (n) by the log of the sum of square error (SSE) of the training dataset divided n. As the number of parameters increases, there is a penalty expressed as 2p, where p is the number of parameters.

Regional uncertainty

We used the regional boundaries as described in Teng and colleagues for biome definitions (Teng et al., 2014). A 0.3 mmol m-3 DIP contour was used to delineate subtropical gyres. In the northern hemisphere, regions approximately south of 60°N were defined as the North Pacific Temperate and North Atlantic Temperate zones. Above 60°N is defined as the Arctic Ocean. In the Southern Hemisphere, all regions south of the 0.3 mmol m-3 DIP contour are part of the Southern Ocean.

Results

Patterns of predicted [DIP]

Predicted (DIPsat) and observed [DIP] (DIPobs) were significantly correlated (Figure 2.1) and the best model (lowest AIC score) explained 77% of the variation in surface DIP (Figure 2.2A). The best model had four inputs; i) sea surface temperature (SST), ii) net primary productivity (NPP) iii) sea surface salinity (SSS) iv) total dust deposition (tot_dd) (Figure 2.3, Figure 2.4). It captured a latitudinal gradient of high [DIPsat] at the poles, intermediate at equator, and lowest in subtropical gyres and was well within the ranges of the GLODAP latitudinal distribution (Figure 2.2A). The model successfully predicted higher [DIPsat] in the Southern Ocean and southern subtropical gyres, as compared to their northern counterparts. However, at low DIP concentrations the best fit model overestimated [DIPsat] in each subtropical gyre (Figure S2.3) and had an R^2 of 0.08 for [DIP] < 0.1 μM. Between 20°N and 20°S, our model captured the spatial extent of equatorial upwelling, but underpredicted the magnitude of elevated [DIPobs] in parts of the Indian and Pacific Oceans (Figure 2.1). Spatially, [DIPsat] agreed with the GLODAP trend of reduced [DIP] on the western side of the Atlantic and Pacific Ocean basins. Thus, our remote sensing estimation captured most regional differences in [DIPobs].

Predictive ability of Remote Sensing inputs

The combination of remote sensing (RS) inputs matched our four axes of variation in [DIP]. When we binned the models by AIC score, we observed the best models (AIC score < -19,000) included SST, inherent optical properties, iron stress/supply indicators, and SSS (Figure 2.4). To explore which inputs most closely predicted [DIPsat] along the four axes (latitudinal, equatorial upwelling, subtropical gyres, and polar oceans), we ran neural

network simulations constrained by latitude. Along axis 1, SST was notably the best predictor of latitudinal variation in [DIP] and described 50% of variation in [DIP] (Figure S2.5). However, SST predicted the lowest [DIPsat] at in areas of equatorial upwelling, demonstrating the limitation of a single remote sensing variable for predicting changes in [DIP]. Adding NPP to the SST model allowed for the distinction of low [DIP] in the subtropical gyres vs. elevated [DIP] near the equator (Figure S2.5; $R^2 = 0.34$ for latitudes 45°N to 45°S). Adding either iron indicators or salinity to the SST model generated lower [DIPsat] in the Northern Hemisphere subtropical gyres. From 15-45°N a model of total dust deposition and SST had a mean [DIPsat] ~0.7 μM versus ~1 μM from 15-45°S (Figure S2.5; $R^2 = 0.45$ for latitudes 15°N/°S to 45°N/°S). For axis 4, salinity or an inherent optical property, in combination with SST, captured Arctic geographic complexity and higher [DIPsat] in the Southern Ocean (Figure S2.5, $R^2 = 0.5$ for latitudes above 45°N/°S). Wind/upwelling indicators were only significant in the polar regions. Among the best models, the inherent optical properties and dust deposition inputs were highly correlated (Figure S2.5) and interchangeable (Figure 2.4, Figure S2.4). Thus, several satellite observation types could be substituted as long as all four axes of variation were included in the remote sensing estimate.

Interactive effects

Interactions among RS inputs suggested regional variation in regulation of DIP. The interaction between SST and [DIPsa]t was consistent across regions; higher SST predicted reduced DIPsat concentrations (Figure 2.5A). Above 20°C, the other four RS inputs gave rise to higher [DIPsat] in equatorial regions. NPP had a nonlinear effect on [DIPsat] between the high and low latitude regions (Figure 2.5B). At high latitudes, increased NPP

predicted DIPsat drawdown, but at low latitudes, high NPP indicated elevated DIPsat concentrations – presumably through an increased supply. Higher salinity indicates water stratification, and here produced depressed DIPsat values (Figure 2.5D). The exception was for equatorial conditions, where more saline water was correlated with higher [DIPsat], possibly indicating upwelling of less saline water. Iron supply indicators had a direct relationship with DIPsat concentrations (Figure 2.5C). Higher dust deposition at low latitudes generally predicted lower DIPsat concentrations. Dust deposition though had little impact in polar areas. While the sign of the NPP relationships with [DIP] was consistently negative for the Arctic and Southern Oceans, NPP had divergent [DIP] curves for low latitude Equatorial and subtropical gyre situations. The artificial neural network successfully weighted the influence of the RS inputs according to region.

Regional uncertainties

We observed a clear bias in the prediction of [DIPsat] at low latitudes. First, we overpredicted the lowest DIPsat concentrations in the subtropical gyres and our remote sensing model was unsuccessful in matching DIP observations below 0.1 μM (Figure S2.6). In subsequent runs, we reanalyzed the neural networks with a high sensitivity DIP database and found a RMSE below 0.35 approaching 0.03 μM DIP (Figure 2.2B). The mismatch between low [DIPobs] and [DIPsat] was most evident in the North Atlantic gyre where the mode of observations is between 0.01 to 0.1 μM (Figure S2.3). This range of [DIP] was where the satellite-derived RMSE increased substantially (Figure 2.2B). Second, we underpredicted the DIP concentrations across the Equatorial Pacific (Figure 2.1, Figure S2.3). The areal extent of nutrient enrichment in the Equatorial Pacific Ocean is well bounded, but the predictions are consistently negatively biased. This trend of negatively

biased [DIPsat] in upwelling regions is also observed along eastern boundary current in North America and Africa. Third, the influx of DIP into the Arabian Sea is not resolved spatially. Overall, the satellite-derived estimate improves upon prior global estimates of [DIP] but regional challenges remain.

Discussion

Here, we develop a satellite-derived estimate of the global variation in sea surface [DIP] that predicted 77% of the spatial-temporal variation measured in the field. Our estimate matches latitudinal and regional gradients across diverse biomes. Formerly, studies determined the absence/pretense of a nutrient by the regional sea surface temperature (SST) at which nutrients (nitrate, phosphate, and sulfate) become undetectable by conventional methods (Kamykowski et al., 2002; Kamykowski & Zentara, 1985; Switzer et al., 2003). Alone, SST covered nearly 58% of the variation in global [DIPobs]. However, SST alone fails to resolve differences in [DIP] between low and high productivity low-latitude regions, but can be useful in predicting [DIP] regionally (Palacios et al., 2013; Waldron & Probyn, 2010). SST has been combined with RS chlorophyll a and/or modelled mixed layer depths (MLD) to estimate [DIN] in productive regions (Arteaga et al., 2015; Gomes et al., 2000; Steinhoff et al., 2010). Like prior attempts to estimate [DIN], we employ additional water optical RS inputs to capture elevated [DIP] in warm, productive regions. While some studies have tried to estimate the supply of DIN from below by using sea surface height (SSH), sea level anomaly (SLA) , or wind stress estimates in combination with circulation models (Oschlies & Garçon, 1998; Siegel et al., 1999; Williams et al., 2000), we found no substantial increases in explanatory power from adding RS inputs linked to sea level or wind for [DIP]. To our knowledge, there has not

been a concerted effort to estimate nanomolar gradients in [DIP] via RS inputs. This satellite-derived DIP estimate is a significant advance forward for capturing DIP availability in oligotrophic biomes with the addition of iron supply indicators. While not a direct estimate of iron supply, two iron indicators were consistently in the best models, strongly supporting the importance of iron in modulating [DIP] (Mather et al., 2008; Moutin et al., 2008). Our estimate not only captures the depressed DIP observed in the Northern Hemisphere gyres, but also the east-west gradient in DIP concentrations. Neural networks provide a strong framework for using RS observations to create an open ocean DIP indicator that matches our mechanistic understanding (Wang et al., 2018).

Establishing relationships between DIP and satellite observations heavily depends on the accuracy to which we can detect changes in situ [DIP] (Martiny et al., 2019) and the ability of the neural networks to discern regional interactions among RS inputs (Wilson & Coles, 2005). The satellite-derived estimate has three major uncertainties to precisely predicting DIP at low latitudes. First, we have the poorest fits between [DIPobs] and [DIPsat] among subtropical gyres. Adding a high sensitivity database improved the fit below 0.03 μM, but not to the lowest observation near 0.01 μM. Approximating DIP stress and availability in low biomass ecosystems is difficult, in part because wide swaths of subtropical gyres are below the detection limit of common assays (Martiny et al., 2019). Multiple methods now exist to measure sub-nanomolar levels of DIP (Haberer & Brandes, 2003; Karl & Tien, 1992; Li et al., 2008; Takahashi et al., 2009), but are not routinely used on repeat hydrography sections. Secondly, our model has a systematic negative bias in equatorial and eastern boundary upwelling systems. We speculate the model is limited by the dynamic range of DIP concentrations experienced in upwelling systems and fits the

estimated [DIP] towards the mean value. If true, we anticipate similar bias temporally during a phytoplankton bloom. Third, we had mixed results in estimating [DIPsat] in the Northern Indian Ocean, where ocean circulation and productivity dramatically change with the monsoonal season (Veldhuis et al., 1997). While the Bay of Bengal experiences fresh water stratification via immense river inputs, the Arabian Sea seasonally has increased upwelling during the Southwest monsoon (Kumar et al., 2002). Our combination of RS inputs was able to predict lower DIP in the Bay of Bengal, but not higher nutrients in the Arabian Sea. Within unique and complex systems, a regional based model may better match the local ecosystem dynamics. As such, our [DIPsat] estimate is best suited to open ocean sea surface [DIP]. Contrary to our expectations, sea surface salinity and not wind driven upwelling indices separated the polar variation axis and additional subtropical gyre variation. Sources for variation in sea surface salinity depend on region, and range from evaporation-precipitation patterns, river discharge, ice melt, and ocean circulation. Depending on the source of salinity changes, the relationship with [DIP] can lead to better estimates (e.g., Arctic Ocean, seasonally stratified biomes, and among the subtropical gyres) or poor relationships in unique areas (e. g. Arabian Sea, Bay of Bengal). Low saline waters in the Arctic could either be indicators of river inputs, which are generally DIP depleted relative to nitrate, or ice melt that contains varying amounts of P sources and inhibits stratification (Pabi et al., 2008). Neural networks assign weights to the unique combination of inputs, allowing a more accurate estimation of [DIP] by region where the exact interaction between predictors is unclear.

Variation in surface [DIP] is important for many ecosystem and biogeochemical processes. The availability of DIP shapes community interactions (Tilman et al., 1982)

nutrient uptake strategies (Lomas et al., 2014), and cellular stoichiometry (Galbraith & Martiny, 2015). At the surface RS observations have impressive spatial-temporal coverage over the past two decades, while DIP observations now cover each major ocean biome. A climatological view is excellent for estimating average nutrient stress but may not reflect the *in situ* DIP stress for an active community at any given time. Future attempts to model biogeochemical processes via remote sensing, sea surface DIPsat serves an important role.

Acknowledgements

ACM was supported by grant (NSF Convergence). CAG was supported by grant XXX. We want to thank George Hagstrom (Princeton University), for helpful discussions on data transformations. We thank the many oceanographic researchers who collected the data that contributed to the GLODAPv2 project and high sensitivity DIP cruises, and acknowledge the huge effort made to gather all data to create each database.

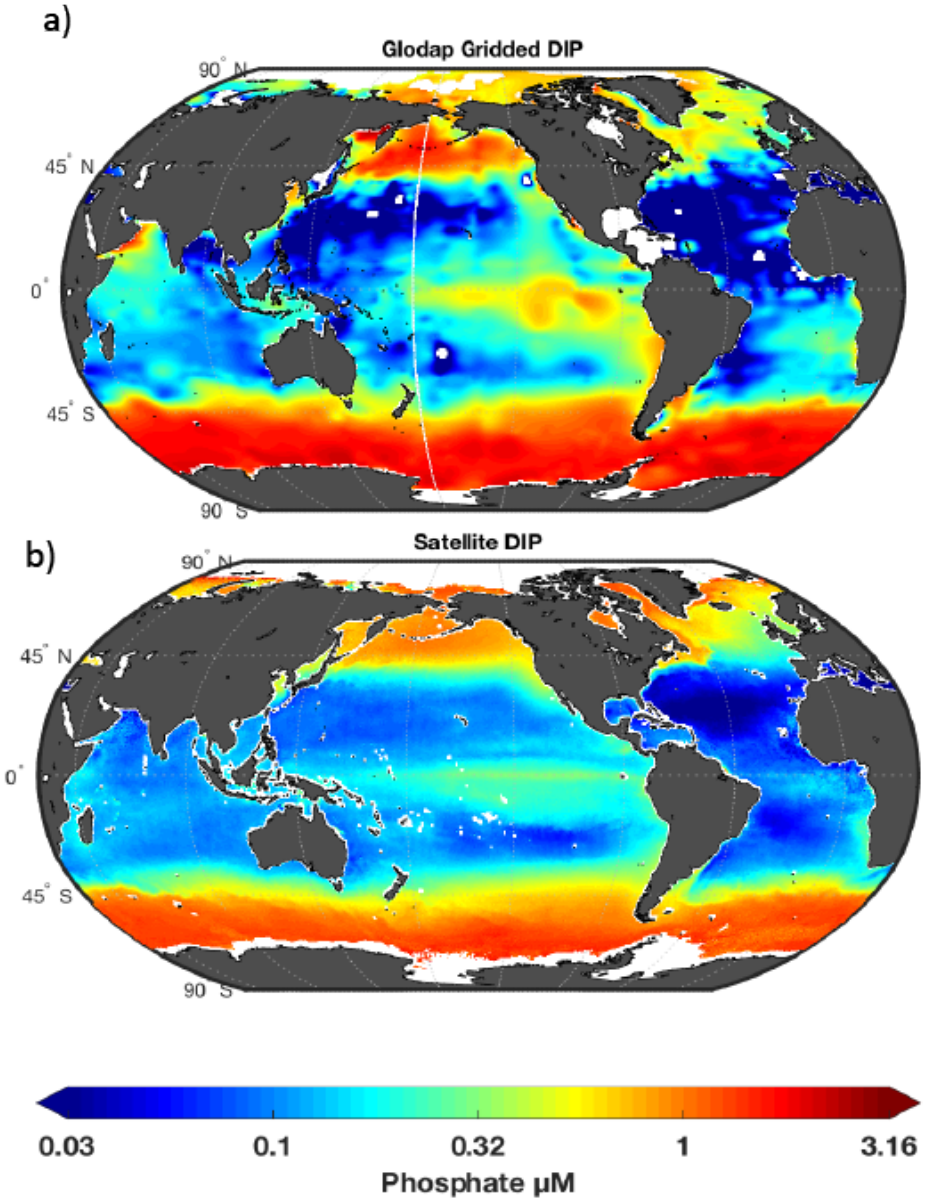

Figure 2.1: Global surface DIP distribution. Annual mean [DIP] are shown for A) GLODAPv2 observations interpolated at the surface, and B) Satellite [DIP] predicted from the best network model using annually average RS inputs at 1 degree resolution.

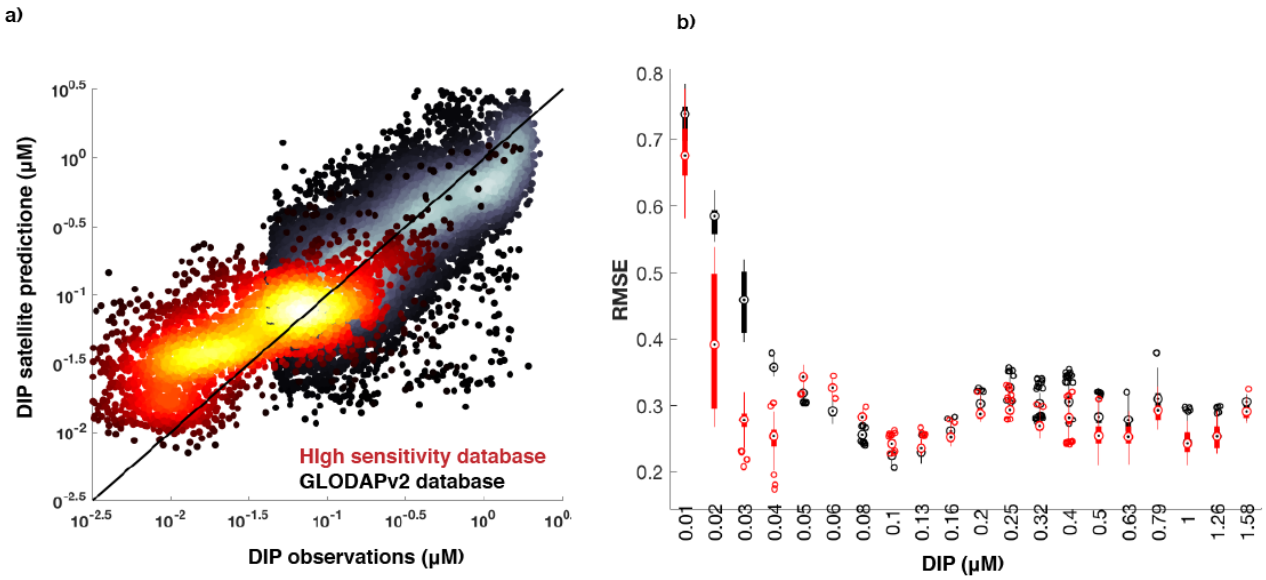

Figure 2.2. Improved model fits at low concentrations. A) Scatter plot of [DIPsat] against [DIPobs] for the high sensitivity database (red) and the GLODAPv2 database (black). B) RMSE binned by [DIP] is shown for the original network model (GLODAPv2 alone-black) and improved model (includes high sensitivity [DIP]-red).

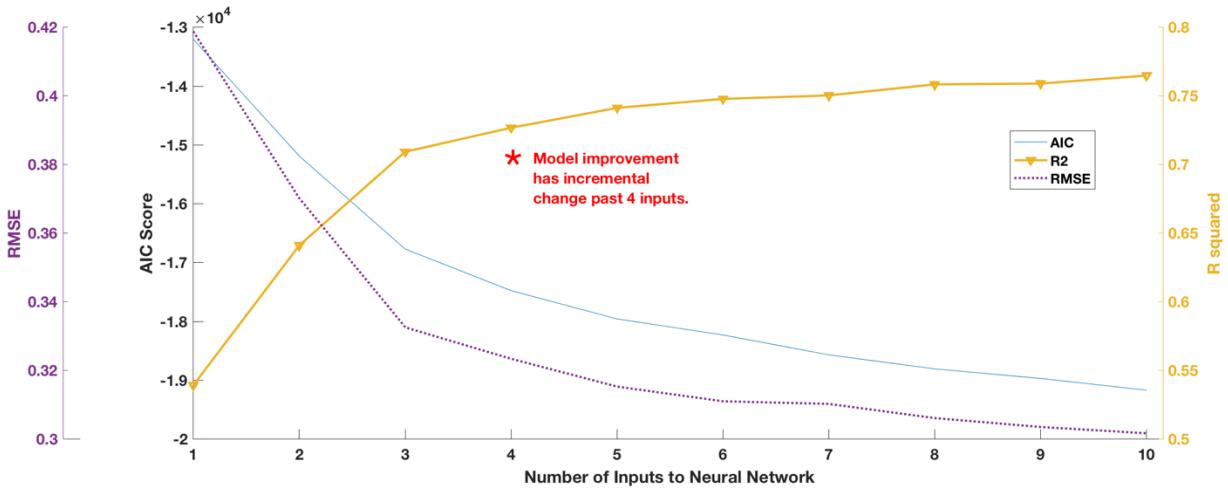

Figure 2.3: Model fits with increasing network inputs. Statistics are shown based on the best neural network model fit (lowest AIC score) with increasing input amounts. Results are shown for RMSE (dashed purple), AIC score (solid blue) and R squared (yellow triangles).

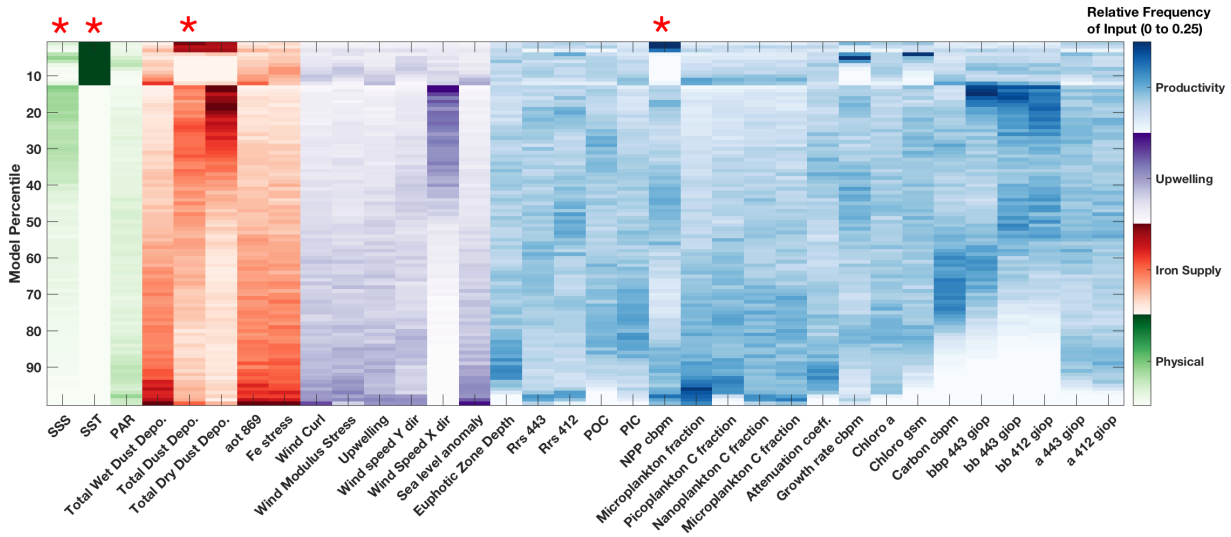

Figure 2.4. Best model RS input. All four combination models are ranked and binned into percentiles based on AIC scores. In each bin, the relative frequency scales between 0 (white) and 0.25 for the categories; productivity (blue), upwelling (purple), iron supply (red), and physical (green). A red asterisk denotes the best fitting model (SSS, SST, Total Dust Deposition, and NPP).

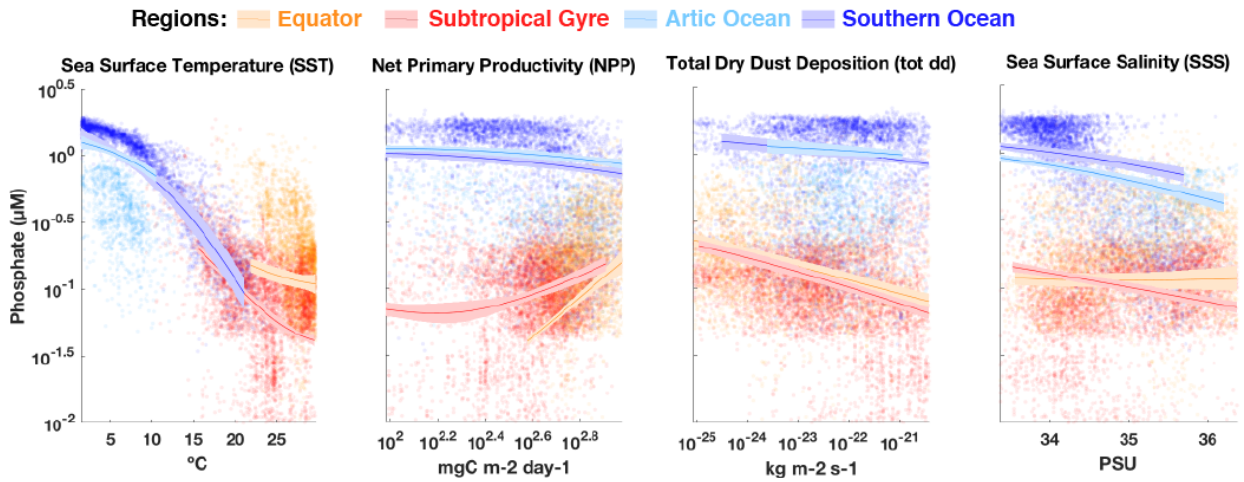

Figure 2.5. Interactions between DIPsat and remote sensing inputs. Predicted DIP is plotted as solid line, and standard error as shaded area. All but one RS inputs from best fit are held constant at mean values within defined regions (Teng et al., 2014), while values are varied for A) sea surface temperature (SST), B) net primary productivity (NPP), C) total dust deposition (tot_dd), and D) sea surface salinity (SSS). Colored scatter points are DIP observations for the equator (orange), subtropical gyres (red), Arctic (light-blue), and Southern Ocean (dark-blue).

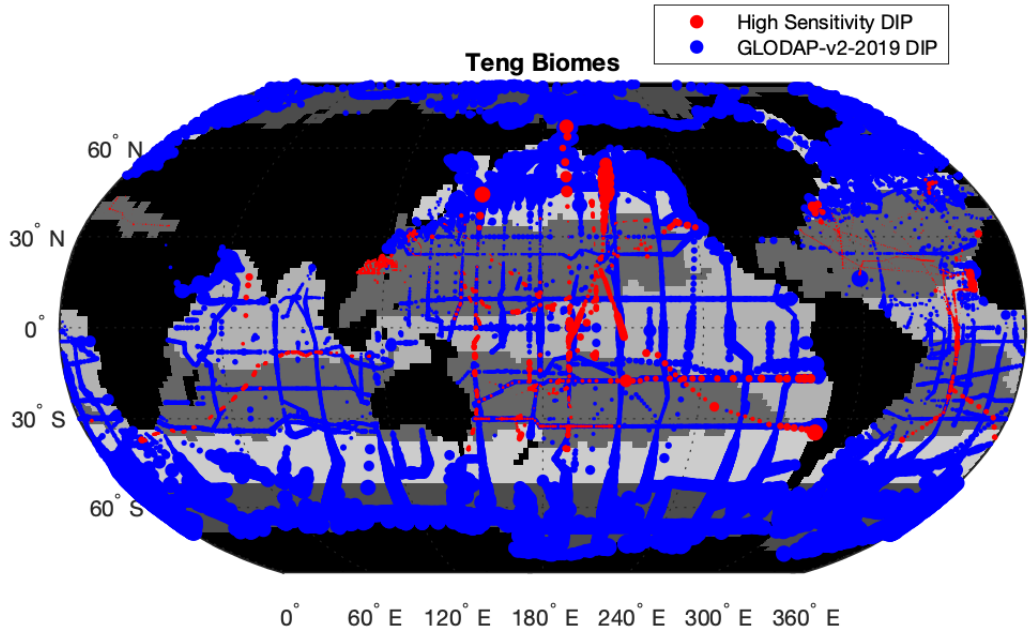

Figure S2.1 DIP observations in the top 10 m for GLODAPv2 (black) and the high sensitivity database (green). Increasing marker size indicates increasing DIP concentrations. The background shades represent the biomes defined in Teng et al. 2014. Subtropical gyres are outlined by a 0.3uM World Ocean Atlas phosphate contour (N.A gyre, N.P. gyre, S.A. gyre, S.P. gyre, and I.O. Gyre). Tropical upwelling regions between gyres are defined as Atlantic Equatorial, Pacific Equatorial, and N.I.O. monsoonal. The Arctic Ocean is defined above 65°N (excluding Labrador Sea near Greenland) and the Southern Ocean below 55°S. Finally, the N.A temperate and N.P. temperate are the leftover area in the Northern Hemisphere.

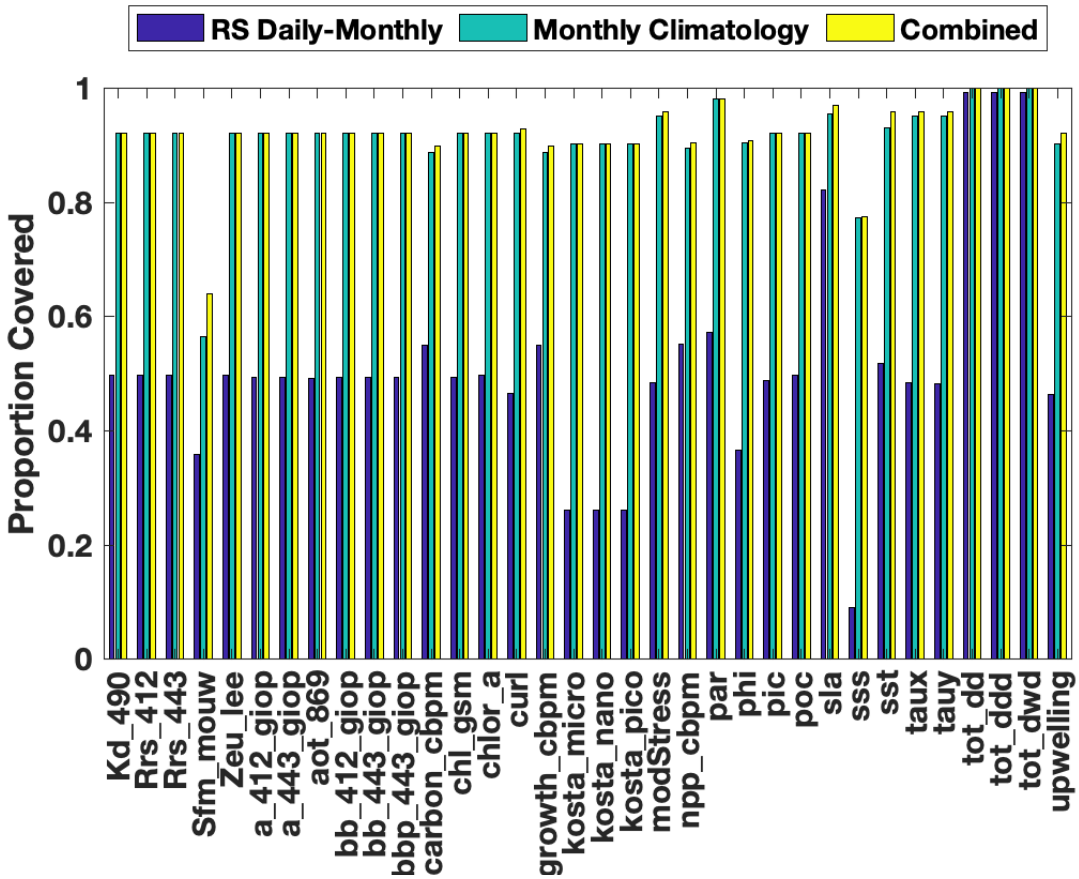

Figure S2.2. Proportions of DIP observations matched to satellite input. The proportion is based 32,040 DIP observations. The blue represents monthly-daily satellite matches, green monthly climatology, and yellow the total coverage. Remaining DIP observations had no satellite match-up for that input. Only DIP observations with all 34 inputs were used in the initial neural network analyses (n = 18025).

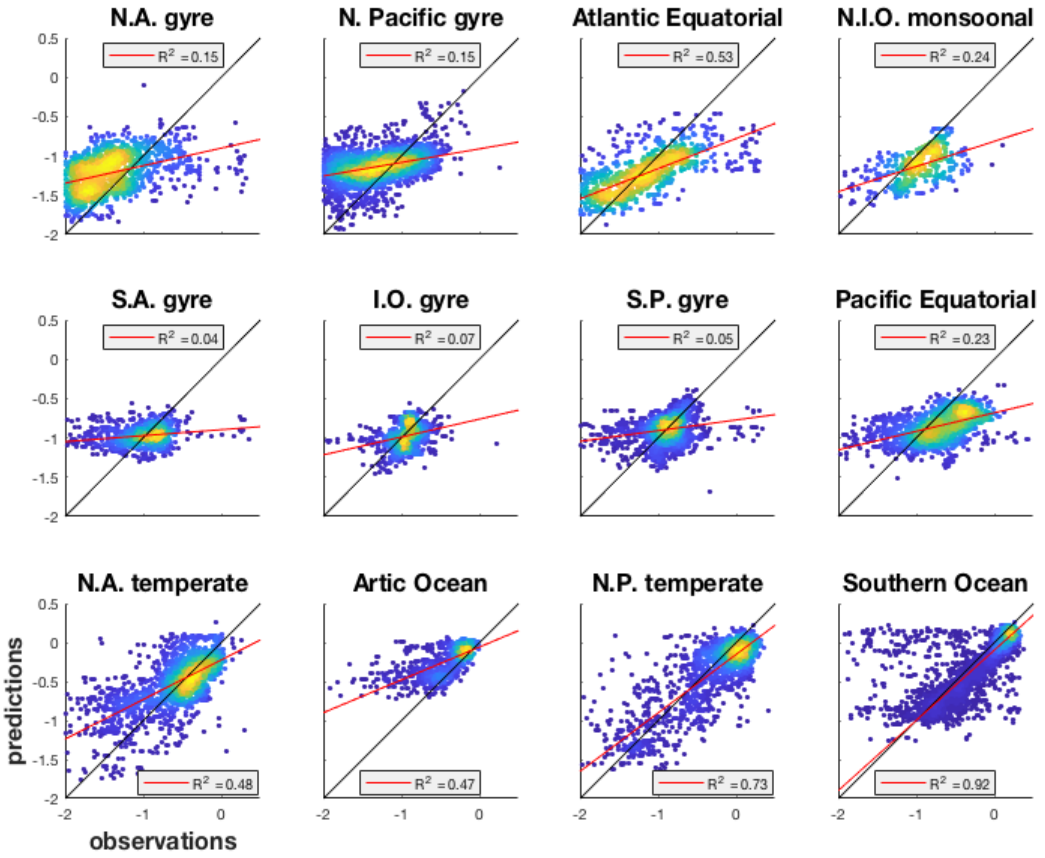

Figure S2.3. Density scatter of phosphate observations VS. predictions by region. The black line is the 1:1 line, and red line is the best fit line in MATLAB to the observations and predictions. Yellow indicated high density of points, and blue indicates low density of points. (Order of regions is based on lowest median DIP to highest). Regions defined in Figure S2.1.

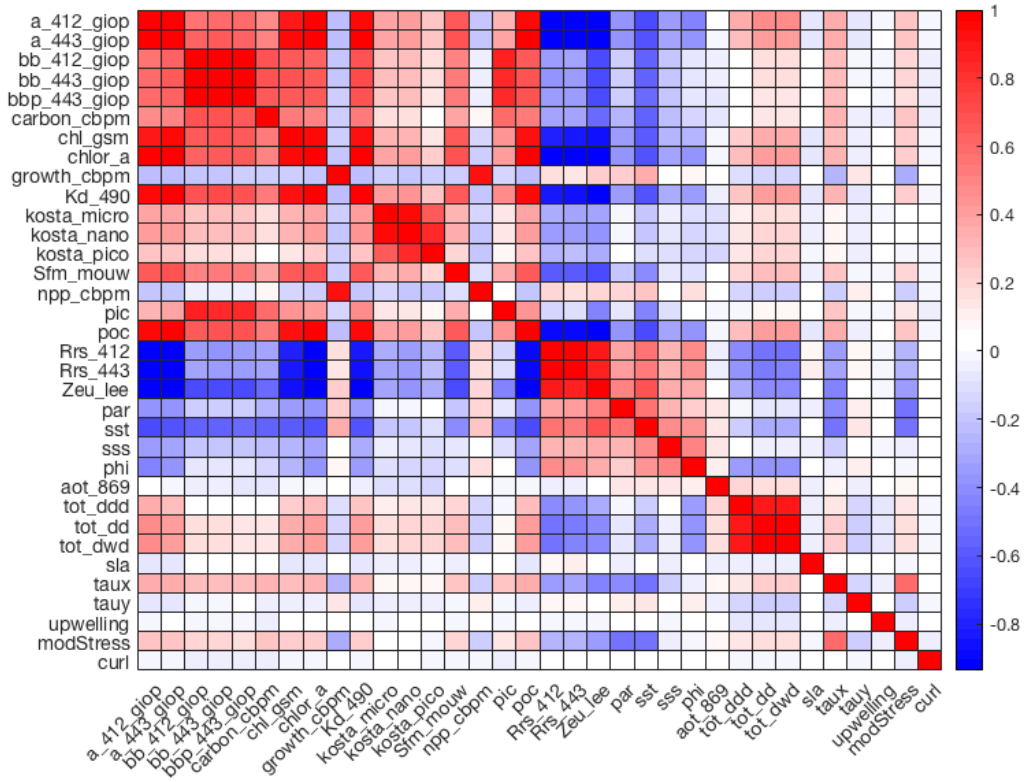

Figure S2.4. Correlation heat map of satellite observations. Colorbar indicates correlation coefficient (red positive, blue negative). Ocean optical propertied (absorbance, backscatter, reflectance), algorithms derived from (plankton size fraction, chlorophyll, productivity, carbon content, euphotic depth) , and dust deposition fractions are highly correlated among these categories. As shown in Figure 2.3, only four inputs are needed to capture 77% of variance, with additional inputs lending little increase in predictability.

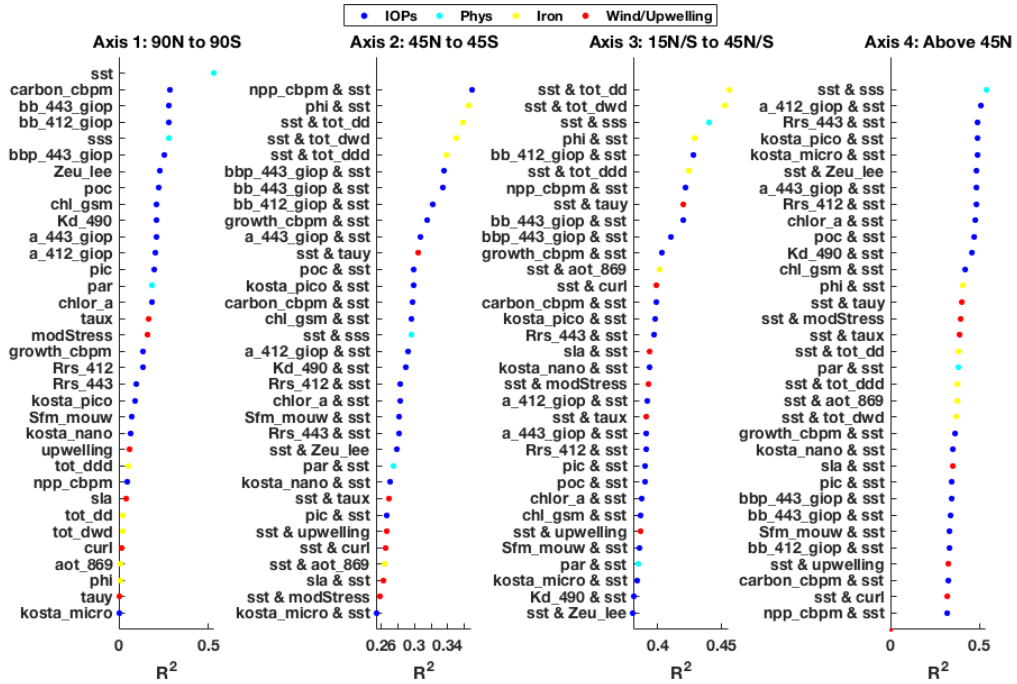

Figure S2.5. Ranking of models with 1,2 combinations along proposed axes. Models are ranked by R squared here. Axes roughly correspond to the whole latitudinal gradient (90°N to 90°S), the tropics/subtropics (45°N to 45°S), the subtropics only (15°N/S to 45°N/S), and the polar oceans (above 45°N/S). All neural network are run with a single input for the first latitudinal axis, and for up to 2 combinations of 34 RS inputs for subsequent axes. SST outperforms all other inputs for the latitudinal axis. The tropical/subtropical axis is best predicted by a combination of SST and either a productivity/IOP metric or iron supply metric. The subtropical axis is best predicted by a combination of SST and either salinity (SSS) or an iron supply metric. The final axis (polar oceans) is best defined by SST/SSS, or SST/productivity(IOP) metrics. Wind/upwelling metrics have a moderate contribution to all axes. IOP = inherent optical properties and includes related algorithm metrics (blue). Phys = physical-chemical indicators (light blue). Iron = iron supply/stress (yellow). Wind/upwelling = wind speed and sea level anomaly metrics (red).

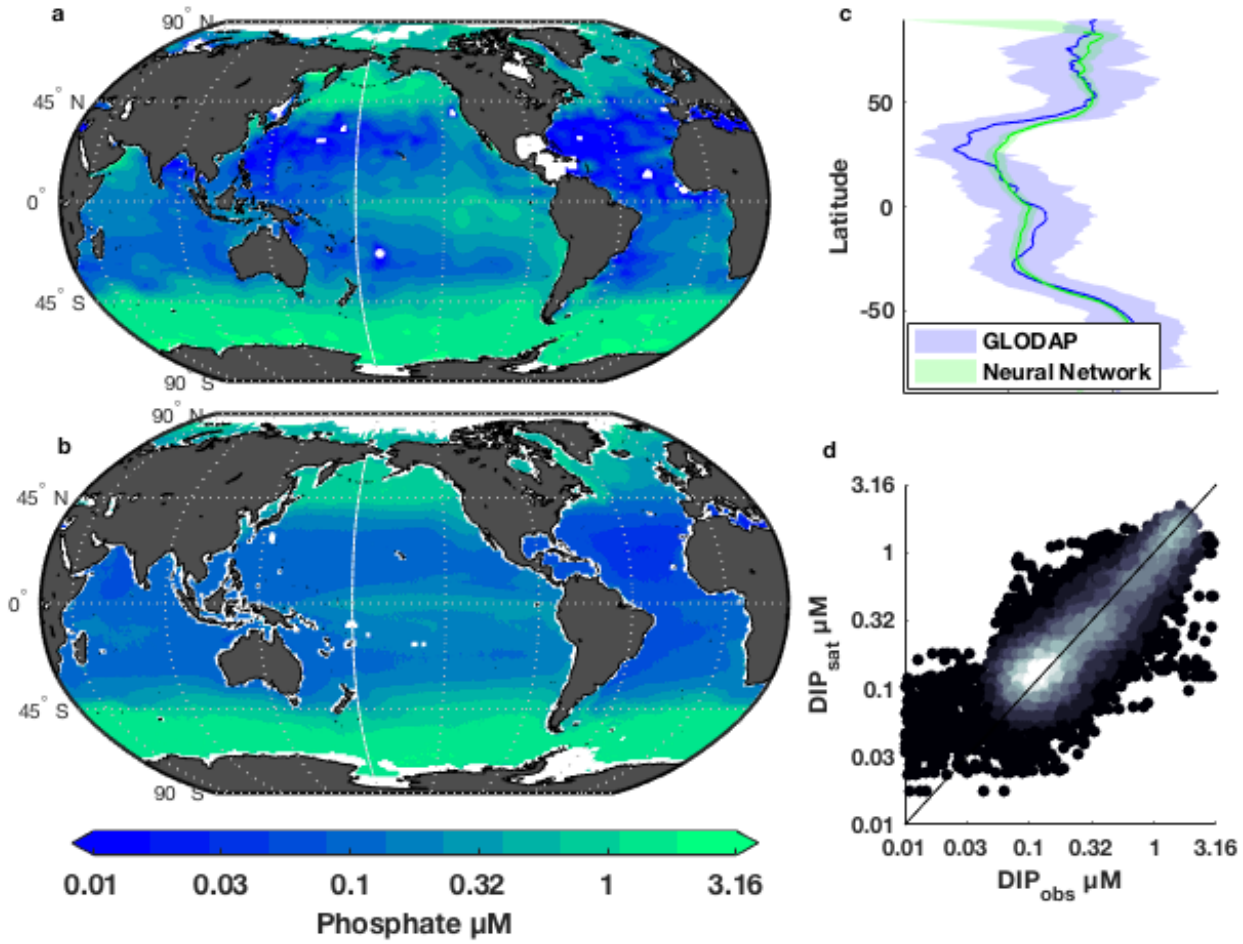

Figure S2.6. Global surface DIP distribution using GLODAPv2 database only. Annual mean DIP concentration for A) GLODAPv2 observations interpolated at the surface and B) predicted DIP from the best network model averaged for annual mean. C) The mean and standard deviation by latitude for GLODAPv2 (blue) and the best network model fit (green). D) Scatter of DIP observations and DIPsat predictions. Below 0.1µM, the model has a poor fit DIP observations, as seen in the N.A. subtropical gyre.

Table 2.1. Remote Sensing Inputs to Neural Network Model			
Axis of Variation			
1. Latitudinal	2. Tropical/Subtropical	3. Subtropical gyres	4. Polar Oceans
Associated Remote Sensing (RS) Category			
Physical-chemical environmental properties	Water optical properties and algorithms derived from optical properties	Iron supply or stress indicators	Wind-driven upwelling indicators
RS input by category			
PAR (E m-2 day-1) [a,b] SST (ºC)[a,k] SSS (PSU) [f,g]	a412 (m-1) [a,b] a443 (m-1) [a,b] b412 (m-1) [a,b] b443 (m-1) [a,b] bbp443 (m-1) [a,b] Rrs412 (sr-1) [a,b] Rrs443 (sr-1) [a,b] chlGSM (mg m-3) [a,b] chlOCI (mg m-3) [a,b] PIC (mol m-3) [a,b] POC (mol m-3) [a,b] ZEULee (m) [a,b] growthCbPM (day-1) [a,b] NPPCbPM (mgC m-2 day-1) [a,b] carbonCbPM (mg m-3) [a,b] SfmMouw [a,b,c,d] picoKosta [b] nanoKosta [b] microKosta [b] phi (%) [a,b]	aot869 [a] aot865 [b] tot_ddd (kg m-2 s-1) [j] tot_dwd (kg m-2 s-1) [j] tot_dd (kg m-2 s-1) [j] phi (%) [a,b]	SLA [e] taux (Pa) [h,i] tauy (Pa) [h,i] upwelling (m s-1) [h,i] Modstress (Pa) [h,i] curl (Pa m-1) [h,i]

Satellite sensors, exception MERRA2 linked to atmospheric circulation model
[a] MODIS-Aqua
[b] SeaWiFS
[c] MERIS
[d] VIIRS
[e] AVISO
[f] Aquarius
[g] SMAP
[h] QuikSCAT
[l] Metrop-ASCAT
[j] MERRA2 Model
[k] REMSS

Table S2.1. Description of Remote Sensing inputs to neural network models.

Varname	Description	Units	Sensors	Timespan	Resolution *Temporal, Spatial*	
a_412_giop	total absorption coefficient at 414nm	m-1	MODIS-Aqua, SeaWiFS	2002-present 1997-2010	8D, MO	0.33 deg
a_443_giop	total absorption coefficient at 443nm	m-1	MODIS-Aqua, SeaWiFS	2002-present 1997-2010	8D, MO	0.33 deg
bb_412_giop	total backscatter coefficient at 412nm	m-1	MODIS-Aqua, SeaWiFS	2002-present 1997-2010	8D, MO	0.33 deg
bb_443_giop	total backscatter coefficient at 443nm	m-1	MODIS-Aqua, SeaWiFS	2002-present 1997-2010	8D, MO	0.33 deg
bbp_443_giop	backscattering coefficient for particles at 443nm	m-1	MODIS-Aqua, SeaWiFS	2002-present 1997-2010	8D, MO	0.33 deg
Rrs_412	Remote sensing reflectance at 412nm	sr-1	MODIS-Aqua, SeaWiFS	2002-present 1997-2010	8D, MO	0.33 deg
Rrs_443	Remote sensing reflectance at 443nm	sr-1	MODIS-Aqua, SeaWiFS	2002-present 1997-2010	8D, MO	0.33 deg
aot_869	aerosol optical thickness at 869		MODIS-Aqua	2002-present	8D, MO	0.33 deg
aot_865	aerosol optical thickness at 865		SeaWiFS	1997-2010	8D, MO	0.33 deg
chl_gsm	Chlorophyll Concentration, GSM Algorithm	mg m-3	MODIS-Aqua, SeaWiFS	2002-present 1997-2010	8D, MO	0.33 deg
chlor_a	Chlorophyll Concentration, OCI Algorithm	mg m-3	MODIS-Aqua, SeaWiFS	2002-present 1997-2010	8D, MO	0.33 deg
par	Photosyntheticall y Available Radiation, R. Frouin	einstein m-2 day-1	MODIS-Aqua, SeaWiFS	2002-present 1997-2010	8D, MO	0.33 deg
pic	Calcite Concentration, Balch and Gordon	mol m-3	MODIS-Aqua, SeaWiFS	2002-present 1997-2010	8D, MO	0.33 deg
poc	Particulate Organic Carbon, D. Stramski, 2007 (443/555 version)	mol m-3	MODIS-Aqua, SeaWiFS	2002-present 1997-2010	8D, MO	0.33 deg
Zeu_lee	Euphotic depth, Lee algorithm	m	MODIS-Aqua, SeaWiFS	2002-present 1997-2010	8D, MO	0.33 deg
sst	Sea surface temperature	°C	MODIS-Aqua REMSS		8D, MO Daily	0.33 deg

growth_cbpm	growth of cells from CbPM model	day-1	MODIS-Aqua, SeaWiFS	2002-present 1997-2010	8D, MO	0.33 deg
npp_cbpm	Net primary production from CbPM	mgC m-2 day-1	MODIS-Aqua, SeaWiFS	2002-present 1997-2010	8D, MO	0.33 deg
carbon_cbpm	carbon from CbPM	mg m-3	MODIS-Aqua, SeaWiFS	2002-present 1997-2010	8D, MO	0.33 deg
Sfm_mouw	Microplankton fraction		MODIS-A, SeaWiFS, MERIS, VIIRS	1997 - 2015	MO	0.33 deg
kosta_pico	picoplankton fraction	C biomass fraction	SeaWiFS	1997-2010	MO	0.33 deg
kosta_nano	nanoplankton fraction	C biomass fraction	SeaWiFS	1997-2010	MO	0.33 deg
kosta_micro	microplankton fraction	C biomass fraction	SeaWiFS	1997-2010	MO	0.33 deg
sla	Sea level anomaly		AVISO	1993-present	MO	0.33 deg
sss	Sea surface salinity	PSU	Aquarius, SMAP	2011-2015 2015-present	7D MO	1 deg 0.25 deg
taux	Zonal wind speed	Pa	QuikSCAT, METOP-ASCAT	1999-2009 2009-present	8D	1 deg 0.25 deg
tauy	Meridional wind speed	Pa	QuikSCAT, METOP-ASCAT	1999-2009 2009-present	8D	1 deg 0.25 deg
upwelling	Upwelling intensity	m s-1	QuikSCAT, METOP-ASCAT	1999-2009 2009-present	8D	1 deg 0.25 deg
modStress	Modulus of wind stress	Pa	QuikSCAT, METOP-ASCAT	1999-2009 2009-present	8D	1 deg 0.25 deg
curl	Wind stress curl	Pa m-1	QuikSCAT, METOP-ASCAT	1999-2009 2009-present	8D	1 deg 0.25 deg
tot_ddd	Total dry dust deposition	kg m-2 s-1	MERRA2 model	1980-present	MO	0.5 deg
tot_dd	Total dust deposition	kg m-2 s-1	MERRA2 model	1980-present	MO	0.5 deg
tot_dwd	Total west dust deposition	kg m-2 s-1	MERRA2 model	1980-present	MO	0.5 deg
phi	Physiological iron stress	%	MODIS-Aqua, SeaWiFS	Climatology	MO	9 km

CHAPTER 3

Linking biome shifts in microbial genome adaptation with ocean biogeochemistry

Co-authors: George Hagstrom, Alyse Larkin, Lucas Ustick, Simon Levin, Michael Lomas, and Adam Martiny.

Abstract

Linking 'omics measurements with biogeochemical cycles is a widespread challenge in microbial community ecology. Here, we propose applying genomic adaptation as 'biosensors' for microbial investments to overcome nutrient stress. We then integrate this genomic information with a trait-based model to predict regional shifts in the elemental composition of marine plankton communities. We evaluated this approach using metagenomic and particulate organic matter samples from the Atlantic, Indian and Pacific Ocean. We find that our genome-based trait model significantly improves our prediction of particulate C: P (carbon : phosphorus) across ocean regions. Furthermore, we detect previously unrecognized ocean areas of iron, nitrogen and phosphorus stress. In many ecosystems, it can be very challenging to quantify microbial stress. Thus, a carefully calibrated genomic approach could become a widespread tool for understanding microbial responses to environmental changes and the biogeochemical outcomes.

Keywords: Metagenomics, Redfield Ratio, elemental stoichiometry

Introduction

Linking genomics and other 'omics measurements with biogeochemical cycles is a widespread challenge in microbial community ecology. Currently, most 'omics observations are used to quantify shifts in diversity and functional potential. In contrast,

we rarely use microbial 'omics data to understand and constrain large-scale energy or nutrient fluxes. This lack of convergence between microbial 'omics information and ecosystem or global models may limit our ability to predict future changes to global biogeochemical cycles.

It is well-established that the cellular and community regulation of elemental requirements and composition (i.e., carbon : nitrogen : phosphorus, C:N:P) are important for linking the global carbon and nutrient cycles (Sterner & Elser, 2002). There is an intense debate about the interaction between microbial diversity and environmental changes in regulating C:N:P for both terrestrial and aquatic environments (Moreno & Martiny, 2018; Sterner & Elser, 2002). The chemical composition of a cell is affected by many environmental factors, but nutrient availability is emerging as central (Garcia et al., 2018). Nutrient availability impacts the elemental composition of a community in multiple ways. Physiologically, the overall nutrient level impacts the growth rate (Monod, 1950). The relative supply of N vs. P (and other nutrients), relative to the algal biomass ratio, determines which nutrient availability results in cellular stress (Klausmeier et al., 2004). Furthermore, microbial lineages can have unique resource requirements and thus experience the same environment differently at a physiological level. For example, the marine cyanobacterium *Prochlorococcus* appears to have a lower P requirement compared to larger phytoplankton (Martiny et al., 2013) and co-existing diatoms can have unique N:P (Jenkins, et al., 2015). Thus, the interaction between microbial diversity and nutrient limitation plays a complex role in regulating ecosystem C:N:P.

It is a challenge to define and quantify the nutritional environment experienced by microorganisms. First, the concentrations of inorganic phosphorus and nitrogen are

commonly below detection limits in marine environments (Martiny et al., 2019). Second, most microorganisms can utilize multiple alternative forms of nutrients (Guidot et al., 2005; Shilova et al., 2017; Sosa et al., 2019; Tapia-Torres et al., 2016). Ammonium is energetically the most favored form of nitrogen. When ammonium is in low supply, microorganisms can shift in some order to urea, nitrate, or organically bound nitrogen (Herrero et al., 2001). There are several unknowns associated with the use of alternative resources. We rarely quantify the concentration and chemical form of alternative nutrients or the chemical nature organically bound N or P. Either assumptions are made about what substrate algae are using, or there are difficulties obtaining isotopically labelled compounds for more complex alternative nutrient sources. Furthermore, the resource costs associated with the use of organically bound nutrients are broadly unknown, leading to ill-defined trade-offs for nutrient assimilation. For example, cells need to invest N when upregulating acquisition proteins leading to trade-offs between nutrient investments and uptake (Bonachela et al., 2013). Finally, there is variation among individual lineages in the extent they can rely on alternative nutrient forms (Zimmerman et al., 2014). Thus, it is currently impossible to predict microbial nutrient use and associated biogeochemical roles even with a perfect chemical characterization of an environment.

Marine microorganisms show clear genomic evidence for adaptation to specific nutritional environments through gene gain and loss (Martiny et al., 2015; Morris et al., 2012; Scanlan et al., 2009). Such genomic changes reflect a shift from simple to more complex forms under limiting conditions. This pattern has been detected in many microorganisms but is clearly illustrated in marine Cyanobacteria. In regions with a replete inorganic phosphate supply, *Prochlorococcus* genomes mainly contain transporters directly

associated with inorganic phosphate (Martiny et al., 2006). However, *Prochlorococcus* adapts to lower phosphate using genes associated with regulation and the direct uptake of alternative forms. In regions with severe P stress, *Prochlorococcus* genomes contain genes for alkaline phosphate to cleave off phosphate from organic molecules (Coleman & Chisholm, 2010; Martiny et al., 2009). Here, alkaline phosphatase and a few other proteins can be highly induced to utilize organic P as an alternative P source (Antelmann et al., 2000; Martiny et al., 2006). *Prochlorococcus* adapts to N limitation in a parallel fashion, whereby cells from high N areas only contain genes for ammonium uptake (Martiny et al., 2009). In regions with stronger N stress, *Prochlorococcus* genomes sequentially include genes for urea, nitrite and ultimately nitrate assimilation. Thus, the genome content of *Prochlorococcus* (and other marine microorganisms) closely corresponds to the underlying environmental conditions and thereby describes the cellular strategies for nutrient acquisition (Berube et al., 2015).

We propose using genomic shifts among microbial communities as a 'biosensor' for *in situ* nutritional environments in order to improve predictions of C:N:P variability across ocean regions. Specifically, we combine the distribution of genes with a trait model to simulate cellular investment strategies and predict C:N:P. We show that in comparison to both traditional abiotic and common trait models, the incorporation of nutrient trait variation quantified using metagenomics greatly improves our ability to predict shifts in C:N:P. This work illustrates how we can use 'omics observations to improve our understanding of global biogeochemical cycles in ways that would be challenging to achieve with abiotic characterizations alone.

Methods

Sample collection

Seawater samples were collected from the western Atlantic Ocean (AE1319 – Aug/Sep 2013, BV46 – Oct 2011), central Pacific Ocean (NH1418 – Sept 2014), and the eastern Indian Ocean (IO9N – Mar/Apr 2016) (Figure S3.1, Table S3.1). On each cruise samples for DNA, flow cytometry, particulate organic matter, uptake rate kinetics, and nutrients were collected as described previously (Baer et al., 2017, 2018; Garcia et al., 2018; Kent et al., 2019; Lomas et al., 2014). Fifty-four stations were selected for metagenomics analysis where these corresponding measurements were taken. Select data (uptake rate kinetics, nutrient concentrations, cell abundances, and particulate elemental concentrations) for the Atlantic AE1319 and BV46 cruises is available on BCO-DMO (https://www.bco-dmo.org/project/2178) and for the Indian I09 (https://www.bco-dmo.org/project/628972). Results have previously been reported describing the cyanobacterial diversity (Kent et al., 2019; Larkin et al., 2019), cell quotas and abundances (Baer et al., 2017, 2018), uptake rate kinetics (Baer et al., 2018; Lomas et al., 2014), and particulate organic matter ratios (Garcia et al., 2018) along several transects.

Particulate organic matter

All particulate organic matter samples for carbon, nitrogen and phosphorus were collected on pre-combusted (4 hours at 500°C) GF/F filters with a nominal pore size of 0.7 μm. POP filters were rinsed with 0.17M Na_2SO_4 at time of collection to remove residual dissolved organic phosphorus. All filters were stored frozen until analysis in lab. POC/PON samples were measured using a Flash 1112 EA elemental analyzer (Thermo Scientific, Waltham, MA, USA) for the I09 transect against an Atropine ($C_{17}H_{23}NO_3$) standard curve

(range 0.2-1.5 mg). For the NH1418, AE1319, and BV46 transects POC/PON samples were measured on either Control Equipment 240-XA or 440-XA elemental analyzer using acetanilide as a standard (Steinberg et al., 2001). POP samples were analyzed using an ash/hydrolysis colorimetric method described previously (Lomas et al., 2010). Briefly, 2 mL of 0.017M $MgSO_4$ was added to the filter and KH_2PO_4 standards in acid-washed scintillation vials and dried overnight at 90°C. The filters were exposed to high temperatures 500°C for 2 hours and acidified in 0.2M HCL at 90°C. After a mixed reagent was added, the samples were analyzed on a spectrophotometer at 885nm.

Uptake rate kinetics

On the Atlantic (AE1319, BV46) and Pacific (NH1418) Ocean transects, phosphate uptake rate kinetics were taken for whole community and taxa-specific groups (e.g. *Synechococcus* & *Prochlorococcus*) using methods previously described (Michael W Lomas et al., 2014). Incubations were performed using 10 mL seawater aliquots within 3°C of ambient temperature during time of collection (~23°C). Kinetics experiments for phosphate were performed with increasing DIP additions up to 100nM, and ended at a final concentration of 100uM. On the Indian Ocean GO-SHIP transect (I09N), whole community bottle incubations were performed for uptake of ^{15}N-labeled ammonia, urea, and nitrate (Baer et al., 2018). The incubations were performed in 2L polycarbonate bottles over a 6-hr period at ambient seawater temperature. N incubations were mixed to a final concentration of 0.03μM, which is below the detection limit and reflective of the N-limiting conditions throughout the I09N transect.

Cell abundances using flow cytometry

Samples for flow cytometry and cell sorting were collected previously and are presented elsewhere (Baer et al., 2017, 2018; Kent et al., 2019). Briefly, the samples were sorted using a FACSJazz or Influx flow cytometer (BD, Franklin Lakes, NJ, USA). Samples were preserved using a 0.5% paraformaldehyde solution (final concentration), kept in the dark for 1 hour to fix at 5°C, and then stored frozen at -80°C until analysis. Populations of *Synechococcus* were determined with a gate in orange (585nm), *Prochlorococcus* based on forward scatter and red fluorescence.

Nutrients

For the NH1418, AE1319, and BV46 cruises, phosphate was measured using the MAGIC-SRP high sensitivity method (Karl & Tien, 1992). Nitrate was measured as using a cadmium reduction assay as previously described (Kent et al., 2019).

Nutrients data for the I09N cruise were provided by Jim Swift/SIO and Susan Becker/SIO and is available at https://cchdo.ucsd.edu45.

Metagenomics – library and sequencing

For DNA, 4-10 L seawater samples were collected with a 0.22 µm Sterivex filter and preserved with Lysis Buffer (50 mM Tris -HCl pH 7.6, 20 mM EDTA pH 8.0, 400 mM NaCl, 0.75 M sucrose) and frozen at -80˚C until further processing. DNA was extracted as described previously (Boström et al., 2004; Kent et al., 2019; Larkin & Martiny, 2017) and diluted (Atlantic/Pacific: 0.5ng/µl, Indian: 1ng/µl) for sequencing. Metagenomic libraries were prepared using Nextera Library Prep Kit (Illumina, San Diego, CA) with a modified PCR mixture. 1 ul was 0.5-1ng of DNA was tagmented using the Nextera DNA Prep Kit tagmentation enzyme and incubated for 10 minutes at 55°C. The Nextera XT barcodes were

annealed to metagenome fragments using the following PCR protocol. For PCR, we used 20ul of a master mix containing 0.5 µL Phusion High Fidelity buffer (New England Biolabs, Ipswich, MA), 0.5 µL dNTPs (New England Biolabs, Ipswich, MA), 0.25 µL Phusion High Fidelity polymerase (New England Biolabs, Ipswich, MA), and 14.25 µL of PCR water. Equimolar samples were pooled and the quality was checked and quantified using a Bioanalyzer (Agilent, Santa Clara, CA). The pooled library was sequenced on an HiSeq - 4000 (Illumina, San Diego, CA) producing paired end reads (2 x 150 bp). Low quality reads and adapters were removed using trimmomatic 0.35 (Bolger et al., 2014) with a sliding window of 4:15 and minimum length set to 36. PhiX was filtered out using BBduk2 tool BBMap (BBMap - Bushnell B. - sourceforge.net/projects/bbmap/, k = 31, hdist = 1). Sequences were aligned and mapped to a curated reference database (Table S3.4) using Bowtie2 (Langmead & Salzberg, 2012) with the following settings; --local -D 15 -R 2 -L 15 -N 1 --gbar 1 --mp 3. High quality contigs were assembled and processed with Anvi'o (Eren et al., 2015). Pangenome gene clusters were identified using the DIAMOND algorithm (Buchfink et al., 2014) and summarized in Anvi'o.

Nutrient assimilation gene frequencies

Prochlorococcus and *Synechococcus* genes associated with assimilation for iron, nitrogen, and phosphorus were identified based on prior studies (Berube et al., 2015; Malmstrom et al., 2013; Martiny et al., 2009; Martiny et al., 2009; Robidart et al., 2019; Scanlan et al., 2009). Based on these past studies, we filtered out genes if present in all *Synechococcus* and *Prochlorococcus* to detect variation in lineage coverage. We found the relative gene f by scaling to the median coverage of single copy core genes (SCCG) (Martiny

et al., 2019) across 54 stations. We identified the relative gene frequency for each nutrient per station, and per taxa (*Synechococcus* and *Prochlorococcus*) as follows:

$$relative\ gene\ frequency_{gene\ in\ taxa} = \sum_{\substack{genomes \\ in\ taxa}} \left[\left(\frac{gene\ coverage_{gene}}{median\ coverage\ of\ SCCG_{taxa}} \right) \left(\frac{total\ reads_{genome}}{total\ reads_{taxa}} \right) \right]$$

Next, we conducted three separate Principle Component Analysis (PCA) for N, P, and Fe assimilation genes, respectively (Figure S3.4). Each relative gene frequency was scaled between 0 and 1 across the 54 stations as inputs to the PCA (*n* x *m* matrix of *n* stations and *m* normalized gene frequencies). A total of four gene indices were produced for each station, where N/P gene = first component of PCA;

$$N_{\text{gene } Prochlorococcus}$$

$$P_{\text{gene } Synechococcus}$$

$$N_{\text{gene } Prochlorococcus}$$

$$P_{\text{gene } Synechococcus}$$

These N and P gene indices for *Prochlorococcus* and *Synechococcus* were subsequently incorporated into a trait model to predict C:P.

ATOM-gene Model

We developed a new version of the ATOM model (Moreno et al., 2018) where we incorporated gene frequencies to constrain resource allocations to nutrient stress. The ATOM-gene model describes phytoplankton in terms of their radius r, and relative allocation of biomass to biosynthesis (E), photosynthetic proteins (L), and periplasmic

proteins associated with nutrient uptake (A). ATOM-gene also represents a nutrient storage pool. Phytoplankton traits determine stoichiometry according to:

$$(\mathrm{P{:}C}) = \frac{E\mathrm{P}_E + \gamma \mathrm{P}_\gamma + \mathrm{P}_{\mathrm{stor}}}{E\mathrm{C}_P + L\mathrm{C}_P + \gamma \mathrm{C}_\gamma + \frac{\alpha(\mathrm{C}_M + A\mathrm{C}_P)}{2r}}.$$

ATOM-gene calculates phytoplankton traits using an optimality model. For each set of traits, ATOM-gene determines a functional response to environmental conditions defined by irradiance (I), temperature (T), nitrogen (N), and phosphorus (P) (Table S3.2). Instead of using *in-situ* measurements of inorganic nutrients to determine the investment to nutrient uptake, here we instead predict uptake capabilities using the gene indices for nitrogen and phosphate uptake genes in *Prochlorococcus and Synechococcus,* respectively.

$$\log[\mathrm{N}_{\mathrm{model}}] = \log[\mathrm{N}_0] - c_{\mathrm{N}}\mathrm{N}_{\mathrm{gene}}, \quad \log[\mathrm{P}_{\mathrm{model}}] = \log[\mathrm{P}_0] - c_{\mathrm{P}}\mathrm{P}_{\mathrm{gene}}.$$

Environmental conditions translate into rates of biosynthesis μ_E, photosynthesis μ_L, nitrogen uptake μ_{N}, and phosphorus uptake μ_{P}, with overall growth rate determined by the slowest of these processes:

$$\mu = \min(\mu_E, \mu_L, \mu_{\mathrm{N}}, \mu_{\mathrm{P}}).$$

The biosynthesis rate depends linearly on the investment E:

$$\mu_E = k_S(T)E,$$

where the biosynthetic efficiency decreases with temperature with a $Q_{10k} = 2$. The photosynthesis functional response comes from (Geider et al., 1996) (also see Moreno et. al.):

$$\mu_L = \frac{f(I,T)L}{1 + \phi_S},$$

where we allow the photosynthesis rate to have a non-trivial temperature dependence. We assume diffusion-limited growth to derive the nitrogen and phosphorus dependent growth rates:

$$\mu_{\mathrm{N}} = \frac{4\pi D_{\mathrm{N}}[\mathrm{N}_{\mathrm{model}}]r}{Q_{\mathrm{N}}}, \qquad \mu_{\mathrm{P}} = \frac{4\pi D_{\mathrm{P}}[\mathrm{P}_{\mathrm{model}}]rA}{Q_{\mathrm{P}}}.$$

Here $A_{min} < A < 1$, and the diffusion coefficients $(D_{\mathrm{N}}, D_{\mathrm{P}})$ decrease with temperature using $Q_{10D} = 1.5$. ATOM-gene then finds the trait combination with the largest μ. At the optimal solution either:

$$\mu_E = \mu_L = \mu_N < \mu_P \quad \text{(N-limitation)},$$

$$\mu_E = \mu_L = \mu_P < \mu_N \quad \text{(P-limitation)},$$

$$\mu_E = \mu_L = \mu_P = \mu_N \quad \text{(Co-limitation)}.$$

ATOM-gene subsequently determines C:P from this optimal strategy. If the strategy is N-limited, then:

$$\mathrm{P}_{\mathrm{stor}} = C_{\mathrm{stor}}[\mathrm{P}_{\mathrm{model}}] \max(0, \mu_c - \mu\_\mathrm{opt}),$$

where μ_C is a growth rate cutoff above which luxury storage stops.

We selected a prior probability distribution over model parameters and implemented ATOM-Gene within the STAN probabilistic programming language (Carpenter et al., 2017). We integrated C:P, N and P gene indices, temperature, and irradiance (averaged over the top 50 meters), and calculated the posterior probability distribution over model parameters assuming a log-normal probability distribution for C:P:

$$(\mathrm{C{:}P})_{\mathrm{obs}} \sim \mathrm{lognormal}\left((\mathrm{C{:}P})_{\text{Atom-gene}}\left(I, T, \mathrm{N}_{\mathrm{gene}}, \mathrm{P}_{\mathrm{gene}}, \sigma\right)\right).$$

We performed this Bayesian optimization for the gene indices computed from both *Prochlorococcus* and *Synechococcus* leading to a statistical model of C:P.

Galbraith-Martiny and P-Regression Model

The Galbraith-Martiny model (Galbraith & Martiny, 2015) calculates P:C as a linear function of phosphate concentration:

$$(\mathrm{P{:}C})_{\mathrm{GM}} = 6.9x10^{3}[\mathrm{P_{obs}}] + 6.0x10^{-3}.$$

We also created a P-regression based model (Preg) by refitting the Galbraith-Martiny GM model just to the dataset gathered here, assuming a lognormal error model:

$$(\mathrm{P{:}C})_{\mathrm{Preg}} \sim \mathrm{lognormal}\big(\kappa[\mathrm{P_{obs}}] + [\mathrm{P_0}], \sigma\big).$$

Yvon-Durocher Model and T-Regression Model

The Yvon-Durocher model (Yvon-Durocher et al., 2015) expresses phytoplankton C:P as an exponential function of temperature:

$$\log(\mathrm{C{:}P})_{\mathrm{YD}} = \Pi(T - 15) + b,$$

where $\Pi = 0.037^{o}\mathrm{C}^{-1}$ and $b = 5.010$. We also created a T-Regression based model by refitting the Yvon-Durocher model to the data-set gathered here, assuming lognormal errors:

$$(\mathrm{C{:}P})_{\mathrm{Treg}} \sim \mathrm{lognormal}(\Pi(T - 15) + b, \sigma).$$

Moreno-Hagstrom Model

The Moreno-Hagstrom model (Moreno et al., 2018) uses the radius (r) and allocation of biomass to biosynthesis (E) and photosynthesis (L) to model C:P, by calculating the trait-combination that leads to maximal growth for each combination of irradiance (I), temperature (T), and phosphorus (P). The Moreno-Hagstrom model models luxury-P storage as a linear function of P, so that:

$$(\mathrm{C{:}P})_{\mathrm{MH}} = \frac{1}{\left((\mathrm{C{:}P})_{\mathrm{structure}} + f_{\mathrm{storage}}[\mathrm{P_{obs}}]\right)}.$$

It should be noted the relationship between polyphosphate storage and ambient P concentrations has been demonstrated to have an inverse relationship in subtropical North Atlantic *Synechococcus* (Martin et al., 2014), but the direction appears to be regional dependent (Li & Dittrich, 2019).

Results

We quantified the variation in the Carbon-to-Phosphorus (C:P) elemental stoichiometry across ocean environmental gradients in the Atlantic, Indian and Pacific Ocean (Figure 3.1). Generally, C:P ratios decreased with colder water and higher nutrient concentrations. This pattern was present in the temperate region in the North Atlantic (Figure3. 1A) and equatorial upwelling in the Pacific Ocean. (Figure 3.1B). However, in the Indian Ocean C:P decreased toward lower phosphate concentrations and warmer water (Figure 3.1C) and thus showed the opposite relationship to temperature (Garcia et al., 2018). Statistical models based solely on phosphate (G-M) or temperature (Y-D) were unable to capture the different trends in the Indian Ocean and showed significant biases

(Figure 3.2). All models overestimated C:P in large parts of the Indian Ocean and either over- or underestimated C:P in the equatorial Pacific Ocean. This bias remained when we refit the G-M and Y-D models to only observations in this study, suggesting a structural bias. We next tested the more complex trait-based model but this model had strong bias, too. Thus, existing models driven by common abiotic factors were unable to predict shifts in the elemental stoichiometry of marine communities.

The incorporation of genomically-derived resource acquisition traits into a model greatly improved the prediction of regional shifts in elemental stoichiometry (Figure 3.2, R^2 = 0.45). We derived resource acquisition traits in *Prochlorococcus* and *Synechococcus* (the two most abundant phytoplankton in these samples)(Baer et al., 2018) from metagenomes. We then used the presence of nitrogen and phosphorus acquisition genes to develop an index for the induction of nutrient acquisition machinery for each nutrient and lineage (Figure S3.4). This index assumes Cyanobacterial lineages adapt to their environment through genome streamlining and the presence/absence of nutrient acquisition genes is directly related to nutrient stress. We found that shifts in adaptation and investment strategies for nutrient uptake led to lower bias in all the regions. For example, this was the only model that captured the latitudinal gradient in C:P in the Indian Ocean. Thus, the ATOM-gene model was able to incorporate a previously unknown pattern of nutrient gene frequencies to predict the regional shifts in C:P.

The frequency of nutrient acquisition genes helped resolve variation in nutrient stress at very low nutrient concentrations. We observed a significant correlation between shifts in nutrient acquisition gene frequencies and the ambient nutrient concentration (Figure 3.3). This was seen for both phosphorus and nitrogen acquisition genes and their

respective inorganic nutrient concentrations. However, the ambient nutrient concentration of phosphorus and especially nitrogen was below detection limit in many samples. Here we detected large variations in gene frequencies suggesting corresponding shifts in nutrient stress. Thus, metagenomic analyses across diverse ocean regions provided a high-sensitivity quantification of nutrient stress.

The frequency of *Prochlorococcus* acquisition genes suggested regional shifts in nutrient stress by both a single and multiple nutrients. As seen in earlier studies, we detected a high frequency of P acquisition genes for *Prochlorococcus* in the subtropical North Atlantic Ocean below 39˚N, where phosphate concentrations were low (Figure 3.4A). This included genes responsible for the regulation and uptake of dissolved organic P, arsenate detoxification, and several of unknown function. We also saw elevated P acquisition genes for *Prochlorococcus* in the north Indian Ocean and Bay of Bengal (between 1˚ and 17˚N). In contrast, P acquisition genes were low in all samples from the Pacific Ocean and south Indian Ocean. *Prochlorococcus* N acquisition genes showed a different biogeographical pattern. Urea acquisition genes were frequent in all samples with the exception of the high nitrate areas in the equatorial Pacific Ocean and temperate waters in the North Atlantic Ocean. Nitrite and nitrate acquisition genes were frequent throughout the Indian Ocean (with the exception of samples on the equator) and in the northern part of the Pacific Ocean transect. However, nitrite and nitrate genes were less common in the North Atlantic subtropical waters. Iron acquisition genes were common in equatorial Pacific Ocean. Thus, we detected multiple regions of N, P, and Fe stress through the frequency of nutrient acquisition genes in *Prochlorococcus*.

We observed a partial correspondence between the frequency of nutrient acquisition genes in *Prochlorococcus* and *Synechococcus* suggesting some lineage-specific adaptations to the nutritional condition (Figure 3.4A). Overall, the regional shifts in *Prochlorococcus* and *Synechococcus* genome content were significantly correlated (Mantel test R = 0.65, *p*-value < 0.001). In *Synechococcus*, there was also a high frequency of P acquisition genes in the subtropical North Atlantic Ocean and north Indian Ocean (Figure 3.4C). However, it appeared that the Indian Ocean area with high P acquisition genes spread further south in *Synechococcus* compared to *Prochlorococcus*. N acquisition genes were also frequent in nearly all samples for *Synechococcus,* whereas the genes were more geographically restricted in *Prochlorococcus*. There was some evidence of increase in *Synechococcus* iron acquisition genes in the equatorial Pacific Ocean but the pattern was not strong. Thus, the biogeographical shifts in nutrient acquisition genes were more pronounced for *Prochlorococcus* compared to *Synechococcus*.

The variation in nutrient acquisition genes may be linked to shifts in limitation by one or more nutrients (Figure 3.4B and D, Figure S3.4). The frequency of nutrient acquisition genes suggested P stress but also some N co-stress in the western North Atlantic Ocean and north Indian Ocean. The North Pacific Ocean and south Indian Ocean appeared to be N stressed. The equatorial Pacific Ocean was iron stressed. However, the gene frequencies suggested that a brief transition region around 10˚N in the North Pacific Ocean experienced co-stress by N and Fe. *Synechococcus* appeared to be stressed by N in temperate North Atlantic Ocean waters whereas *Prochlorococcus* appeared more stressed by iron. Similarly, *Synechococcus* showed evidence of P stress in parts of the south Indian Ocean but this was not seen in *Prochlorococcus*. Shifts in the relative gene frequency

corresponded to shifts in clade ecotypes (Figure S3.2). Thus, metagenomic analyses of phytoplankton populations suggested regional shifts in stress by one or multiple nutrients.

We used additional ecosystem measurements to verify the predictions from ATOM-gene and the overall resource investment strategies. In the Indian Ocean, uptake kinetics for the ATOM-Gene model were positively correlated with observed specific uptake rates for nitrate, ammonium, and urea (Figure 3.5). The implied nutrient distributions matched our observations of increasing N northwards and vice versa for P into the subtropical Indian Ocean gyre. Increases in N and P uptake rates, cellular investment in photosynthesis and biosynthesis, and cell volume corresponded to reduced nitrogen limitation (Table S3.3). Phosphorus limitation appeared to have little impact on C:P and cellular uptake traits in the Indian Ocean, unlike the other two basins (Figure S3.5). This was true for both *Synechococcus* and *Prochlorococcus* ATOM-Gene parameters. Although P investment increased into the subtropical Indian Ocean gyre, there was little influence on P luxury uptake and storage. Only larger cells in the temperate North Atlantic exhibited P storage in the ATOM-Gene model. Overall, co-limitation or N-limitation reduced luxury P storage in the surface Indian Ocean despite high P investment. Thus, the interaction between N and P limitation as seen in the genomic observations could be the underlying mechanism leading to latitudinal shifts in C:P observations.

Discussion

Linking ‘omics with global biogeochemistry is a major research challenge and opportunity (Caputi et al., 2019; Coles et al., 2017; Hennon & Dyhrman, 2019; Mock et al., 2016). A great deal of molecular data is being generated (Sunagawa et al., 2015; Venter et al., 2004), but there is a limited current application of this new knowledge towards

understanding large-scale changes in the Earth system (Moran, 2015). Trait-based approaches are attractive for scaling from an individual organism to key ecosystem functions by using a model intermediate (Kiørboe et al., 2018; Talmy et al., 2013). We here use this approach as an intermediate for linking genomic information with ocean biogeochemical processes. By quantifying the spatial variation due to difference in nutrient assimilation genes, we better reproduced observations of C:P in three ocean basins (Figure 3.1, Figure 3.2). The ATOM-gene model allowed for multiple nutrient indexes (N and P) where *in situ* nutrient observations were undetectable, resulting in significant improvement to the existing trait model (Moreno et al., 2018). Importantly, the gene index quantifies cyanobacterial adaptation to nutrient stressors where our knowledge is limiting. Nutrient stress may occur through diffusive limitation of ambient concentrations, the magnitude of nutrient fluxes, the ratio of nutrient supply, or nutrient co-limitation. Additionally, both *Synechococcus* and *Prochlorococcus* can utilize different P and N sources (Moore et al., 2002). This method is favorable within the relatively stable environments inhabited by *Synechococcus* and *Prochlorococcus*, which selects for genome streamlining. Thus, genome shifts integrate these unknowns through the selective pressure to retain particular genes in nutrient-poor biomes.

The frequency of nutrient assimilation genes greatly improved our understanding of nutrient stress and elemental stoichiometry of marine communities. In particular, the results showed surprising patterns of P and N limitation in the less studied Indian Ocean. Our results support a recent analysis *Synechococcus* and *Prochlorococcus* elemental quotas, leading to a gradient of N, P, and Fe stress in the Indian Ocean (Twining et al., 2019). The Bay of Bengal showed evidence of P limitation but lower N:P and C:P ratios. We attribute

this contradictory observation to an interaction between N and P stress as the upregulation of P uptake proteins is restricted by N stress (Bonachela et al., 2011). Culture studies have shown that N and P stress interact in controlling the overall cellular physiology and C:N:P (Klausmeier et al., 2004). However, it has been a challenge to translate these findings to field communities. Some of this confusion originates from external N and possibly P sources from atmospheric deposition, as well as N-fixation, which can be episodic and difficult to quantify. This leads to a poorly constrained N:P supply ratio. It is unclear why we see evidence of increased P stress near the Bay of Bengal, but it is tempting to attribute it to elevated N-fixation and P drawdown (Martiny et al., 2019; Wang et al., 2019). We also saw a high presence of Fe limitation genes in regions with low C:P, where *Synechococcus* and *Prochlorococcus* cell abundances remained elevated (Kent et al., 2019). As expected, this was seen for the equatorial Pacific HNLC region (Coale et al., 1996). Our data also support past studies indicating that the subtropical North Atlantic Ocean (Rijkenberg et al., 2014) and the southern Indian Ocean (Twining et al., 2019) could experience some iron stress. Thus, our genomic techniques are unveiling regions where we have a limited understanding of nutrient limitation.

Our approach is based on an assumption of rapid adaptation leading to direct association between genome content and environmental conditions (Giovannoni et al., 2005; Partensky & Garczarek, 2010; Swan et al., 2013; Tripp et al., 2010). Tropical and subtropical ocean regions have fast bacterial turnover leading to rapid selection. However, environments with slow bacterial turnover may include ecotypes or genes that represent past environmental conditions (rather than current). Different lineages may also experience unique stress (Alexander et al., 2015). Our dataset includes few representative

stations from high latitudes, where light or temperature may be limiting rather than nutrients (Dickman et al., 2006; Thomas et al., 2016). In such conditions, transcriptomics or proteomics may be more applicable. However, these techniques suffer from their own caveats like strong diel cycles (Ottesen et al., 2014; Poretsky et al., 2009) or low correlation between RNA and protein expression (Jayapal et al., 2008; Maier et al., 2011). Thus, the exact link between 'omics measurements and biogeochemical processes needs to be tailored to the system of interest.

'Omics techniques can be powerful for understanding the environmental conditions experienced by microorganisms. This principle is also applied in other ecosystem settings. A high presence of Proteobacteria in the human gut may be an indicator of an imbalance in the redox potential and 'ecosystem' dysbiosis (Shin et al., 2015). Similarly, the presence of ammonia monooxygenase may be indicative of nitrification (Francis et al., 2005). In many ecosystems, it can be very challenging to quantify microbial physiology and stress. Thus, a carefully calibrated genomic approach could become a widespread tool for understand microbial responses to environmental changes and the biogeochemical outcomes.

Acknowledgments

We would like to thank Jim Prosser and Jennifer Martiny for organizing this special issue and the National Science Foundation (NSF) (OCE-1559002, OCE-1848576, OCE-1756054) the National Aeronautics and Space Administration Earth and Space Science Fellowship (NESSF16R) and NIH T32AI141346 for supporting this work. GIH acknowledges the support of NSF grant OCE-1848576 and Simons Foundation Grant Number: 395890. We would like to thank Claudia Weihe for guidance in preparing

metagenome libraries, and the scientists and crews aboard the NH1418, AE1319, BV46, and I09 cruises for their effort.

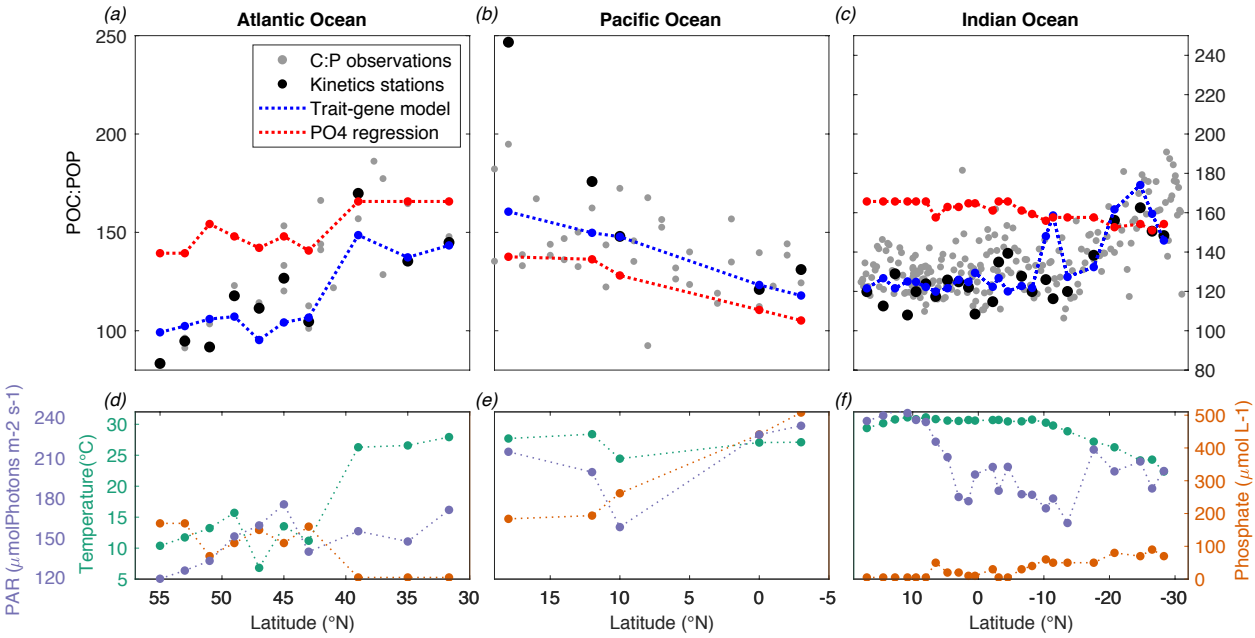

Figure 3.1. Observations and predictions of seston elemental stoichiometry. In situ measurements of particulate organic matter C:P are shown in gray, with selected stations in black where nutrient uptake incubations were performed for the A) Atlantic B) Pacific and C) Indian Oceans. Predicted C:P is shown by the ATOM-Syn trait-gene model (blue) and Galbraith-Martiny 2015 phosphate regression model (red).

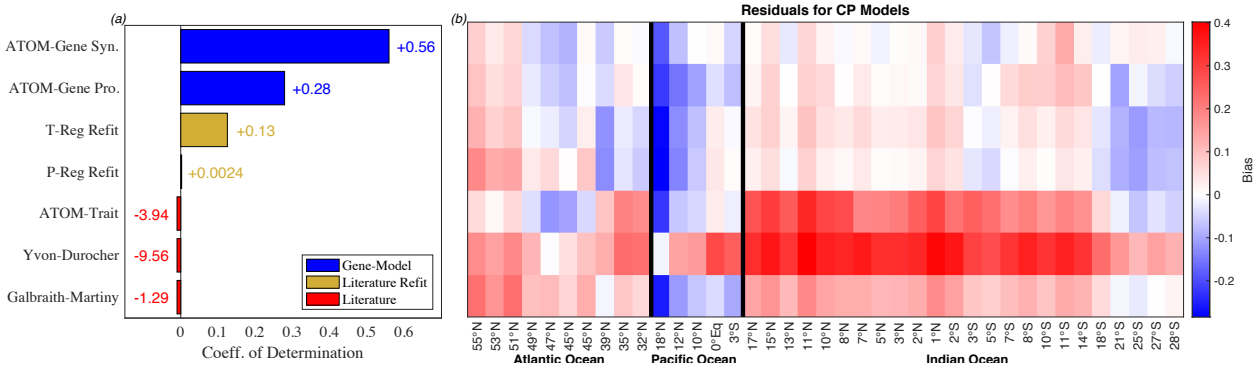

Figure 3.2. Trait model C:P bias. Statistical results for the predicted C:P models showing A) R2 and B) residuals (predictions – observations) across stations where surface C:P measurements were taken.

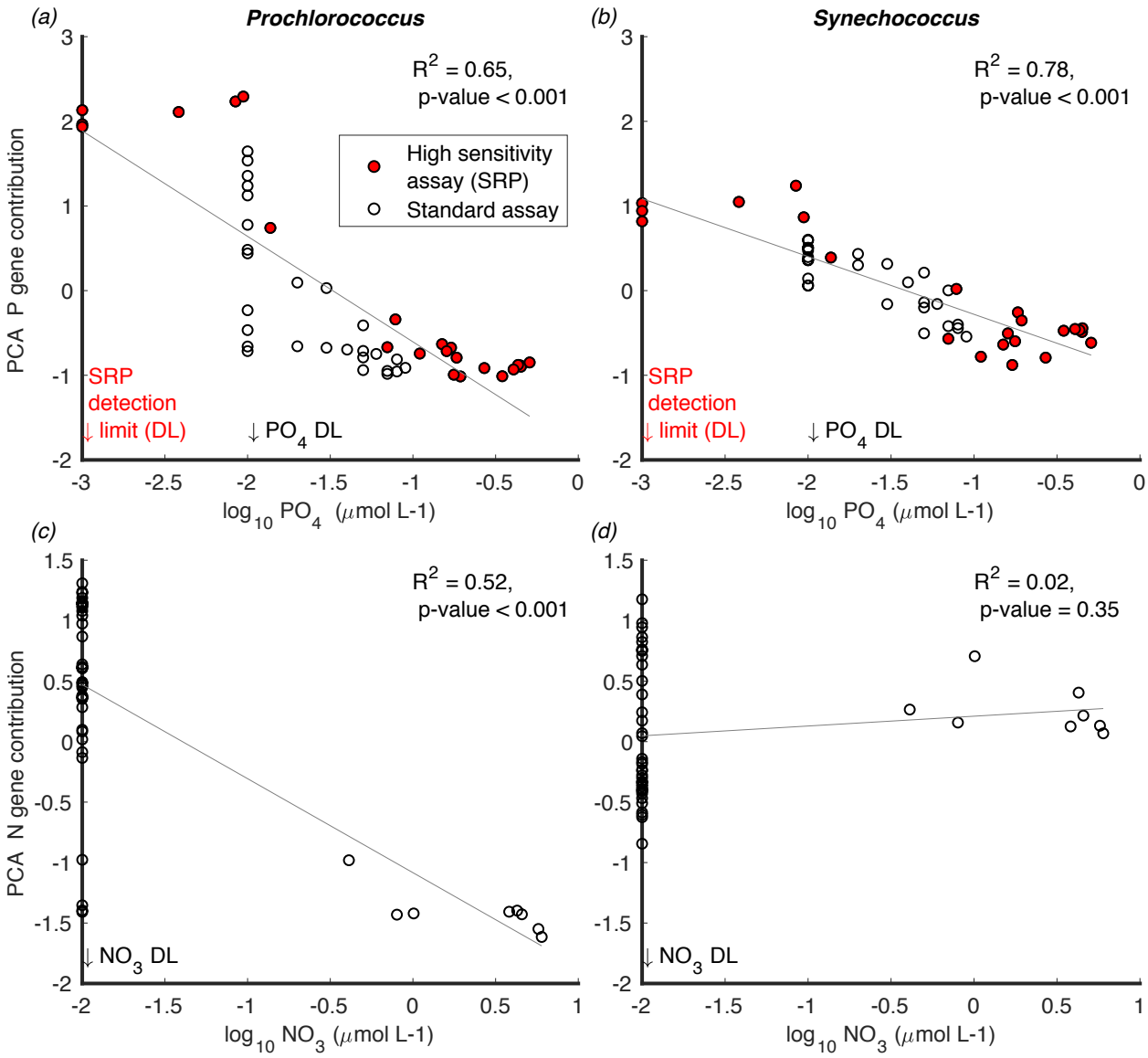

Figure 3.3. PCA component 1 versus nutrient concentrations. In situ nutrient concentrations for phosphate and nitrate are plotted against the first principle component calculated from relative gene frequencies for A) Prochlorococcus phosphorus assimilation genes (R2 = 0.65, p-value < 1E-8), B) Synechococcus phosphorus assimilation genes (R2 = 0.52, p-value < 1E-8, C) Prochlorococcus nitrogen assimilation genes (R2 = 0.78, p-value < 1E-8), and D) Synechococcus nitrogen assimilation genes (R2 = 0.02, p-value = 0.35). High sensitivity phosphate measurements (magenta square) were done using a MAGIC-SRP assay. Otherwise nitrate and phosphate observations were taken using standard methods (blue diamonds). DL = Detection limit.

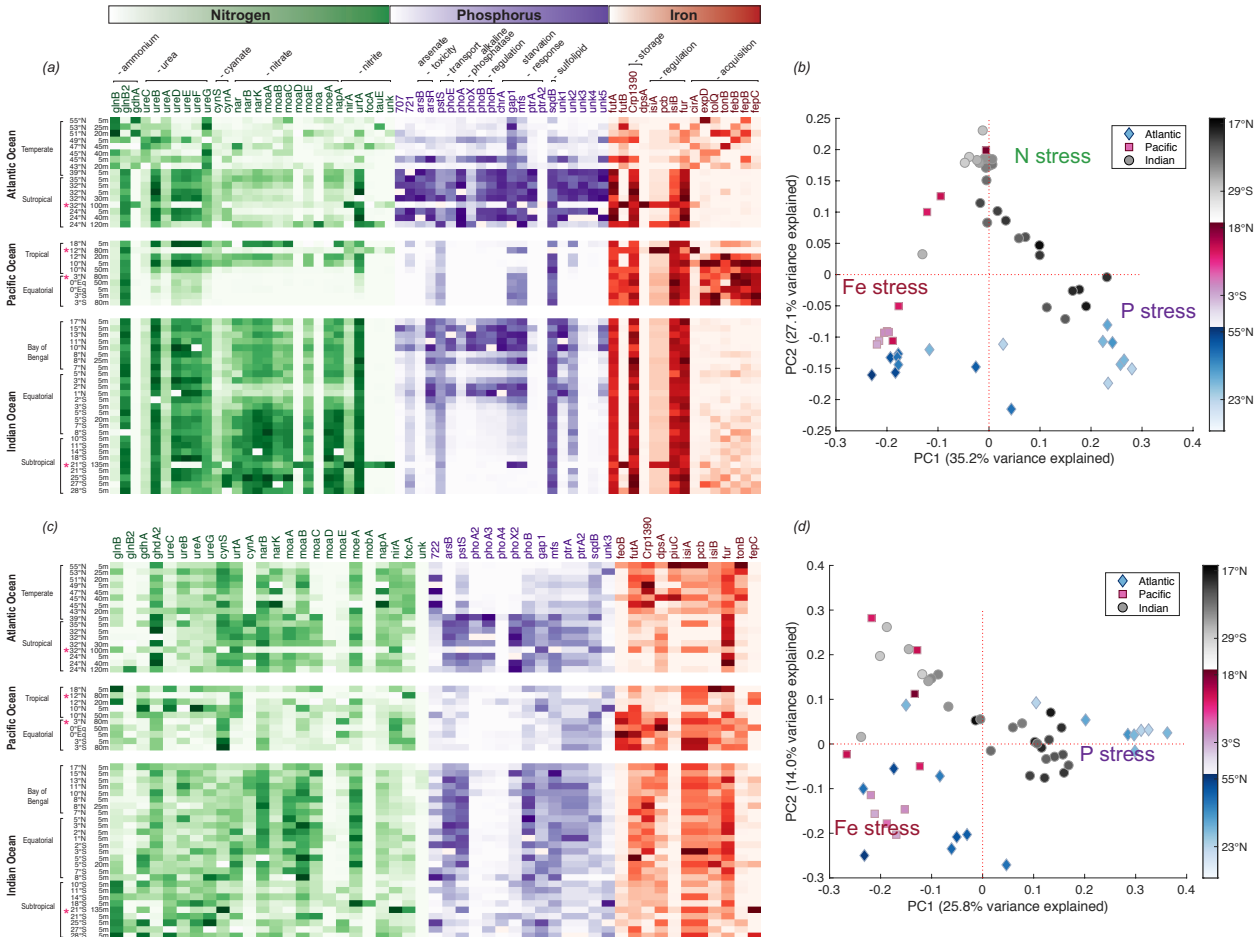

Figure 3.4. Variation among relative gene frequencies between stations. Green = nitrogen, Purple = phosphorus, red = iron. Prochlorococcus (A,B) and Synechococcus (C,D) matrices based on normalized gene frequency are significantly correlated (Mantel test R = 0.65, p-value < 0.001).

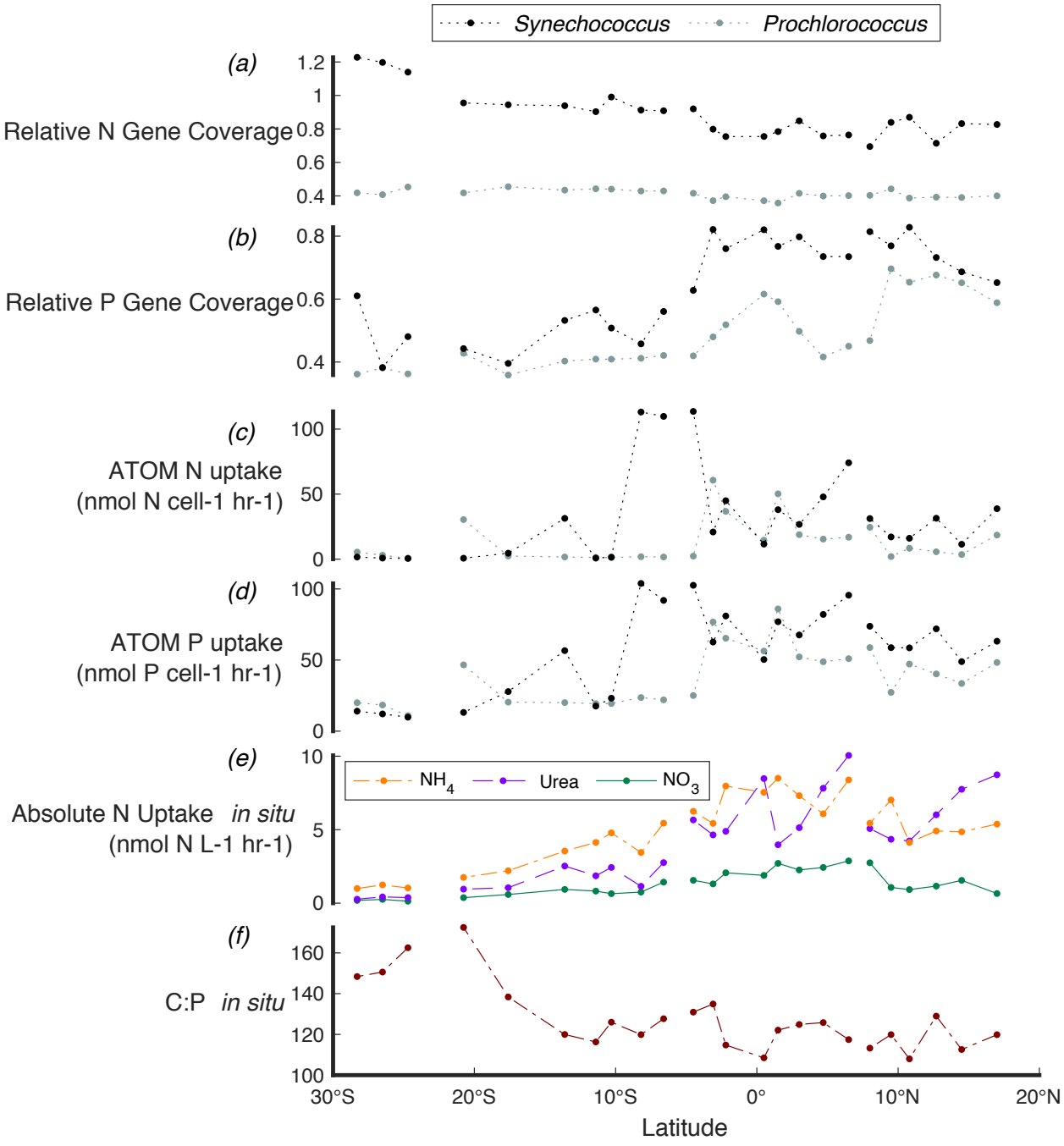

Figure 3.5. Evaluation of nutrient stress indices against ATOM-Gene and in situ uptake parameters in the Indian Ocean. Relative gene coverage of A) nitrogen and B) phosphorus genes is shown for Prochlorococcus (blue) and Synechococcus (orange-red). ATOM-Gene estimates for C) absolute N uptake and D) P affinity normalized to cell volume are compared to the in situ parameters of E) Specific uptake of N species (nitrate-magenta, urea-blue, ammonium-yellow) and F) the ratio of particulate organic carbon to phosphorus. In situ uptake rates and C:P are presented in [3,25].

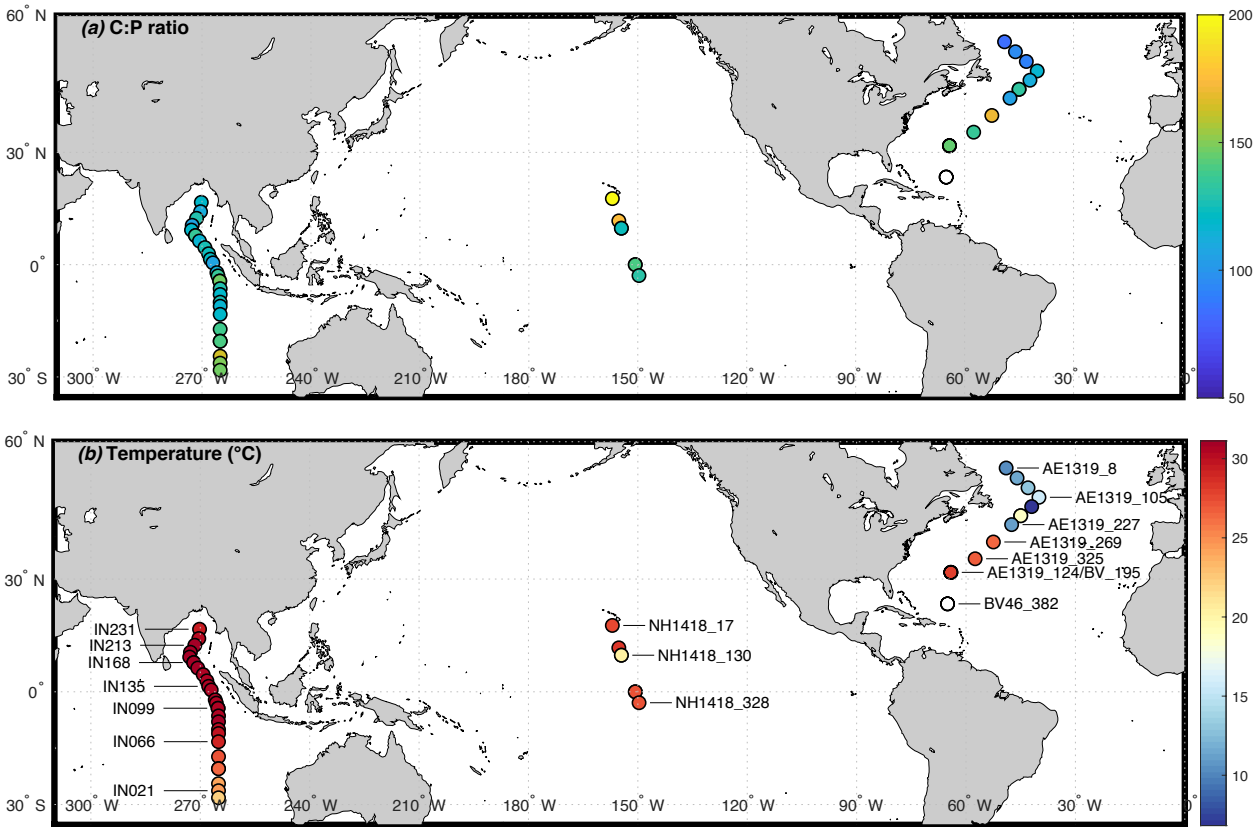

Figure S3.1. Map of transects AE1319/BVAL46 (Atlantic), NH1418 (Pacific), and I09 (Indian Ocean). Observations for the a) C:P ratios and b) temperature (□□Celsius) are shown with select stations labeled. Metagenomic samples AE1319_124 and BV46_195 are located at same site, but collected on different transects.

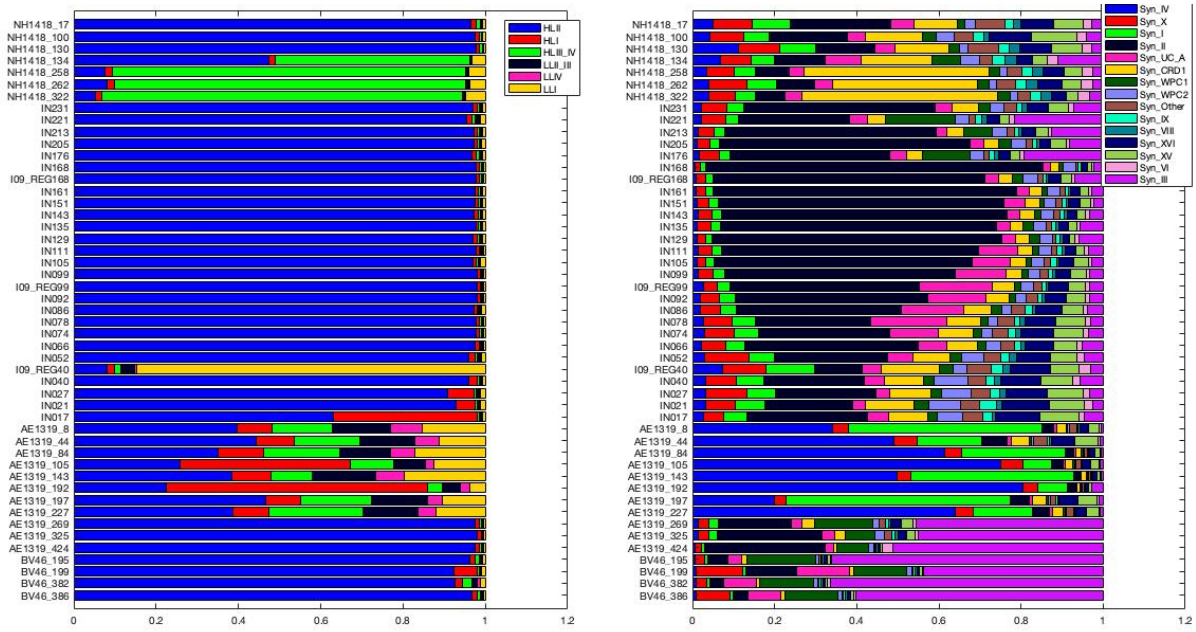

Figure S3.2. Clade abundance of *Prochlorococcus* and *Synechococcus* according to Table S3.4.

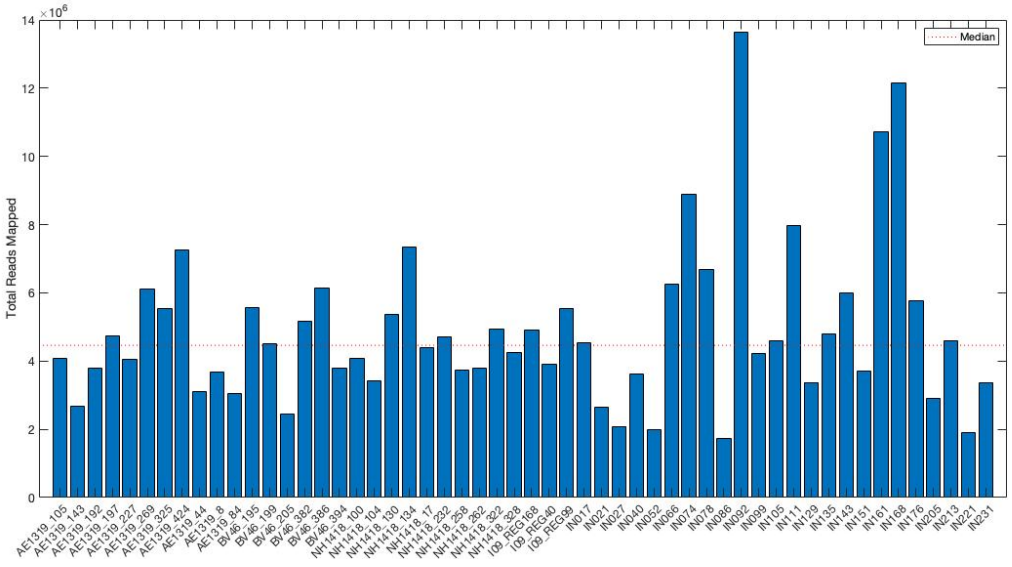

Figure S3.3. Total reads mapped per station.

(a) Nitrogen acquisition genes

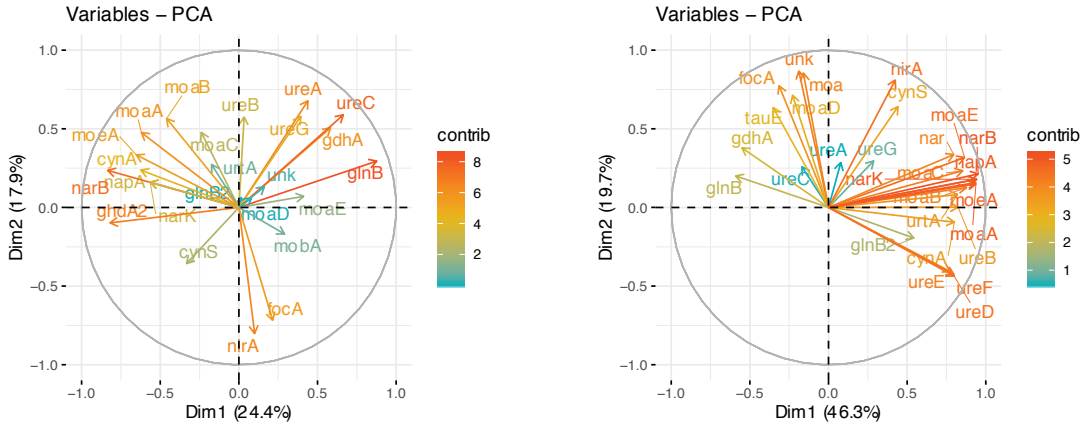

(b) Phosphorus acquisition genes

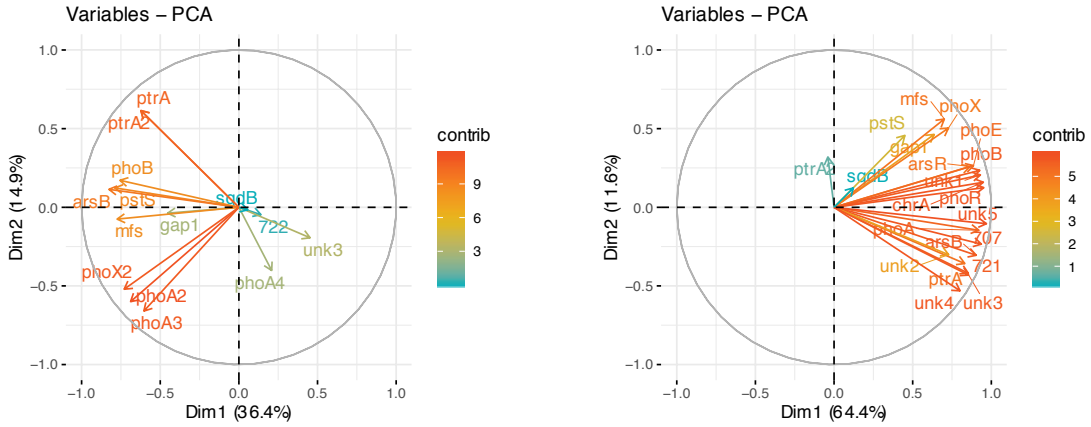

(c) Iron acquisition genes

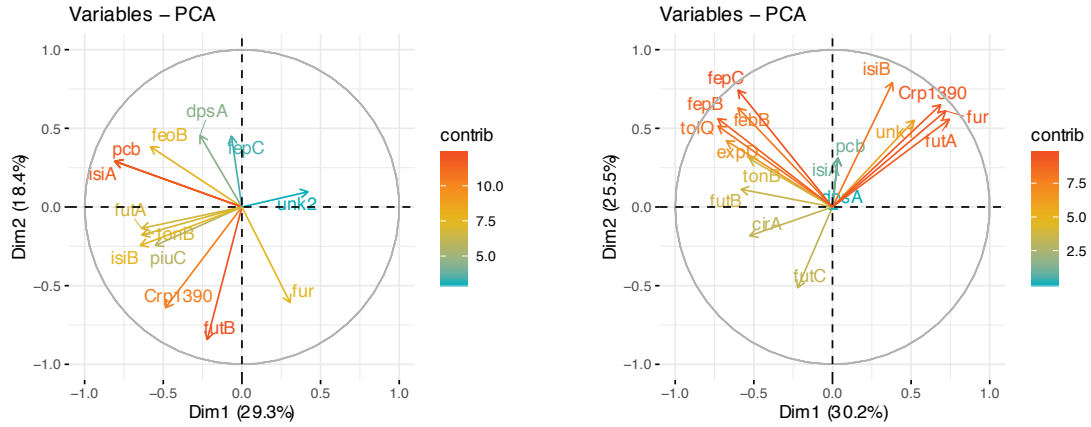

Synechococcus *Prochlorococcus*

Figure S3.4. Principle component analysis for stations using normalized gene coverages related to (A) Nitrogen, (B) Phosphorus, and (C) Iron acquisition.

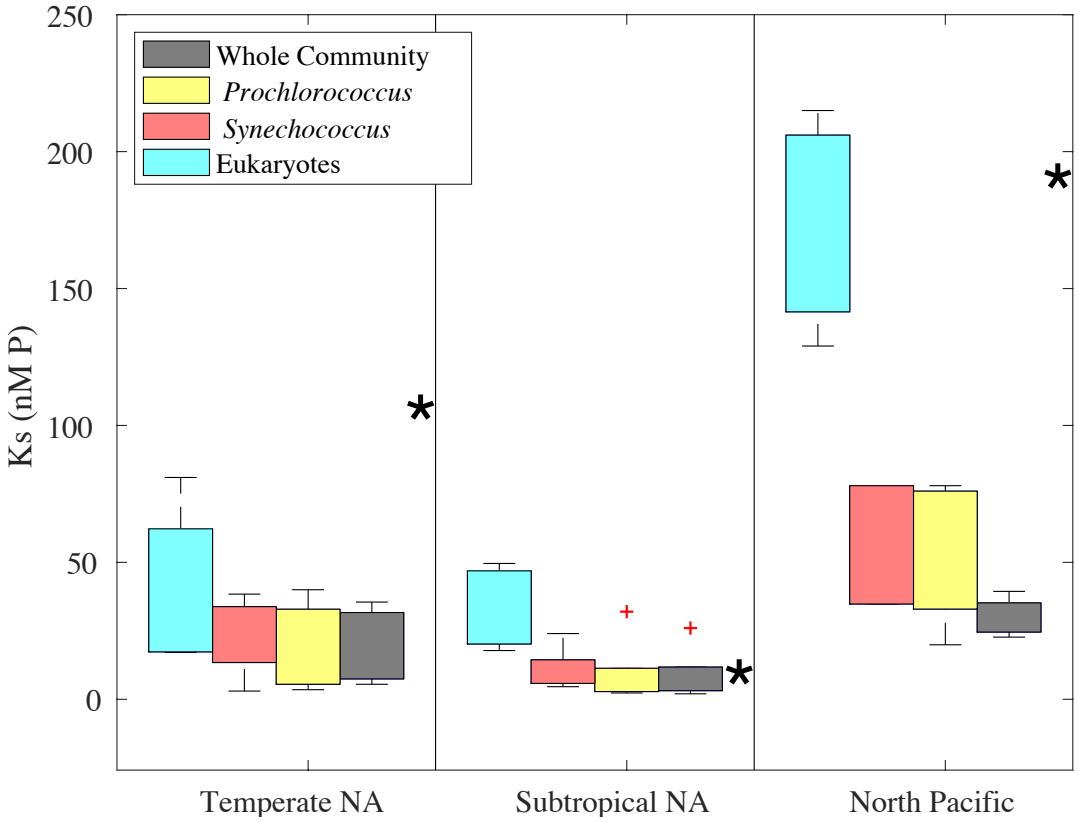

Figure S3.5. Boxplots of half saturation concentrations for phosphate in the North Atlantic (NA) and Pacific oceans. Average ambient phosphate concentrations are shown with an asterisk (*) for each region.

Table 3.1. Mean environmental characteristics for each ocean cruise transect.

Cruise	POC	POP	C:P	PO4	NO3	Pro abundance	Syn abundance	Pro Pmax	Pro Ks	Syn Pmax	Syn Ks	NH4 uptake	Urea uptake	NO3 uptake
	[uM]	[nM]		[nM]	[uM]	[cells ml-1]	[cells L-1]	[amol cell-1 hr-1]	[nmol L-1]	[amol cell-1 hr-1]	[nM]	[nM N h-1]	[nM N h-1]	[nM N h-1]
AE1319	3.0	23.2	167.5	36.5	6.1	34690	12164	8.9	10.6	39.5	29.9	NA	NA	NA
BVAL46	NA	7.1	NA	13.6	NA	54894	4307	10.4	5.9	46.8	11.4	NA	NA	NA
NH1418	1.6	10.8	153.1	74.1	2.3	82423	2858	0.6	54.5	0.6	56.4	NA	NA	NA
IO9	2.0	14.7	135.3	40.5	BD	145089	3236	NA	NA	NA	NA	4.9	4.2	1.3

Pro = *Prochlorococcus*, Syn = *Synechococcus*, Pmax = maximum uptake rate, Ks = half saturation PO4 concentration. BD = below detection and NA = not measured.

Table S3.2. Particulate organic matter observations for transects I09, NH1418, AE1319.

Metagenome SampleID	Latitude	Longitude	Depth	Datetime	POC	PON	POP	CN	CP	NP
unitless	[° N]	[°W]	[m]	unitless	[µmol/L]	[µmol/L]	[nmol/L]	unitless	unitless	unitless
AE1319_8	55.00	-49.00	5.00	26-Aug-2013	7.5	1.04	89.96	7.21	83.37	11.56
AE1319_44	53.00	-46.00	25.00	27-Aug-2013	11.52	1.52	121.62	7.58	94.72	12.50
AE1319_84	51.00	-43.00	20.00	28-Aug-2013	5.29	0.6	57.67	8.82	91.73	10.40
AE1319_105	49.00	-40.00	5.00	29-Aug-2013	5.66	0.63	48.06	8.98	117.77	13.11
AE1319_143	47.00	-42.00	45.00	30-Aug-2013	12.99	1.75	116.54	7.42	111.46	15.02
AE1319_197	45.00	-45.00	40.00	31-Aug-2013	14.51	1.91	120.7	7.60	120.22	15.82
AE1319_192	45.00	-45.00	5.00	31-Aug-2013	4.84	0.44	36.34	11.00	133.19	12.11
AE1319_227	43.00	-47.50	20.00	01-Sep-2013	7.16	0.98	68.43	7.31	104.63	14.32
AE1319_269	39.00	-52.50	5.00	03-Sep-2013	1.61	0.11	9.48	14.64	169.83	11.60
AE1319_325	35.00	-57.50	5.00	05-Sep-2013	1.58	0.17	11.67	9.29	135.39	14.57
AE1319_424	31.67	-64.17	5.00	08-Sep-2013	1.42	0.18	9.8	7.89	144.90	18.37
BV46_195	31.67	-64.17	5.00	05-Oct-2011	nan	nan	9.58	nan	nan	nan
BV46_199	31.67	-64.17	30.00	05-Oct-2011	nan	nan	11.91	nan	nan	nan
BV46_205	31.67	-64.17	100.00	05-Oct-2011	nan	nan	5.49	nan	nan	nan
BV46_382	23.67	-65.07	5.00	11-Oct-2011	nan	nan	5.47	nan	nan	nan
BV46_386	23.67	-65.07	40.00	11-Oct-2011	nan	nan	6.72	nan	nan	nan
BV46_394	23.67	-65.07	120.00	11-Oct-2011	nan	nan	6.24	nan	nan	nan
NH1418_17	18.00	-157.00	5.00	20-Sep-2014	1.48	0.16	6	9.25	246.67	26.67
NH1418_104	12.00	-155.22	80.00	22-Sep-2014	1.5	0.21	13.26	7.14	113.12	15.84
NH1418_100	12.00	-155.22	20.00	22-Sep-2014	1.5	0.25	8.53	6.00	175.85	29.31
NH1418_130	10.00	-154.52	5.00	23-Sep-2014	1.71	0.25	9.92	6.84	172.38	25.20
NH1418_134	10.00	-154.52	50.00	23-Sep-2014	2.55	0.35	20.64	7.29	123.55	16.96
NH1418_232	3.00	-151.74	80.00	26-Sep-2014	1.99	0.32	17.65	6.22	112.75	18.13
NH1418_258	0.00	-150.70	50.00	27-Sep-2014	3.01	0.53	29.41	5.68	102.35	18.02
NH1418_262	0.00	-150.70	5.00	27-Sep-2014	3.96	0.69	28.35	5.74	139.68	24.34
NH1418_322	-3.00	-149.67	5.00	28-Sep-2014	2.63	0.42	20.06	6.26	131.11	20.94
NH1418_328	-3.00	-149.67	80.00	28-Sep-2014	2.34	0.39	20.75	6.00	112.77	18.80
IN231	17.00	89.80	5.00	24-Apr-2016	1.66	0.27	13.82	6.19	119.86	19.45
IN221	14.50	89.60	5.00	22-Apr-2016	1.65	0.25	14.64	6.70	112.58	16.82
IN213	12.70	88.50	5.00	21-Apr-2016	1.71	0.26	13.25	6.57	128.96	19.65
IN205	10.80	87.30	5.00	20-Apr-2016	1.90	0.29	17.57	6.62	107.99	16.31
IN176	9.50	87.10	5.00	16-Apr-2016	1.94	0.30	16.21	6.42	119.89	18.72

IN168	8.00	88.20	5.00	16-Apr-2016	2.08	0.33	18.35	6.29	113.25	18.14
I09_REG168	7.98	94.87	25.00	21-Mar-2016	2.06	0.31	15.33	6.73	134.44	19.91
IN161	6.50	89.30	5.00	15-Apr-2016	2.07	0.32	17.61	6.45	117.44	18.21
IN151	4.70	90.80	5.00	13-Apr-2016	1.93	0.30	15.31	6.37	125.80	19.90
IN143	3.00	91.80	5.00	12-Apr-2016	2.09	0.33	16.74	6.34	124.86	19.70
IN135	1.50	92.30	5.00	11-Apr-2016	1.81	0.31	14.86	5.86	122.09	20.87
IN129	0.50	93.00	5.00	11-Apr-2016	1.91	0.30	17.61	6.31	108.49	17.19
IN111	-2.20	94.10	5.00	08-Apr-2016	1.75	0.24	15.29	7.29	114.77	15.77
IN105	-3.10	94.40	5.00	08-Apr-2016	1.92	0.29	14.24	6.68	134.91	20.28
IN099	-4.50	94.90	5.00	07-Apr-2016	2.02	0.28	15.44	7.24	130.93	18.07
I09_REG99	-4.53	94.87	20.00	07-Apr-2016	1.88	0.27	12.75	7.00	147.80	21.26
IN092	-6.60	95.00	5.00	05-Apr-2016	1.70	0.27	13.31	6.32	127.69	20.22
IN086	-8.20	95.00	5.00	05-Apr-2016	1.59	0.24	13.24	6.60	119.89	18.16
IN078	-10.30	95.00	5.00	03-Apr-2016	1.85	0.30	14.71	6.32	125.99	20.13
IN074	-11.40	95.00	5.00	03-Apr-2016	1.78	0.31	15.29	5.84	116.29	19.95
IN066	-13.60	95.00	5.00	01-Apr-2016	1.54	0.26	12.85	6.04	119.96	19.91
IN052	-17.60	95.00	5.00	30-Mar-2016	1.63	0.22	11.76	7.33	138.35	18.92
I09_REG40	-20.76	95.00	20.00	29-Mar-2016	1.59	0.23	9.22	6.81	172.49	25.43
IN040	-20.80	95.00	5.00	29-Mar-2016	1.74	0.22	12.48	8.09	139.77	17.33
IN027	-24.70	95.00	5.00	26-Mar-2016	1.68	0.24	10.32	7.11	162.53	22.85
IN021	-26.50	95.00	5.00	25-Mar-2016	1.68	0.23	11.17	7.64	150.59	20.21
IN017	-28.30	95.00	5.00	25-Mar-2016	1.74	0.20	11.74	8.59	148.37	17.32

Table S3.3. Inputs to ATOM models for transects I09, NH1418, AE1319.

Metagenome SampleID	Temperature	PAR	PO4	Phosphorus PCA1 *Prochlorococcus*	Nitrogen PCA1 *Prochlorococcus*	Phosphorus PCA1 *Synechococcus*	Nitrogen PCA1 *Synechococcus*
unitless	[°C]	[µmol m-2 s-1]	[µmol/L]	[unitless]	[unitless]	[unitless]	[unitless]
AE1319_8	10.4	262.8	nan	-0.85	-1.66	-0.86	-0.01
AE1319_44	11.7	256.7	0.17	-0.67	-1.43	-0.88	0.16
AE1319_84	13.2	244.3	0.07	-0.67	-1.40	-0.57	-0.30
AE1319_105	15.7	231.7	nan	0.34	-0.98	-0.51	-0.34
AE1319_143	6.8	319.6	0.15	-0.63	-1.21	-0.64	-0.29
AE1319_197	8.4	322.6	0.11	-0.74	-1.35	-0.78	0.39
AE1319_192	18.7	227.0	nan	1.18	-1.21	-0.33	-0.69
AE1319_227	11.2	289.4	0.16	-0.71	-1.41	-0.51	0.07
AE1319_269	26.3	182.7	0.001	2.13	0.08	1.03	-0.60
AE1319_325	26.6	185.2	0.001	1.96	0.28	0.82	-0.41
AE1319_424	27.9	181.2	0.001	1.94	0.02	0.94	-0.84
BV46_195	nan	318.9	0.01	2.23	-0.18	1.24	-0.96
BV46_199	nan	161.7	0.01	2.29	-0.05	0.87	-0.79
BV46_205	nan	24.1	0.08	-0.34	-1.08	0.02	0.87
BV46_382	nan	414.4	0.00	2.11	-0.51	1.05	-0.81
BV46_386	nan	184.5	nan	2.45	-0.14	0.83	-0.93
BV46_394	nan	29.0	0.01	0.74	-0.46	0.39	-0.10
NH1418_17	27.7	42.5	0.18	-0.79	1.31	-0.26	0.82
NH1418_104	19.6	73.2	0.27	-0.91	-1.42	-0.79	0.71
NH1418_100	28.4	0.1	0.19	-1.01	0.48	-0.35	0.71
NH1418_130	28.6	624.2	0.18	-0.99	0.36	-0.60	1.18
NH1418_134	20.3	6.8	0.35	-1.01	-0.98	-0.47	0.27
NH1418_232	27.3	34.4	0.45	-0.88	-1.41	-0.49	0.13
NH1418_258	27.0	51.4	0.45	-0.90	-1.43	-0.44	0.22
NH1418_262	27.1	731.3	0.43	-0.88	-1.40	-0.47	0.41
NH1418_322	27.1	714.8	0.51	-0.85	-1.55	-0.62	0.13
NH1418_328	26.6	12.8	0.41	-0.93	-1.62	-0.45	0.07
IN231	29.4	583.6	0	0.44	0.62	0.06	0.17
IN221	30.2	563.3	0	1.54	0.38	0.59	-0.18
IN213	30.8	576.5	0	1.36	0.49	0.37	-0.24
IN205	31.1	572.7	0	1.24	0.36	0.51	-0.33
IN176	30.8	567.9	0	1.65	0.87	0.50	-0.47

IN168	31.1	563.3	0	-0.23	0.62	0.40	-0.62
I09_REG168	31.1	215.1	0	0.48	0.45	0.36	-0.43
IN161	30.8	520.0	0.05	-0.41	0.61	0.21	-0.39
IN151	30.6	497.1	0.02	-0.66	0.64	0.30	-0.35
IN143	30.5	421.2	0.02	0.09	0.60	0.43	-0.51
IN135	30.7	417.8	0.01	0.78	-0.13	0.36	-0.40
IN129	30.6	465.6	0.01	1.12	-0.09	0.60	-0.59
IN111	30.7	482.4	0.03	0.03	0.47	0.32	-0.37
IN105	30.7	442.0	0	-0.47	0.38	0.47	-0.28
IN099	30.5	484.2	0	-0.66	0.98	0.06	-0.24
I09_REG99	30.5	327.2	0	-0.71	1.14	0.14	-0.14
IN092	30.5	434.6	0.03	-0.68	1.15	-0.16	0.05
IN086	30.8	433.5	0.04	-0.70	1.11	0.10	-0.17
IN078	30.3	406.2	0.06	-0.75	1.24	-0.16	0.64
IN074	29.8	425.3	0.05	-0.71	1.23	-0.14	0.76
IN066	28.9	386.9	0.05	-0.79	1.19	-0.20	0.24
IN052	27.2	523.8	0.05	-0.94	1.13	-0.50	0.50
I09_REG40	26.3	350.5	0.08	-0.81	0.10	-0.44	0.76
IN040	26.3	483.1	0.08	-0.96	1.08	-0.40	0.95
IN027	24.2	507.0	0.07	-0.95	1.52	-0.42	0.98
IN021	24.3	458.3	0.09	-0.91	1.14	-0.54	0.86
IN017	22.4	487.8	0.07	-0.98	1.04	0.00	0.75

Table S3.4. Correlations between *in situ* observations, gene frequencies, and ATOM-Gene properties.

R Correlation Coefficient	Nitrogen gene frequency *Prochloro.*	Phosphorus Gene frequency *Prochloro.*	Nitrogen gene frequency *Synechoco.*	Phosphorus gene frequency *Synechoco.*	NO3 rho	Urea rho	NH4 rho	CPObs
CPModelGM	-0.55*	0.74*	-0.77*	0.79*	0.55*	0.67*	0.67*	-0.62*
CPModelHM	-0.53*	0.74*	-0.77*	0.75*	0.51*	0.64*	0.65*	-0.63*
CPModelPReg	0.53*	-0.72*	0.79*	-0.79*	-0.56*	-0.68*	0.69*	0.64*
CPModelPro	0.78*	-0.48*	0.55*	-0.64*	-0.51*	-0.55*	0.44*	0.26
CPModelSyn	0.44*	-0.47*	0.73	-0.61	-0.64	-0.66	-0.70	0.67*
CPModelTReg	-0.37	0.54*	-0.87*	0.63*	0.67*	0.63*	0.81*	-0.80*
CPModelYvon	-0.38	0.54*	-0.87*	0.64*	0.67*	0.63*	0.81*	-0.80*
EVecPro	-0.80*	0.51*	-0.59*	0.67*	0.54*	0.57*	0.47*	-0.29
EVecSyn	-0.44*	0.48*	-0.75*	0.62*	0.66*	0.67*	0.71*	-0.67*
LVecPro	-0.83*	0.49*	-0.73*	0.73*	0.69*	0.60*	0.68*	-0.47*
LVecSyn	-0.44*	0.42*	-0.77*	0.61*	0.70*	0.62*	0.77*	-0.71*
LimStatePro	-0.52*	0.86*	-0.37	0.49*	0.19	0.35	0.32	-0.46
LimStateSyn	-0.67*	0.68*	-0.77*	0.87*	0.75*	0.67*	0.75*	-0.58
NAffPro	-0.82*	0.43*	-0.69*	0.72*	0.69*	0.52*	0.65*	-0.34*
NAffSyn	-0.34	0.25	-0.65*	0.46*	0.67*	0.55*	0.69*	-0.50*
NUptakePro	-0.68*	0.18	-0.44*	0.49*	0.46*	0.23	0.42*	-0.05
NUptakeSyn	-0.05	-0.09	-0.28	0.05	0.37	0.25	0.38	-0.21
PAffPro	-0.84*	0.45*	-0.69*	0.73*	0.69*	0.52*	0.65*	-0.35
PAffSyn	-0.36	0.27	-0.66*	0.48*	0.68*	0.56*	0.70*	-0.51*
PInvPro	0.82*	-0.45*	0.66*	-0.69*	-0.63*	-0.57*	0.58*	0.35
PInvSyn	0.82*	-0.45*	0.66*	-0.69*	-0.63*	-0.57*	0.58*	0.35
PQuotaPro	-0.71*	0.22	-0.48*	0.54*	0.51*	0.26	0.48*	-0.11
PQuotaSyn	-0.07	-0.08	-0.30	0.08	0.40	0.27	0.40	-0.21
PUptakePro	-0.68*	0.18	-0.44*	0.49*	0.45*	0.23	0.42	-0.05
PUptakeSyn	-0.05	-0.09	-0.28	0.05	0.37	0.25	0.38	-0.21
ProVolume	-0.74*	0.27	-0.47*	0.54*	0.54*	0.26	0.51	-0.15
SynVolume	-0.13	-0.05	-0.36	0.14	0.47	0.32	0.46	-0.25
rVecPro	-0.81*	0.38	-0.61*	0.66*	0.62*	0.46*	0.57*	-0.25
rVecSyn	-0.33	0.23	-0.62*	0.43*	0.65*	0.54*	0.66*	-0.48*

Significant correlations (p-value < 0.05) are indicated by a star (*), with negative relationships in blue and positive in red.

Table S3.5. Genomes and clades for *Prochlorococcus* and *Synechococcus*		
Taxa	Genome	Clade
Synechococcus	GEYO	Syn.CRD1
Synechococcus	MITS9508	Syn.CRD1
Synechococcus	MITS9509	Syn.CRD1
Synechococcus	UW179A	Syn.CRD1
Synechococcus	CC9311	Syn.I
Synechococcus	UW179B	Syn.I
Synechococcus	WH8016	Syn.I
Synechococcus	WH8020	Syn.I
Synechococcus	CC9605	Syn.II
Synechococcus	N19	Syn.II
Synechococcus	N32	Syn.II
Synechococcus	REDSEA_S02_B4	Syn.II
Synechococcus	UW86	Syn.II
Synechococcus	WH8109	Syn.II
Synechococcus	WH8102	Syn.III
Synechococcus	BL107	Syn.IV
Synechococcus	CC9902	Syn.IV
Synechococcus	RS9916	Syn.IX
Synechococcus	NKBG042902	Syn.Other
Synechococcus	PCC7335	Syn.Other
Synechococcus	CC9616	Syn.UC-A
Synechococcus	KORDI_100	Syn.UC-A
Synechococcus	WH7805	Syn.VI
Synechococcus	RS9917	Syn.VIII
Synechococcus	KORDI_49	Syn.WPC1
Synechococcus	KORDI_52	Syn.WPC2
Synechococcus	CB0101	Syn.X
Synechococcus	CB0205	Syn.X
Synechococcus	GFB01	Syn.X
Synechococcus	RCC307	Syn.X
Synechococcus	WH5701	Syn.X
Synechococcus	UW106	Syn.XV
Synechococcus	UW69	Syn.XV
Synechococcus	UW105	Syn.XVI
Synechococcus	UW140	Syn.XVI
Prochlorococcus	EQPAC1	HLI
Prochlorococcus	MED4	HLI
Prochlorococcus	MIT9515	HLI
Prochlorococcus	AS9601	HLII
Prochlorococcus	GP2	HLII
Prochlorococcus	MIT0604	HLII
Prochlorococcus	MIT9123	HLII
Prochlorococcus	MIT9201	HLII
Prochlorococcus	MIT9215	HLII
Prochlorococcus	MIT9301	HLII
Prochlorococcus	MIT9302	HLII
Prochlorococcus	MIT9312	HLII
Prochlorococcus	MIT9314	HLII
Prochlorococcus	MIT9322	HLII
Prochlorococcus	MIT9401	HLII

Prochlorococcus	SB	HLII
Prochlorococcus	SCGCAAA795_I06	HLII
Prochlorococcus	SCGCAAA795_I15	HLII
Prochlorococcus	SCGCAAA795_M23	HLII
Prochlorococcus	UH18301	HLII
Prochlorococcus	HNLC1	HLIII-IV
Prochlorococcus	HNLC2	HLIII-IV
Prochlorococcus	RS50	HLII
Prochlorococcus	XMU1401	HLII
Prochlorococcus	XMU1403	LLI
Prochlorococcus	XMU1408	LLI
Prochlorococcus	MIT0801	LLI
Prochlorococcus	NATL1A	LLI
Prochlorococcus	NATL2A	LLI
Prochlorococcus	PAC1	LLI
Prochlorococcus	MIT0601	LLII-III
Prochlorococcus	MIT0602	LLII-III
Prochlorococcus	MIT9211	LLII-III
Prochlorococcus	SS120	LLII-III
Prochlorococcus	MIT0701	LLIV
Prochlorococcus	MIT1312	LLIV
Prochlorococcus	MIT1313	LLIV
Prochlorococcus	MIT1318	LLIV
Prochlorococcus	MIT1327	LLIV
Prochlorococcus	MIT1342	LLIV
Prochlorococcus	MIT9303	LLIV
Prochlorococcus	MIT9313	LLIV

SUMMARY AND FUTURE DIRECTIONS

Surface phytoplankton exist at the nexus between carbon uptake and export. Microbial communities have evolved to exploit available niches by optimizing their cellular resources (Beck et al., 2017; Hall, 2009; Harcombe et al., 2014). The range in environmental conditions had led to a latitudinal gradient in particulate C:N:P ratios (Martiny et al., 2013). The flexible stoichiometric ratios observed in small phytoplankton (Martiny et al., 2013) may provide a buffer against reduced carbon export across oligotrophic biomes (Tanioka & Matsumoto, 2017). In my dissertation I aimed to evaluate the regional importance of specific environmental gradients (e.g. temperature and nutrients). It is difficult to isolate the primary biological stressor in complex ecosystems. Whole-lake experiments completed by Elser and colleagues (Elser et al., 1998, 2000) remain among the best modern examples to isolate trophic and environmental drivers regulating planktonic C:N:P. Oceans, however, cover 70% of the Earth's surface and represent a vast ecosystem circulating over millennia timescales. Perturbation experiments cannot be conducted, either purposely (Martin et al., 1994) or accidentally (Mason et al., 2012), without unknown ecosystem consequences. Natural gradients present themselves as an alternative to test lab-based hypotheses.

By using the unique environmental gradients in the Indian Ocean, this thesis provides evidence that nutrients are the primary stressor driving low latitude C:N:P variation (Garcia et al., 2018). Oceanic subtropical biomes are predicted in expand under a warming climate (Polovina et al., 2008). The impacts on particulate matter formation and export will partly be shaped by the phytoplankton response (Tanioka & Matsumoto, 2017). The intermonsoon season in the Indian Ocean contains a stable surface phytoplankton community dominated by *Prochlorococcus* cyanobacteria (Baer et al., 2018; Larkin et al.,

2019). Thus, we assume that C:N:P variation is a community response to an environmental gradient of temperature or nutrients. We found no support for increased ribosomal efficiency (Toseland et al., 2013) in the warmest ocean on the planet. However, it would be unwise to continue examining the impact of temperature on one cellular process alone. Phytoplankton metabolic rates are predicted to increase with temperature under high nutrient supply, but the metabolic cost under nutrient stress is unknown (Marañón et al., 2018). Looking forward, temperature should be evaluated in combination with nutrient stress via its effects on nutrient recycling (Ayo et al., 2017) and stratification (Goldman et al., 1996).

Quantifying nutrient availability remains a large challenge in ocean biogeochemistry. Traditionally, phosphate is considered the ultimate nutrient control on phytoplankton productivity (Tyrrell, 1999). As such, current stoichiometric models use phosphate as the limiting nutrient on C:P (Galbraith & Martiny, 2015; Moreno et al., 2018). For this reason, we created a satellite proxy for surface phosphate. However, our results suggest multiple nutrients interact to limit phytoplankton growth. First, our neural network analysis suggested a strong component of iron supply in leading to low phosphate concentrations. Iron is widely proposed to limit nitrogen fixation (Moore et al., 2009; Moore & Doney, 2007). Second, while phosphate successfully predicts C:P in traditionally P-limited regions (Atlantic Ocean & Mediterranean Sea), it was a poor predictor of C:P in the South Indian subtropical gyre (Garcia et al., 2020). The accumulation of phosphate in the nutrient pool, and not in the particulate pool may be driven by N limitation (Moutin et al., 2008). Cyanobacteria depend on an N currency source in order to invest in uptake transporters needed to assimilate available phosphate (Bonachela et al., 2013). Nitrate was below

detection limits across the surface Indian Ocean. This is a large hurdle to evaluating *in situ* co-limitation patterns. While low level nutrient assays exist (Dore et al., 1996; Karl & Tien, 1992; Li et al., 2008), more direct measurements with these novel assays will be needed in nutrient-poor regions.

It is currently impossible to predict microbial nutrient use and associated biogeochemical roles even with a perfect chemical characterization of an environment. Phytoplankton use a variety of alternative nutrient forms, both organic and inorganic forms in a variety of oxidative states (Bronk et al., 2007; Dyhrman et al., 2006; Huang & Hong, 1999; Moore et al., 2002; Sosa et al., 2019). To overcome this challenge, we used genomic shifts among microbial communities as a 'biosensor' for in situ nutritional environments in order to improve predictions of C:P variability across ocean regions (Garcia 2020). Recently, multiple studies have leveraged the functional diversity of microbes to predict biogeochemical patterns (Coles et al., 2017; Hennon & Dyhrman, 2019). The genomes of abundant microbial taxa are streamlined in nutrient-poor biomes (Giovannoni et al., 2005; Swan et al., 2013; Tripp et al., 2010). Stable, microdiverse Cyanobacterial clades are associated with environmental light, temperature, and nutrient gradients (Kent et al., 2019; Larkin & Martiny, 2017). Quantifying the genomic variability in genes associated with these environmental factors strongly suggests adaptation to a particular stress (Malmstrom et al., 2013; Martiny et al., 2006). We developed a nutrient index for N, P, and Fe that could easily be incorporated into a phytoplankton trait model (Garcia et al., 2020). While our method was successful for small cyanobacteria, larger phytoplankton are able retain a lager suite of genes. Generalist plankton may not show metagenomic variation of gene gain and loss, and proteomics or transcriptomics may be more appropriate. Future studies should evaluate

conditions where ‘omics approaches can be incorporated into simple environmental indices.

Approximating correct particle stoichiometry has implications for biological processes including the regulation of primary productivity and the biological pump (Emerson et al., 2001; Schneider et al., 2004; Teng et al., 2014). The flexible stoichiometric ratios observed in small phytoplankton (Martiny et al., 2013) may provide a buffer against reduced carbon export across oligotrophic biomes (Tanioka & Matsumoto, 2017). To what extent the diversity of larger phytoplankton impacts the variability of organic matter remineralization in the deep thermocline remains an important question for modeling nutrient recycling and export in the Southern Ocean (Moore et al., 2018; Lomas et al., 2019; Weber & Deutsch, 2010)(Moore et al., 2018; Lomas et al., 2019; Weber & Deutsch, 2010). There is a strong push to incorporate a more diverse plankton community structure (Fu et al., 2016; Tréguer et al., 2018), and acclimation to multiple nutrients into global biogeochemical models (Buchanan et al., 2018; Flynn, 2010; Glibert et al., 2013). We evaluate important regional predictors with the hope of improving dynamic resource allocation models (Moreno et al., 2018; Smith et al., 2016). However, introducing additional complexity remains a real challenge. By assuming balanced growth at equilibrium, the trait models above can bridge this gap using an “instantaneous” biological response instead of a fully dynamic model (Ward, 2017). Looking forward, particulate C:N:P ratios can help evaluate how and where changing temperatures, nutrient availability, and community structure will impact biogeochemical cycling.

REFERENCES

Alexander, H., Rouco, M., Haley, S. T., Wilson, S. T., Karl, D. M., & Dyhrman, S. T. (2015). Functional group-specific traits drive phytoplankton dynamics in the oligotrophic ocean. *Proceedings of the National Academy of Sciences of the United States of America*, *112*(44), E5972–E5979. https://doi.org/10.1073/pnas.1518165112

Alexander, H., Jenkins, B. D., Rynearson, T. A., & Dyhrman, S. T. (2015). Metatranscriptome analyses indicate resource partitioning between diatoms in the field. *Proceedings of the National Academy of Sciences of the United States of America*, *112*(17), E2182–E2190. https://doi.org/10.1073/pnas.1421993112

Antelmann, H., Scharf, C., & Hecker, M. (2000). Phosphate starvation-inducible proteins of Bacillus subtilis: Proteomics and transcriptional analysis. *Journal of Bacteriology*, *182*(16), 4478–4490. https://doi.org/10.1128/JB.182.16.4478-4490.2000

Arrigo, K. R. (2005). Marine microorganisms and global nutrient cycles. *Nature*, *437*(September), 349–355. https://doi.org/10.1038/nature04159

Arteaga, L., Pahlow, M., & Oschlies, A. (2015). Global monthly sea surface nitrate fields estimated from remotely sensed sea surface temperature, chlorophyll, and modeled mixed layer depth. *Geophysical Research Letters*, *42*(4), 1130–1138. https://doi.org/10.1002/2014GL062937

Ayo, B., Abad, N., Artolozaga, I., Azua, I., Baña, Z., Unanue, M., et al. (2017). Imbalanced nutrient recycling in a warmer ocean driven by differential response of extracellular enzymatic activities. *Global Change Biology*, *23*(10), 4084–4093. https://doi.org/10.1111/gcb.13779

Baer, S. E., Lomas, M. W., Terpis, K. X., Mouginot, C., & Martiny, A. C. (2017). Stoichiometry of Prochlorococcus, Synechococcus, and small eukaryotic populations in the western North Atlantic Ocean. *Environmental Microbiology*, *19*(4), 1568–1583. https://doi.org/10.1111/1462-2920.13672

Baer, S. E., Rauschenberg, S., Garcia, C. A., Garcia, N. S., Martiny, A. C., Twining, B. S., & Lomas, M. W. (2018). Carbon and nitrogen productivity during spring in the oligotrophic Indian Ocean along the GO-SHIP IO9N transect. *Deep Sea Research Part II: Topical Studies in Oceanography*. https://doi.org/10.1016/J.DSR2.2018.11.008

Beck, A., Bernstein, H., & Carlson, R. (2017). Stoichiometric Network Analysis of Cyanobacterial Acclimation to Photosynthesis-Associated Stresses Identifies Heterotrophic Niches. *Processes*, *5*(4), 32. https://doi.org/10.3390/pr5020032

Behrenfeld, M. J., Westberry, T. K., Boss, E. S., O'Malley, R. T., Siegel, D. a., Wiggert, J. D., et al. (2008). Satellite-detected fluorescence reveals global physiology of ocean phytoplankton. *Biogeosciences Discussions*, *5*(6), 4235–4270. https://doi.org/10.5194/bgd-5-4235-2008

Behrenfeld, Michael J., & Falkowski, P. G. (1997). Photosynthetic rates derived from satellite-based chlorophyll concentration. *Limnology and Oceanography*, *42*(1), 1–20. https://doi.org/10.4319/lo.1997.42.1.0001

Berger, C. J. M., Lippiatt, S. M., Lawrence, M. G., & Bruland, K. W. (2008). Application of a chemical leach technique for estimating labile particulate aluminum, iron, and manganese in the Columbia River plume and coastal waters off Oregon and Washington. *Journal of Geophysical Research*, *113*(C2), C00B01. https://doi.org/10.1029/2007JC004703

Berube, P. M., Biller, S. J., Kent, A. G., Berta-Thompson, J. W., Roggensack, S. E., Roache-Johnson, K. H., et al. (2015). Physiology and evolution of nitrate acquisition in Prochlorococcus. *ISME Journal*, *9*(5), 1195–1207. https://doi.org/10.1038/ismej.2014.211

Bolger, A. M., Lohse, M., & Usadel, B. (2014). Trimmomatic: A flexible trimmer for Illumina sequence data. *Bioinformatics*, *30*(15), 2114–2120. https://doi.org/10.1093/bioinformatics/btu170

Bonachela, J. A., Raghib, M., & Levin, S. A. (2011). Dynamic model of flexible phytoplankton nutrient uptake. *Proceedings of the National Academy of Sciences*. https://doi.org/10.1073/pnas.1118012108

Bonachela, J. A., Allison, S. D., Martiny, A. C., & Levin, S. A. (2013). A model for variable phytoplankton stoichiometry based on cell protein regulation. *Biogeosciences*, *10*(6), 4341–4356. https://doi.org/10.5194/bg-10-4341-2013

Boström, K. H., Simu, K., Hagström, Å., & Riemann, L. (2004). Optimization of DNA extraction for quantitative marine bacterioplankton community analysis. *Limnology and Oceanography: Methods*, *2*(11), 365–373. https://doi.org/10.4319/lom.2004.2.365

Boyd, P. W., Watson, A. J., Law, C. S., Abraham, E. R., Trull, T., Murdoch, R., et al. (2000). A mesoscale phytoplankton bloom in the polar Southern Ocean stimulated by iron fertilization. *Nature*, *407*(6805), 695–702. https://doi.org/10.1038/35037500

Bronk, D. A., See, J. H., Bradley, P., & Killberg, L. (2007). *DON as a source of bioavailable nitrogen for phytoplankton*. *European Geosciences Union* (Vol. 4). Retrieved from www.biogeosciences.net/4/283/2007/

Buchanan, P. J., Matear, R. J., Chase, Z., Phipps, S. J., & Bindoff, N. L. (2018). Dynamic Biological Functioning Important for Simulating and Stabilizing Ocean Biogeochemistry. *Global Biogeochemical Cycles*, *32*(4), 565–593. https://doi.org/10.1002/2017GB005753

Buchfink, B., Xie, C., & Huson, D. H. (2014, January 1). Fast and sensitive protein alignment using DIAMOND. *Nature Methods*. Nature Publishing Group. https://doi.org/10.1038/nmeth.3176

Capone, D. G., O'neil, J. M., Zehr, J., & Carpenter, E. J. (1990). Basis for Diel Variation in Nitrogenase Activity in the Marine Planktonic Cyanobacterium Trichodesmium thiebautii. *Applied and Environmental Microbiology*, *56*(11), 3532–6. Retrieved from http://www.ncbi.nlm.nih.gov/pubmed/16348357

Caputi, L., Carradec, Q., Eveillard, D., Kirilovsky, A., Pelletier, E., Pierella Karlusich, J. J., et al. (2019). Community-Level Responses to Iron Availability in Open Ocean Plankton Ecosystems. *Global Biogeochemical Cycles*, *33*(3), 391–419. https://doi.org/10.1029/2018GB006022

Carpenter, B., Gelman, A., Hoffman, M. D., Lee, D., Goodrich, B., Betancourt, M., et al. (2017). *Stan* : A Probabilistic Programming Language. *Journal of Statistical Software*, *76*(1), 1–32. https://doi.org/10.18637/jss.v076.i01

Casey, J. R., Aucan, J. P., Goldberg, S. R., & Lomas, M. W. (2013). Changes in partitioning of carbon amongst photosynthetic pico- and nano-plankton groups in the Sargasso Sea in response to changes in the North Atlantic Oscillation. *Deep-Sea Research Part II: Topical Studies in Oceanography*, *93*, 58–70. https://doi.org/10.1016/j.dsr2.2013.02.002

Cermeño, P., Dutkiewicz, S., Harris, R. P., Follows, M., Schofield, O., & Falkowski, P. G. (2008). The role of nutricline depth in regulating the ocean carbon cycle. *Proceedings of the National Academy of Sciences of the United States of America*, *105*(51), 20344–9. https://doi.org/10.1073/pnas.0811302106

Clark, D. R., Flynn, K. J., & Fabian, H. (2014). Variation in elemental stoichiometry of the marine diatom Thalassiosira weissflogii (Bacillariophyceae) in response to combined nutrient stress and changes in carbonate chemistry. *Journal of Phycology*, *50*(4), 640–651. https://doi.org/10.1111/jpy.12208

Coale, K. H., Johnson, K. S., Fitzwater, S. E., Gordon, R. M., Tanner, S., Chavez, F. P., et al. (1996). A massive phytoplankton bloom induced by an ecosystem-scale iron fertilization experiment in the equatorial Pacific Ocean. *Nature*, *383*(6600), 495. https://doi.org/10.1038/383495a0

Codispoti, L. ., Friederich, G. ., Sakamoto, C. ., & Gordon, L. . (1991). Nutrient cycling and primary production in the marine systems of the Arctic and Antarctic. *Journal of Marine Systems*, *2*(3–4), 359–384. https://doi.org/10.1016/0924-7963(91)90042-S

Coleman, M. L., & Chisholm, S. W. (2010). Ecosystem-specific selection pressures revealed through comparative population genomics. *Proceedings of the National Academy of Sciences of the United States of America*, *107*(43), 18634–18639. https://doi.org/10.1073/pnas.1009480107

Coles, V. J., Stukel, M. R., Brooks, M. T., Burd, A., Crump, B. C., Moran, M. A., et al. (2017). Ocean biogeochemistry modeled with emergent trait-based genomics. *Science*, *358*(6367), 1149–1154. https://doi.org/10.1126/science.aan5712

Copin-Montegut, C., & Copin-Montegut, G. (1978). The chemistry of particulate matter from the south Indian and Antarctic oceans. *Deep-Sea Research*, *25*(10). https://doi.org/10.1016/0146-6291(78)90633-1

Deshpande, A., Gnanaseelan, C., Chowdary, J. S., & Rahul, S. (2017). Interannual spring Wyrtki jet variability and its regional impacts. *Dynamics of Atmospheres and Oceans*, *78*, 26–37. https://doi.org/10.1016/J.DYNATMOCE.2017.02.001

Dickman, E. M., Vanni, M. J., & Horgan, M. J. (2006). Interactive effects of light and nutrients on phytoplankton stoichiometry. *Oecologia*, *149*(4), 676–689. https://doi.org/10.1007/s00442-006-0473-5

Dietze, H., Oschlies, A., Kaler, P., & Kähler, P. (2004). Internal-wave-induced and double-diffusive nutrient fluxes to the nutrient-consuming surface layer in the oligotrophic subtropical North Atlantic. *Ocean Dynamics*, *54*(1), 1–7. https://doi.org/10.1007/s10236-003-0060-9

Dore, J. E., Houlihan, T., Hebel, D. V., Tien, G., Tupas, L., & Karl, D. M. (1996). Freezing as a method of sample preservation for the analysis of dissolved inorganic nutrients in seawater. *Marine Chemistry*, *53*(3–4), 173–185. https://doi.org/10.1016/0304-4203(96)00004-7

Ducklow, H., & Dickson, A. (1994). Shipboard Sampling Procedures. *Jgofs*, (January), 1–210.

Dyhrman, S. T., Chappell, P. D., Haley, S. T., Moffett, J. W., Orchard, E. D., Waterbury, J. B., & Webb, E. A. (2006). Phosphonate utilization by the globally important marine diazotroph Trichodesmium. *Nature*, *439*(7072), 68–71. https://doi.org/10.1038/nature04203

Elser, J. J., Chrzanowski, T. H., Sterner, R. W., & Mills, K. H. (1998). Stoichiometric constraints on food-web dynamics: A whole-lake experiment on the Canadian Shield.

Ecosystems, *1*(1), 120–136. https://doi.org/10.1007/s100219900009
Elser, J. J., Sterner, R. W., Galford, A. E., Chrzanowski, T. H., Findlay, D. L., Mills, K. H., et al. (2000). Pelagic C:N:P stoichiometry in a eutrophied lake: Responses to a whole-lake food-web manipulation. *Ecosystems*, *3*(3), 293–307. https://doi.org/10.1007/s100210000027
Emerson, S., Mecking, S., & Abell, J. (2001). The biological pump in subtropical North Pacific Ocean: Nutrient sources, Redfield ratios, and recent changes. *Global Biogeochemical Cycles*, *15*(3), 535–554. https://doi.org/10.1029/2000GB001320
Eren, A. M., Esen, O. C., Quince, C., Vineis, J. H., Morrison, H. G., Sogin, M. L., & Delmont, T. O. (2015). Anvi'o: An advanced analysis and visualization platformfor 'omics data. *PeerJ*, *2015*(10). https://doi.org/10.7717/peerj.1319
Falkowski, P. G., Greene, R. M., & Geider, R. J. (1992). Physiological Limitations on Phytoplankton Productivity in the Ocean. *Oceanography*. Oceanography Society. https://doi.org/10.2307/43924603
Flynn, K. J. (2010). Ecological modelling in a sea of variable stoichiometry: Dysfunctionality and the legacy of Redfield and Monod. *Progress in Oceanography*, *84*(1–2), 52–65. https://doi.org/10.1016/j.pocean.2009.09.006
Fraga, F. (1966). Distribution of particulate and dissolved nitrogen in the Western Indian Ocean*. *Deep-Sea Research*, *13*, 413–425. Retrieved from http://ac.els-cdn.com/0011747166910771/1-s2.0-0011747166910771-main.pdf?_tid=5da00db0-246e-11e7-b0ad-00000aab0f26&acdnat=1492544389_0b536a65ac43d3b59b1fe9080a459893
Francis, C. A., Roberts, K. J., Beman, J. M., Santoro, A. E., & Oakley, B. B. (2005). Ubiquity and diversity of ammonia-oxidizing archaea in water columns and sediments of the ocean. *Proceedings of the National Academy of Sciences of the United States of America*, *102*(41), 14683–14688. https://doi.org/10.1073/pnas.0506625102
Fu, W., Randerson, J. T., & Moore, J. K. (2016). Climate change impacts on net primary production (NPP) and export production (EP) regulated by increasing stratification and phytoplankton community structure in the CMIP5 models. *Biogeosciences*, *13*, 5151–5170. https://doi.org/10.5194/bg-13-5151-2016
Fuhrman, J., Eppley, R., Hagstrom, a, & Azam, F. (1985). Diel variations in bacterioplankton, phytoplankton, and related parameters in the Southern California Bight . *Marine Ecology Progress Series*, *27*, 9–20. https://doi.org/10.3354/meps027009
Galbraith, E. D., & Martiny, A. C. (2015). A simple nutrient-dependence mechanism for predicting the stoichiometry of marine ecosystems. *Proceedings of the National Academy of Sciences*, *112*(27), 8199–8204. https://doi.org/10.1073/pnas.1423917112
Garcia, C. A., Baer, S. E., Garcia, N. S., Rauschenberg, S., Twining, B. S., Lomas, M. W., & Martiny, A. C. (2018). Nutrient supply controls particulate elemental concentrations and ratios in the low latitude eastern Indian Ocean. *Nature Communications*, *9*(1), 4868. https://doi.org/10.1038/s41467-018-06892-w
Garcia, C.A., Hagstrom, G.I., Larken, A.A., Ustick, L.J., Levin, S.A., Lomas, M.W., & Marticy, A.C. (2020). Linking regional shifts in microbial genome adaptation with surface ocean biogeochemistry. *Phil. Trans. R. Soc. B,* 20190254. http://dx.doi.org/10.1098/rstb.2019.0254
Garcia, H. E., Locarnini, R. A., Boyer, T. P., Antonov, J. I., Baranova, O. K., Zweng, M. M., et al. (2013). *World Ocean Atlas 2013, Volume 4 : Dissolved Inorganic Nutrients (phosphate,*

nitrate, silicate). *NOAA Atlas NESDIS 76* (Vol. 4). https://doi.org/10.1182/blood-2011-06-357442
Geider, R. J., MacIntyre, H. L., & Kana, T. M. (1996). A dynamic model of photoadaptation in phytoplankton. *Limnology and Oceanography*, *41*(1), 1–15. https://doi.org/10.4319/lo.1996.41.1.0001
Giovannoni, S. J., Tripp, H. J., Givan, S., Podar, M., Vergin, K. L., Baptista, D., et al. (2005). Genetics: Genome streamlining in a cosmopolitan oceanic bacterium. *Science*, *309*(5738), 1242–1245. https://doi.org/10.1126/science.1114057
Glibert, P. M., Kana, T. M., & Brown, K. (2013). From limitation to excess: The consequences of substrate excess and stoichiometry for phytoplankton physiology, trophodynamics and biogeochemistry, and the implications for modeling. *Journal of Marine Systems*, *125*, 14–28. https://doi.org/10.1016/j.jmarsys.2012.10.004
Goldman, C. R., Elser, J. J., Richards, R. C., Reuter, J. E., Priscu, J. C., & Levin, A. L. (1996). Thermal stratification, nutrient dynamics, and phytoplankton productivity during the onset of spring phytoplankton growth in Lake Baikal, Russia. *Hydrobiologia*, *331*(1–3), 9–24. https://doi.org/10.1007/BF00025403
Gomes, H. R., Goes, J. I., & Saino, T. (2000). Influence of physical processes and freshwater discharge on the seasonality of phytoplankton regime in the Bay of Bengal. *Continental Shelf Research*, *20*(3), 313–330. https://doi.org/10.1016/S0278-4343(99)00072-2
Grand, M. M., Measures, C. I., Hatta, M., Hiscock, W. T., Landing, W. M., Morton, P. L., et al. (2015). Dissolved Fe and Al in the upper 1000 m of the eastern Indian Ocean: A high-resolution transect along 95°E from the Antarctic margin to the Bay of Bengal. *Global Biogeochemical Cycles*, *29*(3), 375–396. https://doi.org/10.1002/2014GB004920
Granum, E., Kirkvold, S., & Myklestad, S. M. (2002). Cellular and extracellular production of carbohydrates and amino acids by the marine diatom Skeletonema costatum: Diel variations and effects of N depletion. *Marine Ecology Progress Series*, *242*(Werner 1977), 83–94. https://doi.org/10.3354/meps242083
Guidot, A., Verner, M. C., Debaud, J. C., & Marmeisse, R. (2005). Intraspecific variation in use of different organic nitrogen sources by the ectomycorrhizal fungus Hebeloma cylindrosporum. *Mycorrhiza*, *15*(3), 167–177. https://doi.org/10.1007/s00572-004-0318-1
Haberer, J. L., & Brandes, J. A. (2003). A high sensitivity, low volume HPLC method to determine soluble reactive phosphate in freshwater and saltwater. *Marine Chemistry*, *82*(3–4), 185–196. https://doi.org/10.1016/S0304-4203(03)00069-0
Hall, S. R. (2009). Stoichiometrically Explicit Food Webs: Feedbacks between Resource Supply, Elemental Constraints, and Species Diversity. *Annual Review of Ecology, Evolution, and Systematics*, *40*(1), 503–528. https://doi.org/10.1146/annurev.ecolsys.39.110707.173518
Harcombe, W. R., Riehl, W. J., Dukovski, I., Granger, B. R., Betts, A., Lang, A. H., et al. (2014). Metabolic resource allocation in individual microbes determines ecosystem interactions and spatial dynamics. *Cell Reports*, *7*(4), 1104–1115. https://doi.org/10.1016/j.celrep.2014.03.070
Hennon, G. M. M., & Dyhrman, S. T. (2019). Progress and promise of omics for predicting the impacts of climate change on harmful algal blooms. *Harmful Algae*. Elsevier B.V. https://doi.org/10.1016/j.hal.2019.03.005
Herrero, A., Muro-Pastor, A. M., & Flores, E. (2001). Nitrogen control in cyanobacteria.

Journal of Bacteriology. https://doi.org/10.1128/JB.183.2.411-425.2001
Hood, R. R., Beckley, L. E., & Wiggert, J. D. (2017). Biogeochemical and ecological impacts of boundary currents in the Indian Ocean. *Progress in Oceanography*, *156*, 290–325. https://doi.org/10.1016/J.POCEAN.2017.04.011
Huang, B., & Hong, H. (1999). Alkaline phosphatase activity and utilization of dissolved organic phosphorus by algae in subtropical coastal waters. In *Marine Pollution Bulletin* (Vol. 39, pp. 205–211). Pergamon. https://doi.org/10.1016/S0025-326X(99)00006-5
Hydes, D., Aoyama, M., Aminot, A., Bakker, K., Becker, S., Coverly, S., et al. (2010). *Determination of dissolved nutrients (N, P, Si) in seawater with high precision and inter-comparability using gas-segmented continuous flow analysers*. *The GO-SHIP Repeat Hydrography Manual IOCCP Report* (Vol. 134). Retrieved from http://archimer.ifremer.fr/doc/00020/13141/
Jayapal, K. P., Philp, R. J., Kok, Y.-J., Yap, M. G. S., Sherman, D. H., Griffin, T. J., & Hu, W.-S. (2008). Uncovering genes with divergent mRNA-protein dynamics in Streptomyces coelicolor. *PloS One*, *3*(5), e2097. https://doi.org/10.1371/journal.pone.0002097
Kamykowski, D., & Zentara, S.-J. (1985). *Nitrate and silicic acid in the world ocean: patterns and processes*. *MARINE ECOLOGY-PROGRESS SERIES Mar. Ecol. Prog. Ser. I* (Vol. 26). Retrieved from https://www.int-res.com/articles/meps/26/m026p047.pdf
Kamykowski, D., Zentara, S.-J., Morrison, J. M., & Switzer, A. C. (2002). Dynamic global patterns of nitrate, phosphate, silicate, and iron availability and phytoplankton community composition from remote sensing data. *Global Biogeochemical Cycles*, *16*(4), 25-1-25–29. https://doi.org/10.1029/2001GB001640
Karl, D. M., & Tien, G. (1992). MAGIC: A sensitive and precise method for measuring dissolved phosphorus in aquatic environments. *Limnology and Oceanography*, *37*(1), 105–116. https://doi.org/10.4319/lo.1992.37.1.0105
Keith Moore, J., Fu, W., Primeau, F., Britten, G. L., Lindsay, K., Long, M., et al. (2018). Sustained climate warming drives declining marine biological productivity. *Science*. https://doi.org/10.1126/science.aao6379
Kent, A. G., Baer, S. E., Mouginot, C., Huang, J. S., Larkin, A. A., Lomas, M. W., & Martiny, A. C. (2019). Parallel phylogeography of Prochlorococcus and Synechococcus. *ISME Journal*, *13*(2), 430–441. https://doi.org/10.1038/s41396-018-0287-6
Kiørboe, T., Visser, A., & Andersen, K. H. (2018). A trait-based approach to ocean ecology. *ICES Journal of Marine Science*, *75*(6), 1849–1863. https://doi.org/10.1093/icesjms/fsy090
Klausmeier, C. A., Litchman, E., & Levin, S. A. (2004). Phytoplankton growth and stoichiometry under multiple nutrient limitation. *Limnology and Oceanography*, *49*(4_part_2), 1463–1470. https://doi.org/10.4319/lo.2004.49.4_part_2.1463
Kostadinov, T. S., Milutinović, S., Marinov, I., & Cabré, a. (2015). Carbon-based phytoplankton size classes retrieved via ocean color estimates of the particle size distribution. *Ocean Science Discussions*, *12*(3), 573–644. https://doi.org/10.5194/osd-12-573-2015
Langmead, B., & Salzberg, S. L. (2012). Fast gapped-read alignment with Bowtie 2. *Nature Methods*, *9*(4), 357–359. https://doi.org/10.1038/nmeth.1923
Larkin, A. A., & Martiny, A. C. (2017, April 1). Microdiversity shapes the traits, niche space, and biogeography of microbial taxa. *Environmental Microbiology Reports*. Wiley-Blackwell. https://doi.org/10.1111/1758-2229.12523

Larkin, A. A., Garcia, C. A., Ingoglia, K. A., Garcia, N. S., Baer, S. E., Twining, B. S., et al. (2019). Subtle biogeochemical regimes in the Indian Ocean revealed by spatial and diel frequency of Prochlorococcus haplotypes . *Limnology and Oceanography*. https://doi.org/10.1002/lno.11251

Lee, T. (2004). Decadal weakening of the shallow overturning circulation in the South Indian Ocean. *Geophysical Research Letters*, *31*(18), L18305. https://doi.org/10.1029/2004GL020884

Lee, T., Lagerloef, G., Gierach, M. M., Kao, H.-Y., Yueh, S., & Dohan, K. (2012). Aquarius reveals salinity structure of tropical instability waves. *Geophysical Research Letters*, *39*(12), n/a-n/a. https://doi.org/10.1029/2012GL052232

Li, J., & Dittrich, M. (2019). Dynamic polyphosphate metabolism in cyanobacteria responding to phosphorus availability. *Environmental Microbiology*, *21*(2), 572–583. https://doi.org/10.1111/1462-2920.14488

Li, Q. P., Hansell, D. A., & Zhang, J.-Z. (2008). Underway monitoring of nanomolar nitrate plus nitrite and phosphate in oligotrophic seawater. *Limnology and Oceanography: Methods*, *6*(7), 319–326. https://doi.org/10.4319/lom.2008.6.319

Locarnini, R. A., Mishonov, A. V., Antonov, J. I., Boyer, T. P., Garcia, H. E., Baranova, O. K., et al. (2013). World Ocean Atlas 2013. Vol. 1: Temperature. *S. Levitus, Ed.; A. Mishonov, Technical Ed.; NOAA Atlas NESDIS*, *73*(September), 40. https://doi.org/10.1182/blood-2011-06-357442

Lomas, M. W., Burke, A. L., Lomas, D. A., Bell, D. W., Shen, C., Dyhrman, S. T., & Ammerman, J. W. (2010). Sargasso Sea phosphorus biogeochemistry: an important role for dissolved organic phosphorus (DOP). *Biogeosciences*, *7*(2), 695–710. https://doi.org/10.5194/bg-7-695-2010

Lomas, Michael W., Baer, S. E., Acton, S., & Krause, J. W. (2019). Pumped Up by the Cold: Elemental Quotas and Stoichiometry of Cold-Water Diatoms. *Frontiers in Marine Science*. https://doi.org/10.3389/fmars.2019.00286

Lomas, Michael W, Bonachela, J. A., Levin, S. A., & Martiny, A. C. (2014). Impact of ocean phytoplankton diversity on phosphate uptake. *Proceedings of the National Academy of Sciences*, *111*(49), 17540–17545. https://doi.org/10.1073/pnas.1420760111

Lopez, J. S., Garcia, N. S., Talmy, D., & Martiny, A. C. (2016). Diel variability in the elemental composition of the marine cyanobacterium *Synechococcus*. *Journal of Plankton Research*, *38*(4), 1052–1061. https://doi.org/10.1093/plankt/fbv120

Maier, T., Schmidt, A., Güell, M., Kühner, S., Gavin, A. C., Aebersold, R., & Serrano, L. (2011). Quantification of mRNA and protein and integration with protein turnover in a bacterium. *Molecular Systems Biology*, *7*. https://doi.org/10.1038/msb.2011.38

Makino, W., Cotner, J. B., Sterner, R. W., & Elser, J. J. (2003). Are bacteria more like plants or animals? Growth rate and resource dependence of bacterial C : N : P stoichiometry. *Functional Ecology*, *17*(1), 121–130. https://doi.org/10.1046/j.1365-2435.2003.00712.x

Malmstrom, R. R., Rodrigue, S., Huang, K. H., Kelly, L., Kern, S. E., Thompson, A., et al. (2013). Ecology of uncultured Prochlorococcus clades revealed through single-cell genomics and biogeographic analysis. *ISME Journal*, *7*(1), 184–198. https://doi.org/10.1038/ismej.2012.89

Marañón, E., Lorenzo, M. P., Cermeño, P., & Mouriño-Carballido, B. (2018). Nutrient limitation suppresses the temperature dependence of phytoplankton metabolic rates.

ISME Journal, *12*(7), 1836–1845. https://doi.org/10.1038/s41396-018-0105-1
Mark Moore, C., Mills, M. M., Achterberg, E. P., Geider, R. J., Laroche, J., Lucas, M. I., et al. (2009). Large-scale distribution of Atlantic nitrogen fixation controlled by iron availability. *Nature Geoscience*, *2*(12), 867–871. https://doi.org/10.1038/ngeo667
Martin, J. H., Coale, K. H., Johnson, K. S., Fitzwater, S. E., Gordon, R. M., Tanner, S. J., et al. (1994). Testing the iron hypothesis in ecosystems of the equatorial Pacific Ocean. *Nature*, *371*(6493), 123–129. https://doi.org/10.1038/371123a0
Martin, P., Dyhrman, S. T., Lomas, M. W., Poulton, N. J., & Van Mooy, B. A. S. (2014). Accumulation and enhanced cycling of polyphosphate by Sargasso Sea plankton in response to low phosphorus. *Proceedings of the National Academy of Sciences of the United States of America*, *111*(22), 8089–8094. https://doi.org/10.1073/pnas.1321719111
Martiny, A. C., Coleman, M. L., & Chisholm, S. W. (2006). Phosphate acquisition genes in Prochlorococcus ecotypes: Evidence for genome-wide adaptation. *Proceedings of the National Academy of Sciences*, *103*(33), 12552–12557. https://doi.org/10.1073/pnas.0601301103
Martiny, A. C., Vrugt, J. A., Primeau, F. W., & Lomas, M. W. (2013). Regional variation in the particulate organic carbon to nitrogen ratio in the surface ocean. *Global Biogeochemical Cycles*, *27*(3), 723–731. https://doi.org/10.1002/gbc.20061
Martiny, Adam C., Huang, Y., & Li, W. (2009). Occurrence of phosphate acquisition genes in Prochlorococcus cells from different ocean regions. *Environmental Microbiology*, *11*(6), 1340–1347. https://doi.org/10.1111/j.1462-2920.2009.01860.x
Martiny, Adam C., Kathuria, S., & Berube, P. M. (2009). Widespread metabolic potential for nitrite and nitrate assimilation among Prochlorococcus ecotypes. *Proceedings of the National Academy of Sciences of the United States of America*, *106*(26), 10787–10792. https://doi.org/10.1073/pnas.0902532106
Martiny, Adam C., Pham, C. T. A., Primeau, F. W., Vrugt, J. A., Moore, J. K., Levin, S. A., & Lomas, M. W. (2013). Strong latitudinal patterns in the elemental ratios of marine plankton and organic matter. *Nature Geoscience*, *6*(4), 279–283. https://doi.org/10.1038/ngeo1757
Martiny, Adam C., Ma, L., Mouginot, C., Chandler, J. W., & Zinser, E. R. (2016). Interactions between thermal acclimation, growth rate, and phylogeny influence prochlorococcus elemental stoichiometry. *PLoS ONE*, *11*(12), e0168291. https://doi.org/10.1371/journal.pone.0168291
Martiny, Adam C., Lomas, M. W., Fu, W., Boyd, P. W., Chen, Y. L., Cutter, G. A., et al. (2019). Biogeochemical controls of surface ocean phosphate. *Science Advances*, *5*(8), eaax0341. https://doi.org/10.1126/sciadv.aax0341
Martiny, Adam C., Ustick, L., A. Garcia, C., & Lomas, M. W. (2019). Genomic adaptation of marine phytoplankton populations regulates phosphate uptake. *Limnology and Oceanography*. https://doi.org/10.1002/lno.11252
Martiny, Adam C, Vrugt, J. A., & Lomas, M. W. (2014). Concentrations and ratios of particulate organic carbon, nitrogen, and phosphorus in the global ocean. *Scientific Data*, *1*, 140048. https://doi.org/10.1038/sdata.2014.48
Martiny, J. B. H., Jones, S. E., Lennon, J. T., & Martiny, A. C. (2015, November 6). Microbiomes in light of traits: A phylogenetic perspective. *Science*. American Association for the Advancement of Science. https://doi.org/10.1126/science.aac9323

Mason, O. U., Hazen, T. C., Borglin, S., Chain, P. S. G., Dubinsky, E. A., Fortney, J. L., et al. (2012). Metagenome, metatranscriptome and single-cell sequencing reveal microbial response to Deepwater Horizon oil spill. *ISME Journal*, *6*(9), 1715–1727. https://doi.org/10.1038/ismej.2012.59

Mather, R. L., Reynolds, S. E., Wolff, G. A., Williams, R. G., Torres-Valdes, S., Woodward, E. M. S., et al. (2008). Phosphorus cycling in the North and South Atlantic Ocean subtropical gyres. *Nature Geoscience*, *1*(7), 439–443. https://doi.org/10.1038/ngeo232

Meissner, T., Wentz, F. J., & Vine, D. M. Le. (2018). The Salinity Retrieval Algorithms for the NASA Aquarius Version 5 and SMAP Version 3 Releases. *Remote Sensing*, *10*(7), 1121. https://doi.org/10.3390/rs10071121

Mills, M. M., Moore, C. M., Langlois, R., Milne, A., Achterberg, E., Nachtigall, K., et al. (2008). Nitrogen and phosphorus co-limitation of bacterial productivity and growth in the oligotrophic subtropical North Atlantic. *Limnology and Oceanography*, *53*(2), 824–834. https://doi.org/10.4319/lo.2008.53.2.0824

Mills, Matthew M., Ridame, C., Davey, M., La Roche, J., & Geider, R. J. (2004). Iron and phosphorus co-limit nitrogen fixation in the eastern tropical North Atlantic. *Nature*, *429*(6989), 292–294. https://doi.org/10.1038/nature02550

Mock, T., Daines, S. J., Geider, R., Collins, S., Metodiev, M., Millar, A. J., et al. (2016, January 1). Bridging the gap between omics and earth system science to better understand how environmental change impacts marine microbes. *Global Change Biology*. Blackwell Publishing Ltd. https://doi.org/10.1111/gcb.12983

MONOD, J. (1950). Technique, Theory and Applications of Continuous Culture. *Ann. Inst. Pasteur*, *79*(4), 390–410.

Moore, C. M., Mills, M. M., Arrigo, K. R., Berman-Frank, I., Bopp, L., Boyd, P. W., et al. (2013). Processes and patterns of oceanic nutrient limitation. *Nature Geoscience*, *6*(9), 701–710. https://doi.org/10.1038/ngeo1765

Moore, J. K., & Doney, S. C. (2007). Iron availability limits the ocean nitrogen inventory stabilizing feedbacks between marine denitrification and nitrogen fixation. *Global Biogeochemical Cycles*, *21*(2), n/a-n/a. https://doi.org/10.1029/2006GB002762

Moore, L. R., Post, A. F., Rocap, G., & Chisholm, S. W. (2002). Utilization of different nitrogen sources by the marine cyanobacteria Prochlorococcus and Synechococcus. *Limnology and Oceanography*, *47*(4), 989–996. https://doi.org/10.4319/lo.2002.47.4.0989

Moran, M. A. (2015, December 11). The global ocean microbiome. *Science*. American Association for the Advancement of Science. https://doi.org/10.1126/science.aac8455

Moreno, A. R., & Martiny, A. C. (2018). Ecological Stoichiometry of Ocean Plankton. *Annual Review of Marine Science*, *10*(August 2017), 1–27. https://doi.org/10.1146/annurev-marine-121916-063126

Moreno, A. R., Hagstrom, G. I., Primeau, F. W., Levin, S. A., & Martiny, A. C. (2018). Marine phytoplankton stoichiometry mediates nonlinear interactions between nutrient supply, temperature, and atmospheric CO2. *Biogeosciences*. https://doi.org/10.5194/bg-15-2761-2018

Morris, J. J., Lenski, R. E., & Zinser, E. R. (2012). The Black Queen Hypothesis: evolution of dependencies through adaptive gene loss. *MBio*, *3*(2), e00036-12-. https://doi.org/10.1128/mBio.00036-12

Moutin, T., Van Den B, B., Beker, B., Dupouy, C., Rimmelin, P., & Le Bouteiller, A. (2005). Phosphate availability controls Trichodesmium spp. biomass in the SW Pacific Ocean.

Marine Ecology Progress Series, *297*, 15–21. https://doi.org/10.3354/meps297015
Moutin, T., Karl, D. M., Duhamel, S., Rimmelin, P., Raimbault, P., Van Mooy, B. A. S. S., & Claustre, H. (2008). Phosphate availability and the ultimate control of new nitrogen input by nitrogen fixation in the tropical Pacific Ocean. *Biogeosciences*, *5*(1), 95–109. https://doi.org/10.5194/bg-5-95-2008
Mouw, C. B., Ciochetto, A. B., & Yoder, J. A. (2019). A Satellite Assessment of Environmental Controls of Phytoplankton Community Size Structure. *Global Biogeochemical Cycles*, 2018GB006118. https://doi.org/10.1029/2018GB006118
NASA Goddard Space Flight Center, Ocean Ecology Laboratory, Ocean Biology Processing Group. Moderate-resolution Imaging Spectroradiometer (MODIS) Aqua Chlorophyll a 4km Data; NASA OB.DAAC, Greenbelt, MD, USA. (n.d.). https://doi.org/10.5067/AQUA/MODIS/L3M/CHL/2016
Ng, W. H. A., & Liu, H. (2016). Diel periodicity of grazing by heterotrophic nanoflagellates influenced by prey cell properties and intrinsic grazing rhythm. *Journal of Plankton Research*, *38*, fbw014. https://doi.org/10.1093/plankt/fbw014
Olsen, A., Key, R. M., van Heuven, S., Lauvset, S. K., Velo, A., Lin, X., et al. (2016). The Global Ocean Data Analysis Project version 2 (GLODAPv2) – an internally consistent data product for the world ocean. *Earth System Science Data*, *8*(2), 297–323. https://doi.org/10.5194/essd-8-297-2016
Olsen, A., Lange, N., Key, R. M., Tanhua, T., Álvarez, M., Becker, S., et al. (2019). GLODAPv2.2019 - an update of GLODAPv2. *Earth System Science Data*.
Oschlies, A., & Garçon, V. (1998). Eddy-induced enhancement of primary production in a model of the North Atlantic Ocean. *Nature*, *394*(6690), 266–269. https://doi.org/10.1038/28373
Ottesen, E. A., Young, C. R., Gifford, S. M., Eppley, J. M., Marin, R., Schuster, S. C., et al. (2014). Multispecies diel transcriptional oscillations in open ocean heterotrophic bacterial assemblages. *Science*, *345*(6193), 207–212. https://doi.org/10.1126/science.1252476
Pabi, S., van Dijken, G. L., & Arrigo, K. R. (2008). Primary production in the Arctic Ocean, 1998–2006. *Journal of Geophysical Research*, *113*(C8), C08005. https://doi.org/10.1029/2007JC004578
Palacios, D. M., Hazen, E. L., Schroeder, I. D., & Bograd, S. J. (2013). Modeling the temperature-nitrate relationship in the coastal upwelling domain of the California Current. *Journal of Geophysical Research: Oceans*, *118*(7), 3223–3239. https://doi.org/10.1002/jgrc.20216
Partensky, F., & Garczarek, L. (2010). Prochlorococcus : Advantages and Limits of Minimalism . *Annual Review of Marine Science*, *2*(1), 305–331. https://doi.org/10.1146/annurev-marine-120308-081034
Passow, U., & Peinert, R. (1993). The role of plankton in particle flux: two case studies from the northeast Atlantic. *Deep Sea Research Part II: Topical Studies in Oceanography*, *40*(1–2), 573–585. https://doi.org/10.1016/0967-0645(93)90033-J
Polovina, J. J., Howell, E. A., & Abecassis, M. (2008). Ocean's least productive waters are expanding. *Geophysical Research Letters*, *35*(December 2007), 2–6. https://doi.org/10.1029/2007GL031745
Poretsky, R. S., Hewson, I., Sun, S., Allen, A. E., Zehr, J. P., & Moran, M. A. (2009). Comparative day/night metatranscriptomic analysis of microbial communities in the North Pacific subtropical gyre. *Environmental Microbiology*, *11*(6), 1358–1375.

https://doi.org/10.1111/j.1462-2920.2008.01863.x
Prasanna Kumar, S., Muraleedharan, P. M., Prasad, T. G., Gauns, M., Ramaiah, N., de Souza, S. N., et al. (2002). Why is the Bay of Bengal less productive during summer monsoon compared to the Arabian Sea? *Geophysical Research Letters*, *29*(24), 88-1-88–4. https://doi.org/10.1029/2002GL016013
Punyu, V. R., Banakar, V. K., & Garg, A. (2014). Equatorial Indian Ocean productivity during the last 33 kyr and possible linkage to Westerly Jet variability. *Marine Geology*, *348*, 44–51. https://doi.org/10.1016/J.MARGEO.2013.11.010
Randles, C. A., da Silva, A. M., Buchard, V., Colarco, P. R., Darmenov, A., Govindaraju, R., et al. (2017). The MERRA-2 Aerosol Reanalysis, 1980 Onward. Part I: System Description and Data Assimilation Evaluation. *Journal of Climate*, *30*(17), 6823–6850. https://doi.org/10.1175/JCLI-D-16-0609.1
Rao, R. R., & Sivakumar, R. (2003). Seasonal variability of sea surface salinity and salt budget of the mixed layer of the north Indian Ocean. *Journal of Geophysical Research*, *108*(C1), 3009. https://doi.org/10.1029/2001JC000907
Redfield, A. C. (1934). *On the proportions of organic derivatives in sea water and their relation to the composition of plankton*. *James Johnstone Memorial* (Vol. 176–192). University Press of Liverpool.
Rembauville, M., Blain, S., Caparros, J., & Salter, I. (2016). Particulate matter stoichiometry driven by microplankton community structure in summer in the Indian sector of the Southern Ocean. *Limnology and Oceanography*, *61*(4), 1301–1321. https://doi.org/10.1002/lno.10291
Rijkenberg, M. J. A., Middag, R., Laan, P., Gerringa, L. J. A., Van Aken, H. M., Schoemann, V., et al. (2014). The distribution of dissolved iron in the West Atlantic Ocean. *PLoS ONE*, *9*(6). https://doi.org/10.1371/journal.pone.0101323
Robidart, J. C., Magasin, J. D., Shilova, I. N., Turk-Kubo, K. A., Wilson, S. T., Karl, D. M., et al. (2019). Effects of nutrient enrichment on surface microbial community gene expression in the oligotrophic North Pacific Subtropical Gyre. *ISME Journal*, *13*(2), 374–387. https://doi.org/10.1038/s41396-018-0280-0
Rusch, D. B., Martiny, A. C., Dupont, C. L., Halpern, A. L., & Venter, J. C. (2010). Characterization of Prochlorococcus clades from iron-depleted oceanic regions. *Proceedings of the National Academy of Sciences of the United States of America*, *107*(37), 16184–9. https://doi.org/10.1073/pnas.1009513107
Scanlan, D. J., Ostrowski, M., Mazard, S., Dufresne, A., Garczarek, L., Hess, W. R., et al. (2009). Ecological Genomics of Marine Picocyanobacteria. *Microbiology and Molecular Biology Reviews*, *73*(2), 249–299. https://doi.org/10.1128/mmbr.00035-08
Schlüter, L., Henriksen, P., Nielsen, T. G., & Jakobsen, H. H. (2011). Phytoplankton composition and biomass across the southern Indian Ocean. *Deep Sea Research Part I: Oceanographic Research Papers*, *58*(5), 546–556. https://doi.org/10.1016/j.dsr.2011.02.007
Schneider, B., Engel, A., & Schlitzer, R. (2004). Effects of depth- and CO2-dependent C:N ratios of particulate organic matter (POM) on the marine carbon cycle. *Global Biogeochemical Cycles*, *18*(2), n/a-n/a. https://doi.org/10.1029/2003GB002184
Schott, F. A., Dengler, M., & Schoenefeldt, R. (2002). The shallow overturning circulation of the Indian Ocean. *Progress in Oceanography*, *53*(1), 57–103. https://doi.org/10.1016/S0079-6611(02)00039-3

Shilova, I. N., Mills, M. M., Robidart, J. C., Turk-Kubo, K. A., Björkman, K. M., Kolber, Z., et al. (2017). Differential effects of nitrate, ammonium, and urea as N sources for microbial communities in the North Pacific Ocean. *Limnology and Oceanography*, *62*(6), 2550–2574. https://doi.org/10.1002/LNO.10590@10.1002/(ISSN)1939-5590.ALOHA30

Shin, N. R., Whon, T. W., & Bae, J. W. (2015, September 1). Proteobacteria: Microbial signature of dysbiosis in gut microbiota. *Trends in Biotechnology*. Elsevier Ltd. https://doi.org/10.1016/j.tibtech.2015.06.011

Shiozaki, T., Ijichi, M., Kodama, T., Takeda, S., & Furuya, K. (2014). Heterotrophic bacteria as major nitrogen fixers in the euphotic zone of the Indian Ocean. *Global Biogeochemical Cycles*, *28*(10), 1096–1110. https://doi.org/10.1002/2014GB004886

Siegel, D. A., McGillicuddy, D. J., & Fields, E. A. (1999). Mesoscale eddies, satellite altimetry, and new production in the Sargasso Sea. *Journal of Geophysical Research: Oceans*, *104*(C6), 13359–13379. https://doi.org/10.1029/1999JC900051

Smith, S. L., Pahlow, M., Merico, A., Acevedo-Trejos, E., Sasai, Y., Yoshikawa, C., et al. (2016). Flexible phytoplankton functional type (FlexPFT) model: Size-scaling of traits and optimal growth. *Journal of Plankton Research*, *38*(4), 977–992. https://doi.org/10.1093/plankt/fbv038

Sosa, O. A., Casey, J. R., & Karl, D. M. (2019). Methylphosphonate Oxidation in *Prochlorococcus* Strain MIT9301 Supports Phosphate Acquisition, Formate Excretion, and Carbon Assimilation into Purines. *Applied and Environmental Microbiology*, *85*(13). https://doi.org/10.1128/AEM.00289-19

Stan Development Team. (2017). MatlabStan: The MATLAB interface to Stan. https://doi.org/asd

Steinberg, D. K., Carlson, C. A., Bates, N. R., Johnson, R. J., Michaels, A. F., & Knap, A. H. (2001). Overview of the US JGOFS Bermuda Atlantic Time-series Study (BATS): A decade-scale look at ocean biology and biogeochemistry. *Deep-Sea Research Part II: Topical Studies in Oceanography*, *48*(8–9), 1405–1447. https://doi.org/10.1016/S0967-0645(00)00148-X

Steinhoff, T., Friedrich, T., Hartman, S. E., Oschlies, A., Wallace, D. W. R., & Körtzinger, A. (2010). *Estimating mixed layer nitrate in the North Atlantic Ocean*. *Biogeosciences* (Vol. 7). Retrieved from www.biogeosciences.net/7/795/2010/

Sterner, R. W., & Elser, J. J. (2002). *Ecological Stoichiometry: The Biology of Elements from Molecules to the Biosphere*. Princeton University Press. Retrieved from http://books.google.com/books?hl=en&lr=&id=53NTDvppdYUC&pgis=1

Strutton, P. G., Coles, V. J., Hood, R. R., Matear, R. J., Mcphaden, M. J., & Phillips, H. E. (2015). Biogeochemical variability in the central equatorial Indian Ocean during the monsoon transition. *Biogeosciences*, *12*, 2367–2382. https://doi.org/10.5194/bg-12-2367-2015

Sunagawa, S., Coelho, L. P., Chaffron, S., Kultima, J. R., Labadie, K., Salazar, G., et al. (2015). Structure and function of the global ocean microbiome. *Science*, *348*(6237). https://doi.org/10.1126/science.1261359

Swan, B. K., Tupper, B., Sczyrba, A., Lauro, F. M., Martinez-Garcia, M., Gonźalez, J. M., et al. (2013). Prevalent genome streamlining and latitudinal divergence of planktonic bacteria in the surface ocean. *Proceedings of the National Academy of Sciences of the United States of America*, *110*(28), 11463–11468. https://doi.org/10.1073/pnas.1304246110

Swift, J. (SIO), & Becker, S. (SIO). (n.d.). I09N, 33RR20160321_hy1.csv, CLIVAR and Carbon

Hydrographic Data Office, La Jolla, CA, USA. Retrieved August 6, 2017, from https://cchdo.ucsd.edu/cruise/33RR20160321
Switzer, A. C., Kamykowski, D., & Zentara, S. (2003). Mapping nitrate in the global ocean using remotely sensed sea surface temperature. *Journal of Geophysical Research*, *108*(C8), 3280. https://doi.org/10.1029/2000JC000444
Tagliabue, A., Mtshali, T., Aumont, O., Bowie, A. R., Klunder, M. B., Roychoudhury, A. N., & Swart, S. (2012). A global compilation of dissolved iron measurements: focus on distributions and processes in the Southern Ocean. *Biogeosciences*, *95194*, 2333–2349. https://doi.org/10.5194/bg-9-2333-2012
Takahashi, T., Sutherland, S. C., Wanninkhof, R., Sweeney, C., Feely, R. A., Chipman, D. W., et al. (2009). Climatological mean and decadal change in surface ocean pCO2, and net sea–air CO2 flux over the global oceans. *Deep Sea Research Part II: Topical Studies in Oceanography*, *56*(8–10), 554–577. https://doi.org/10.1016/j.dsr2.2008.12.009
Talmy, D., Blackford, J., Hardman-Mountford, N. J., Dumbrell, A. J., & Geider, R. J. (2013). An optimality model of photoadaptation in contrasting aquatic light regimes. *Limnology and Oceanography*, *58*(5), 1802–1818. https://doi.org/10.4319/lo.2013.58.5.1802
Tanioka, T., & Matsumoto, K. (2017). Buffering of Ocean Export Production by Flexible Elemental Stoichiometry of Particulate Organic Matter. *Global Biogeochemical Cycles*, *31*(10), 1528–1542. https://doi.org/10.1002/2017GB005670
Tapia-Torres, Y., Rodríguez-Torres, M. D., Elser, J. J., Islas, A., Souza, V., García-Oliva, F., & Olmedo-Álvarez, G. (2016). How to live with phosphorus scarcity in soil and sediment: Lessons from bacteria. *Applied and Environmental Microbiology*, *82*(15), 4652–4662. https://doi.org/10.1128/AEM.00160-16
Teng, Y.-C. C., Primeau, F. W., Moore, J. K., Lomas, M. W., & Martiny, A. C. (2014). Global-scale variations of the ratios of carbon to phosphorus in exported marine organic matter. *Nature Geoscience*, *7*(12), 895–898. https://doi.org/10.1038/NGEO2303
Thomas, M. K., Kremer, C. T., & Litchman, E. (2016). Environment and evolutionary history determine the global biogeography of phytoplankton temperature traits. *Global Ecology and Biogeography*, *25*(1), 75–86. https://doi.org/10.1111/geb.12387
Thrane, J.-E., Hessen, D. O., & Andersen, T. (2017). Plasticity in algal stoichiometry: Experimental evidence of a temperature-induced shift in optimal supply N:P ratio. *Limnology and Oceanography*, *62*(4), 1346–1354. https://doi.org/10.1002/lno.10500
Tilman, D., Kilham, S. S., & Kilham, P. (1982). Phytoplankton Community Ecology: The Role of Limiting Nutrients. *Annual Review of Ecology and Systematics*, *13*(1), 349–372. https://doi.org/10.1146/annurev.es.13.110182.002025
Toseland, A., Uhlig, C., Valentin, K., Daines, S. J., Mock, T., Kirkham, A., et al. (2013). The impact of temperature on marine phytoplankton resource allocation and metabolism. *Nature Climate Change*, *3*(11), 979–984. https://doi.org/10.1038/nclimate1989
Tréguer, P., Bowler, C., Moriceau, B., Dutkiewicz, S., Gehlen, M., Aumont, O., et al. (2018, January 1). Influence of diatom diversity on the ocean biological carbon pump. *Nature Geoscience*. Nature Publishing Group. https://doi.org/10.1038/s41561-017-0028-x
Tripp, H. J., Bench, S. R., Turk, K. A., Foster, R. A., Desany, B. A., Niazi, F., et al. (2010). Metabolic streamlining in an open-ocean nitrogen-fixing cyanobacterium. *Nature*, *464*(7285), 90–94. https://doi.org/10.1038/nature08786
Twining, B. S., Baines, S. B., Bozard, J. B., Vogt, S., Walker, E. A., & Nelson, D. M. (2011). Metal quotas of plankton in the equatorial Pacific Ocean. *Deep-Sea Research Part II: Topical*

Studies in Oceanography, *58*(3–4), 325–341. https://doi.org/10.1016/j.dsr2.2010.08.018
Twining, B. S., Rauschenberg, S., Baer, S. E., Lomas, M. W., Martiny, A. C., & Antipova, O. (2019). A nutrient limitation mosaic in the eastern tropical Indian Ocean. *Deep-Sea Research Part II: Topical Studies in Oceanography*. https://doi.org/10.1016/j.dsr2.2019.05.001
Tyrrell, T. (1999). The relative influences of nitrogen and phosphorus on oceanic primary production. *Nature*, *400*(6744), 525–531. https://doi.org/10.1038/22941
Veldhuis, M. J. W., Kraay, G. W., Van Bleijswijk, J. D. L., & Baars, M. A. (1997). Seasonal and spatial variability in phytoplankton biomass, productivity and growth in the northwestern Indian ocean: The southwest and northeast monsoon, 1992-1993. *Deep-Sea Research Part I: Oceanographic Research Papers*, *44*(3), 425–449. https://doi.org/10.1016/S0967-0637(96)00116-1
Venter, J. C., Remington, K., Heidelberg, J. F., Halpern, A. L., Rusch, D., Eisen, J. A., et al. (2004). Environmental Genome Shotgun Sequencing of the Sargasso Sea. *Science*, *304*(5667), 66–74. https://doi.org/10.1126/science.1093857
Waldron, H. N., & Probyn, T. A. (2010). Benguela upwelling system. *South African Journal of Marine Science*, *12*(1), 29–39. https://doi.org/10.2989/02577619209504688
Wang, D., Cui, Q., Gong, F., Wang, L., He, X., Bai, Y., et al. (2018). Satellite Retrieval of Surface Water Nutrients in the Coastal Regions of the East China Sea. *Remote Sensing*, *10*(12), 1896. https://doi.org/10.3390/rs10121896
Wang, W. L., Moore, J. K., Martiny, A. C., & Primeau, F. W. (2019). Convergent estimates of marine nitrogen fixation. *Nature*, *566*(7743), 205–211. https://doi.org/10.1038/s41586-019-0911-2
Wanninkhof, R., Sullivan, K., & Pierrot, D. (2016). Underway pCO2 Measurements in Surface Waters and the Atmosphere During the R/V Roger Revelle GO-SHIP cruise along the section I09N_2016 (March 21 - April 27, 2016). http://cdiac.ornl.gov/ftp/oceans/CLIVAR/I09N_33RR20160321/Underway/. Carbon Dioxide Inform. https://doi.org/10.3334/CDIAC/OTG.GO_SHIP_I09N_33RR20160321_UW
Ward, B. A. (2017). Assessing an efficient “instant Acclimation” approximation of dynamic phytoplankton stoichiometry. *Journal of Plankton Research*, *39*(5), 803–814. https://doi.org/10.1093/plankt/fbx040
Weber, T. S., & Deutsch, C. (2010a). Ocean nutrient ratios governed by plankton biogeography. *Nature*, *467*. https://doi.org/10.1038/nature09403
Weber, T. S., & Deutsch, C. (2010b). Ocean nutrient ratios governed by plankton biogeography. *Nature*, *467*. https://doi.org/10.1038/nature09403
Wentz, F., Yueh, S., & Lagerloef, G. (2014). Aquarius Level 3 Sea Surface Salinity Standard Mapped Image Annual Data V3.0 | PO.DAAC. https://doi.org/http://dx.doi.org/10.5067/AQUAR-3SAPS
Westberry, T., Behrenfeld, M. J., Siegel, D. a., & Boss, E. (2008). Carbon-based primary productivity modeling with vertically resolved photoacclimation. *Global Biogeochemical Cycles*, *22*(August 2007), 1–18. https://doi.org/10.1029/2007GB003078
Wiggert, J. D., Vialard, J., & Behrenfeld, M. J. (2009). Basin-wide modification of dynamical and biogeochemical processes by the positive phase of the Indian Ocean dipole during

the SeaWiFS era (pp. 385–407). American Geophysical Union (AGU). https://doi.org/10.1029/2008GM000776

Williams, R. G., McLaren, A. J., & Follows, M. J. (2000). Estimating the convective supply of nitrate and implied variability in export production over the North Atlantic. *Global Biogeochemical Cycles*, *14*(4), 1299–1313. https://doi.org/10.1029/2000GB001260

Wilson, C., & Coles, V. J. (2005). Global climatological relationships between satellite biological and physical observations and upper ocean properties. *J. Geophys. Res*, *110*, 10001. https://doi.org/10.1029/2004JC002724

Wu, J., Sunda, W., Boyle, E. A., & Karl, D. M. (2000). Phosphate Depletion in the Western North Atlantic Ocean. *Science*, *289*(5480). Retrieved from http://science.sciencemag.org/content/289/5480/759

Wyrtki, K. (1973). An Equatorial Jet in the Indian Ocean. *Science*, *181*(4096), 262–264. https://doi.org/10.1126/science.181.4096.262

Yvon-Durocher, G., Dossena, M., Trimmer, M., Woodward, G., & Allen, A. P. (2015). Temperature and the biogeography of algal stoichiometry. *Global Ecology and Biogeography*, *24*(5), 562–570. https://doi.org/10.1111/geb.12280

Zimmerman, A. E., Allison, S. D., & Martiny, A. C. (2014). Phylogenetic constraints on elemental stoichiometry and resource allocation in heterotrophic marine bacteria. *Environmental Microbiology*, *16*(5), 1398–1410. https://doi.org/10.1111/1462-2920.12329

Zwirglmaier, K., Jardillier, L., Ostrowski, M., Mazard, S., Garczarek, L., Vaulot, D., et al. (2008). Global phylogeography of marine Synechococcus and Prochlorococcus reveals a distinct partitioning of lineages among oceanic biomes. *Environmental Microbiology*, *10*(1), 147–161. https://doi.org/10.1111/j.1462-2920.2007.01440.x